PIEZOELECTRIC MEMS: MICROSYSTEMS BASED ON BULK PZT LATERAL BIMORPHS FOR LOW-POWER APPLICATIONS AND TOWARD BULK DIFFRACTION WAVE GYROSCOPES

A Dissertation

Presented to the Faculty of the Graduate School

of Cornell University

In Partial Fulfillment of the Requirements for the Degree of

Doctor of Philosophy

by

Visarute Pinrod

May 2020

PIEZOELECTRIC MEMS: MICROSYSTEMS BASED ON BULK PZT LATERAL BIMORPHS FOR LOW-POWER APPLICATIONS AND TOWARD BULK DIFFRACTION WAVE GYROSCOPES

Visarute Pinrod, Ph.D.

Cornell University 2020

Piezoelectric microelectromechanical systems (MEMS) technology, compared to conventional discrete manufacturing techniques, allows the development of sensors and wireless transmitters in smaller sizes, lowered cost, and lower power consumption. This dissertation presents two research areas of piezoelectric MEMS: microsystems based on bulk lead zirconate titanate (PZT) lateral bimorphs, and high-overtone bulk diffraction wave gyroscopes.

First, the microsystems for low power applications are developed based on piezoelectric lateral bimorphs fabricated by a 150-µm-resolution laser-micromachining process on 500-µm-thick bulk PZT. Compared to piezoelectric thin-film bimorphs, bulk PZT provides higher electromechanical coupling (k_{33} = 0.72) and high dielectric coefficient (ε_r = 1275). The high k_{33} enables efficient transduction from electrical to mechanical domain for actuators, and high mechanical to electrical signal for sensors. The high ε_r enables greater charge to be generated for energy harvesters. This dissertation presents PZT-bimorph-based microsystems designed for the following applications: 1) near-zero power consumption event detection devices, 2) in-*situ* MEMS gyroscope calibration, and 3) ultralow frequency (ULF) communication by mechanical motion of magnets. The first application is the near-zero power event detection, where zero-power PZT-bimorph-based sensors are used to measure acceleration, rotation, magnetic field, and sound. NEMS switches or CMOS comparators detect desired signal

patterns and generate wakeup triggers. Prototypes are evaluated in the laboratory and field tests consisting of detections of electrical generators, cars, and trucks. The power consumption of the system with a low-power CMOS comparator is 2-6 nW, which potentially enables the development of long-lifetime battery-powered IoT devices. The second application is the calibration of MEMS gyroscopes, where PZT-bimorph-based dither stages are used to calibrate and reduce gyroscope scale factor errors down to 50 ppm from 5.5%. Gyroscopes integrated with the calibration dither stages potentially allows for low-cost gyroscopes to be used for navigation, significantly reducing the cost, weight, and size of navigation grade gyroscopes. The third application is the ULF communication, which permanent magnets are actuated by the PZT-bimorph-based dither stages to generate a time-varying magnetic field in the ULF range (300 Hz - 3 kHz). A transmitter prototype consumes lower power (1.8 μW) and is capable of wirelessly communicating up to 20 m at a frequency of 893 Hz and modulation bandwidth of 2.4 Hz. The transmitter can potentially communicate underwater, underground, and in the air due to low attenuation, reflection, and refraction of the ULF magnetic induction.

High-overtone bulk diffraction wave gyroscopes are developed to operate in high-shock environments such as autonomous vehicles during accidents. Unlike most commercial MEMS gyroscopes, this gyroscope eliminates the need for proof masses, which can impact parts of the package when exposed to high shocks. The gyroscope uses interdigitated electrodes that excite thickness mode resonances of the longitudinal waves in a lithium niobate substrate. The gyroscope measures rotation from the effects of the Coriolis force on bulk acoustic shear waves generated by the diffraction and reflection of the longitudinal wave.

BIOGRAPHICAL SKETCH

Visarute Pinrod (Earth) was born in 1990 in Bangkok, Thailand. He attended primary school at Assumption College Thonburi in Bangkok, Thailand, and high school at Mahidol Wittayanusorn School in Nakhon Pathom, Thailand. In 2013, Visarute completed his undergraduate degree at Brown University in Providence, RI, earning a Bachelor of Science in engineering and Physics. At Brown, he was part of the Zia Lab under the guidance of Prof. Rashid Zia and worked on investigating the emission of magnetic and electric dipoles near Bragg mirrors. Later in 2013, he began his doctoral education at Cornell University in the SonicMEMS Laboratory under the guidance of Prof. Amit Lal. His research focuses on piezoelectric microelectromechanical systems (MEMS), inertial sensors, and low power sensors.

To my mother, father, and Nahong Kim

For their love, encouragement, and support

ACKNOWLEDGMENTS

This dissertation cannot be complete without help from numerous people. I would like to express my deepest gratitude to my advisor, Prof. Amit Lal, for his hard work, creative ideas, and insightful navigation. Experience from working under his guidance has transformed me into not only a better scientist but also a better person. Next, I would like to acknowledge my committee member: Prof. Clifford Pollock, and Prof. Alyosha Molnar, for their guidance. I am thankful to Prof. Edwin Chihchuan Kan, Prof. Sunil Bhave, Prof. Sandip Tiwari, and Prof. Farhan Rana for advice and insightful discussions.

I would like to thank SonicMEMS laboratory members who contribute to this research, and create pleasant working environment: Serhan Mehmet Ardanuç, Benyamin Davaji, Vinaya Kumar Kadayra Basavarajappa, Nabil Shalabi, Kwame Amponsah, Sarvani Piratla, Jason Thomas Hoople, Po-Chen Cheng, Sachin Prakash Nadig, Ved Vishwas Gund, Justin Kuo, Tiffany St. Bernard, Alexander Ruyack, Mamdouh Osama Mahmoud Mohamed Abdelmejeed, Leanna Pancoast, Yutong Liu (Jessica), Adarsh Ravi, Di Ni, June-Ho Hwang, Landon Blackledge, Shubham Jadhav, Paolo Arguelles, Shrinidhi Kulkarni, Sahil Gupta, Christine Ou, Julien Ajdenbaum, Brian Jeong, Jiahao Zhang, and Yuan Yao. This work cannot be successful without advice and collaborations from them. I would like to thank friends and colleagues at Cornell School of Electrical and Computer Engineering (ECE): Charles Jeon, Sunwoo Lee, Robin Ying, Melissa White, and Suren Jayasuriya. I am thankful to the Cornell ECE staffs for keeping everything running smoothly: Susan Bulkley, Scott Coldren, Patricia Ann Clark, Patricia L. Gonyea, and Dave Stone.

This work was partially supported by Defense Advanced Research Projects Agency (DARPA). I would like to thank DARPA program managers, who gave critical feedback and insightful advice: Dr. Robert Lutwak, the DARPA program manager of

Micro-Technology for Positioning, Navigation and Timing (Micro-PNT): The Primary and Secondary Calibration on Active Layer (PASCAL) program, Dr. Troy Olsson, the DARPA program manager of Near Zero Power RF and Sensor Operations (N-ZERO) program, and Dr. Ronald Polcawich, the DARPA program manager of The Precise Robust Inertial Guidance for Munitions (PRIGM): advanced inertial micro sensor (AIMS) program. This work was partially supported by Jacobs Scholar Fellowship, and Thailand Ministry of Science and Technology Scholarship. This work was performed in part at the Cornell NanoScale Facility, a member of the National Nanotechnology Coordinated Infrastructure (NNCI), which is supported by the National Science Foundation (Grant NNCI-1542081). This work made use of the Cornell Center for Materials Research Shared Facilities which are supported through the NSF MRSEC program (DMR-1719875).

Friends, colleagues, and mentors have supported me all through the Ph.D. program at Cornell. I would like to thank Pichaya Damrongpiwat (Mint), Justin Kuo, and Graeme Kay (Ideal Partner Group Ltd., Part.) for editing this dissertation. I would like to thank friends who make Ithaca become memorable place: Chinawat Isradisaikul (Chin), Bunyarit Meksiriporn (Pao, Mackay), Kullachate Muangnapoh (Oath), Chairat Polmuk (Som, Sam), Pakawat Phalitnonkiat (Kun), Sra Chuenchoksan, Rina Tse, Sunsiree Kosindesha (Wahn, Sandy), Ithipong Assaranurak (Billy), Sirapat Techaruvichit (Ming), Kittikun Songsomboon (Ob, Chris), Mingtao Wu (Baymax), Chalermpat Pariya-Ekkasut (Nong), Siraphat Taesuwan (Fay), Thapakorn Jaroentomeechai (Hize, Tommy), Pornteera Osottanakorn (Ploy), Korakot Janteerasakul (Bua), Vasu Jarerattanachat (Bank), Pichaya Damrongpiwat (Mint), Weerin Chantaroje (Ped), Ravi Laohasurayodhin (Note), Rawinthira Narksusook (Jelly), Sauvanithi Yupho (Nid), Chotiwut Sukpradub (Keng), Ratima Lueangwattanakit (May), Ramita Pinsuwannakub (May), Sireemas Maspong (Gift, Mas), Tyson Ruengsuksilp,

Chawisara Uswachoke (Belle), Fikri Pitsuwan (Fik), Benjamin Chiaravanont (Ben), Win Tripop, Anuntachai Vongvanij (Ben), Ornwara Tritrakarn, Natthatida Thaweecharoen (Namhom), Somhathai Hanwatanachai (Zara), Patchara Suensilpong, Suttinan Doungpummesr (Pond), and many other people. I would like to thank lecturers and teaching assistances in the Korean Language Program at Cornell University: Meejeong Song, Seunggon Jeong, Hankyul Kim, Nari Yoon, and Jahyon Park. I would like to thank Nahong Kim for her love and patient. We have shared love, happiness, and sadness throughout the whole Ph.D. program.

Finally, I would like to thank my family members, especially my parents: Wanaporn Saksipatana and Amorn Pinrod for their love, support, and encouragement.

TABLE OF CONTENTS

LIST OF FIGURES

LIST OF TABLES

CHAPTER 1

INTRODUCTION

1.1 Sensors and wireless transmitters for Internet of things (IoT)

The rapid growth of the Internet of things (IoT) has significantly increased the demand for better sensors and wireless transmitters [1]–[4]. It is forecasted that as much as 25 billion IoT devices, including autonomous cars, unmanned aerial vehicles (UAVs), and robots will be in use by 2021 [4]. These IoT devices integrate various sensors to gather information from the physical world and to communicate with the internet through wireless transmitters. Although commercially-available sensors and wireless transmitters are widely used in IoT devices, there are numerous instances for which these commercial sensors and wireless transmitters cannot be relied upon.

Piezoelectric microelectromechanical systems (MEMS) technology can be used to improve sensors and wireless transmitters [5]–[7]. MEMS technology integrates complex mechanical and electrical systems into small devices at low cost, size, weight, and power [8], [9]. The piezoelectric effect provides linear reversible electrical-mechanical transduction used in sensors, actuators, resonators, and various devices [5]. Compared to other mechanisms, piezoelectric transduction has high electromechanical coupling coefficient (for example: PZT, k_{33} = 0.72), works in wide range of frequency (for example: GaN, 123 GHz), and is compatible with CMOS integration (for example: AlN) [5]–[7], [10], [11]. Alternative transduction techniques include 1) electrostatic transduction, 2) thermal transduction, and 3) magnetic transduction. First, electrostatic transduction is used in products such as micromirrors, accelerometers, and gyroscopes [8]. However, electrostatic force usually requires a high bias voltage, released structures such as comb drives and parallel plates, and micro- or nano-scale gaps [12], [13]. The released structures and precision gaps may increase fabrication complexity and reduce shock and vibration tolerance. Second, thermal transduction operates at low voltage and

provides a large force, but consumes more power while responding comparatively slowly [8]. Third, magnetic transduction is used in conventional macroscale systems such as motors, generators, loudspeakers, microphones, and telegraphs [14]–[16]. In micro-scale, permanent magnet films usually require high-temperature annealing (> 500 ºC), require thick film (> 1μm), or are prone to oxidation (e.g., Sm-Co and Nd-Fe-B alloy films) [16].

This dissertation presents piezoelectric MEMS sensors and wireless transmitters, developed for specific IoT applications. The research is presented in two areas: microsystems based on bulk lead zirconate titanate (PZT) lateral bimorphs, and high-overtone bulk diffraction wave gyroscopes. In this chapter, background information on piezoelectricity is presented in 1.2, followed by an introduction on each piezoelectric MEMS device in the dissertation organization in 1.3. Chapters 2 - Chapter 7 explain each device in detail.

1.2 Piezoelectricity

The piezoelectric effect is used in this dissertation to design sensors and wireless transmitters described in Chapter 2 - Chapter 7. This section introduces the piezoelectric effect, explains its origin, and discusses piezoelectric materials. The piezoelectric effect is a property of certain solid materials, which converts mechanical stress into an electrical charge, and vice versa [6], [17], [18]. Since its discovery by Pierre Curie and Jacques Curies in 1880, piezoelectricity has attracted research interests in fundamental physics, material development, and applications [6], [19]. Sensors can be designed to use the direct piezoelectric effect, which generates output voltage as a response to mechanical stress. On the other hand, actuators can be designed to use the converse piezoelectric effect, which generates strain from an input voltage. Various devices such as filters and resonators make use of the piezoelectric effect in both directions.

1.2.1 Piezoelectric mechanism

Piezoelectric effects can occur in crystals, ceramics, 2D materials, and other solids if their microscopic structures have a sufficiently low symmetry [6], [17], [18]. For example, inversion symmetry prohibits materials from being piezoelectric because the total electric dipole moment cancels out. The direct piezoelectric effect occurs when the geometric change at the microscopic level due to strain creates an internal electric dipole moment, which further generates voltage, charge, or current. The converse piezoelectric effect occurs when an external electric field is applied and the material responds by changing its dimension at the microscopic level.

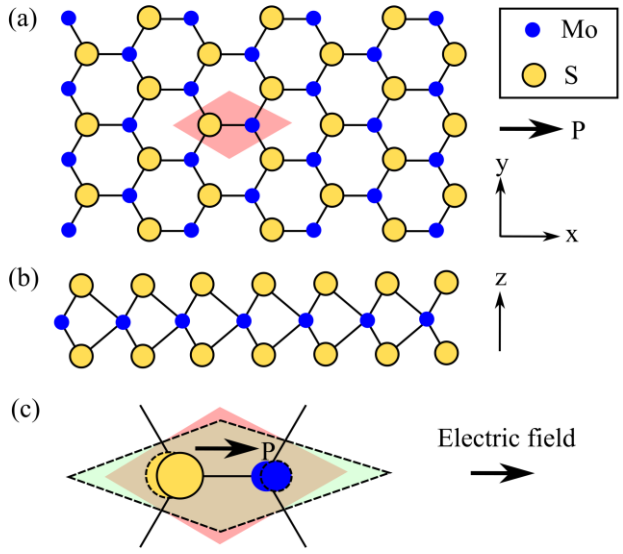

Figure 1.1 2D piezoelectric material (2H-MoS_2), drawn not to scale. (a) The top view shows molybdenum (Mo) atoms in blue and sulfur atoms in yellow. A primitive cell is labeled in red. (b) The side view shows that sulfur atoms are not in the same plane as molybdenum atoms. (c) Direct piezoelectric effect: electric dipole is generated when the dimension is changed in the x-direction. Converse piezoelectric effect: a primitive cell is elongated if an external electric field is applied [20]–[22].

An example of piezoelectric 2D material (monolayer molybdenum disulfide in trigonal prismatic form, 2H-MoS_2) is shown in Figure 1.1 to visualize its microscopic structure [20]–[22]. Molybdenum atoms are shown in blue, and sulfur atoms are shown

in yellow. From the top view in Figure 1.1a, a primitive cell is shown in a red rhombus, which can span the whole area. The cross-sectional view is shown in Figure 1.1b, where molybdenum and sulfur atoms are in different planes. Figure 1.1c shows an asymmetric primitive cell which comprises of two sulfur atoms on the left and one molybdenum on the right. The asymmetry of the primitive cell leads to piezoelectric effects, following the previous explanation. If an external electric field is applied as shown, Mo-S covalent bonds elongate and cause the primitive cell to stretch, as shown in green. If an external strain is applied such that the primitive cell is stretched into a green rhombus, an internal polarization ***P*** is created. This microscopic change leads to a piezoelectricity of 2H-MoS_2, which is simulated and experimentally confirmed [20], [21].

1.2.2 Piezoelectric materials

Although numerous piezoelectric materials have been developed, only a few of them are widely used due to their desirable material properties. In 1880, the Curie brothers discovered the piezoelectric effect in several crystals, including tourmaline, topaz, quartz, and boracite [19]. Among these materials, only quartz is in use as a piezoelectric material, particularly in frequency reference oscillators and microbalances due to its excellent temperature coefficient [6]. During World War II, Rochelle salt (sodium potassium tartrate tetrahydrate; $NaKC_4H_4O_6 \cdot 4H_2O$) was used in hydrophone transducers instead of quartz for submarine detection because of its high electromechanical coupling [23]. Rochelle salt is also the first known ferroelectric material, which has a spontaneous charge and high dielectric constant [24].

After World War II, piezoelectric materials have been discovered and developed in various forms, including single crystals, polycrystals, ceramics, polymers, composites, and 2D materials. In the 1940s, barium titanate ($BaTiO_3$) was discovered as the first known piezoelectric material in the ceramic form [23], [25], [26]. Previously, scientists believed that polycrystalline materials could not be piezoelectric because the

random crystal direction in each grain cancels out net polarization [25]. The poling process was discovered and revealed that applying an external DC electric field at a high temperature can reorient grain dipole. Thus, barium titanate ceramics become piezoelectric after poling [27], [28]. In the 1950s, lead zirconate titanate ($Pb[Zr_xTi_{1-x}]O_3$ $(0 \leq x \leq 1)$; PZT) piezoelectric ceramics were developed and became more popular than barium titanate due to its higher electromechanical coupling, higher Curie temperature, and for other reasons not stated here [25], [26], [29]. In 1964, high quality single crystal lithium niobate ($LiNbO_3$) was grown using the Czochralski technique [30]. This crystal has a high electromechanical coupling, high quality factor, and low acoustic attenuation, and is thus suitable for surface acoustic wave applications [23]. In 1969, polyvinylidene fluoride ($-(C_2H_2F_2)_n-$; PVDF) was developed as a piezoelectric polymer [31]. In the 1970s and 1980s, zinc oxide (ZnO) and aluminum nitride (AlN) piezoelectric thin films were developed [7]. AlN is widely used in the microelectromechanical system (MEMS) because piezoelectric AlN film deposition is repeatable and CMOS compatible [7]. In addition to the materials discussed here, there are other interesting piezoelectric materials, including lithium tantalate ($LiTaO_3$), gallium nitride (GaN), aluminum nitride-scandium nitride alloy (AlN-ScN), and lead magnesium niobate-lead titanate (PMN-PT) [6], [7].

Although many piezoelectric materials are available, the material of choice can be determined from preferred material properties, which depend on its specific application such as in sensors, actuators, and filters. Examples of common beneficial properties include low cost, compatibility with CMOS integration, high electromechanical coupling coefficient, high electrical resistance, high quality factor, high Curie temperature, and low temperature coefficient. Examples of widely used piezoelectric materials are shown in Table 1.1. In this dissertation, PZT is used in Chapters 2-5, and lithium niobate is used in Chapters 6-7.

Table 1.1: Examples of piezoelectric materials widely used in MEMS.

Material	Form	Interesting properties	Application examples
Lithium niobate ($LiNbO_3$)	Single crystal	Low acoustic attenuation	Surface acoustic devices (SAW)
Quartz (SiO_2)	Single crystal	Zero temperature coefficient	Frequency reference oscillators
Aluminum nitride (AlN)	Single/ Poly crystal	CMOS compatible	Thin film bulk acoustic resonators (FBAR), Inertial sensors, microphones
Lead zirconate titanate ($Pb[Zr_xTi_{1-x}]O_3$, $(0\leq x\leq 1)$; PZT)	Ceramic	High electromechanical coupling coefficient	Actuators, energy harvesters
Polyvinylidene fluoride ($-(C_2H_2F_2)_n-$; PVDF)	Polymer	Soft	Wearable electronics

1.3 Dissertation organization

Table 1.2: Dissertation organization.

Chapter	Applications	Device type	Materials	Frequency	Operate at resonance
2	Near-zero power consumption event detection	Sensors	PZT	5 Hz - 2 kHz	Both
3		Sensors, energy harvesters	PZT	17-700 Hz	Yes
4	In-*situ* MEMS gyroscope calibration	Actuators	PZT	5-150 Hz	No
5	Ultralow frequency (ULF) communication by mechanical motion of magnets	Actuators	PZT	893 Hz	Yes
6	High-overtone bulk diffraction wave gyroscopes	Sensors	$LiNbO_3$	163 MHz	Yes
7		Sensors	$LiNbO_3$	116 MHz	Yes

This dissertation contains seven chapters, as shown in Table 1.1. Chapters 2-5 explain the PZT-bimorph-based microsystems designed for the following applications: 1) near-zero power event detection in Chapter 2-3, 2) gyroscope calibration in Chapter 4, and 3) ultralow frequency (ULF) communication in Chapter 5. Chapters 6-7 examine high-overtone bulk diffraction wave gyroscopes. The rest of this section introduces each chapter by discussing rationale and explaining the designed piezoelectric MEMS devices.

Chapter 2 explains PZT-bimorph-based sensors designed for near-zero power event detection. Battery replacement cost in unattended wireless sensor nodes diminishes economic and societal benefits from information obtained by the sensor nodes [32], [33]. Developing a zero-power sensor suite with a near-zero power wakeup system can potentially prolong wireless sensor node battery life. The near zero-power sensor node solution is presented with piezoelectric sensors and a comparator made of DC tunable threshold electrostatic switches and a nanowatt power CMOS classifier. A sensor suite measuring acceleration, rotation, magnetic field, and sound based on PZT lateral bimorphs is used with NEMS switches or CMOS comparators to detect a desired signal pattern and generate a wakeup trigger. The sensor sensitivities achieved are 0.1 V/g for the accelerometer, 31 mV/Gauss for the magnetic field, 0.31 mV/(°/s) for rotation, and 12.6 V/Pa for resonance microphone. NEMS switches, with threshold voltages in the mV to 15 V range, can combine multiple sensor outputs through multi-gate actuation to detect desired event-specific features. The platform is evaluated in a field test consisting of the detecting of operational modes of an electrical generator. The power consumption for the CMOS comparator is 2-6 nW in the off-state. Successful mode-of-operation classification is demonstrated with no false alarms in 10 hours. With the resonance microphones, examples of electric generator detection at 10 meters and truck detection at 0.5 meters in a rural environment are shown, illustrative of zero-power

wakeup sensors for long-lifetime IoT devices. The sensing also demonstrates the ability to distinguish different targets owing to different signal spectrums.

Chapter 3 explains PZT-bimorph-based sensors and energy harvesters designed for near-zero power event detection. 3D-printed structures integrated with laser-cut spiral PZT bimorphs are used to obtain low mechanical resonance frequencies for energy harvesting and a vibration-activated mechanical switch. This structure is used to realize a battery-less vibration event detector and RF transmitter, using the energy of the vibration and a mechanical switch as a comparator. The low resonance frequency of the 3D-printed mechanical resonators is used to trigger the impulse response of the PZT bimorphs, resulting in an up-conversion of resonance frequencies. RF pulses are generated by an LC resonator and transmitted by a loop antenna for reporting event detection. The 3D-printed structure has resonances as low as 17.5 Hz to 40 Hz, which corresponds to the vibration energy spectrum readily available in the environment. At 40 Hz and 0.75 g excitation, the resulting RF pulse is at a carrier frequency of 10.9 MHz with energy extracted from the bimorph of 0.95 nJ per pulse. As a demonstration of the device, the wireless sensor node is used to identify operational modes of a portable gasoline electric generator.

Chapter 4 explains PZT-bimorph-based actuators designed for gyroscope calibration. Consumer-grade gyroscopes cannot be used for inertial navigation due to their high scale factors and high bias errors [34]. Developing a precise self-calibration system may allow for low-cost gyroscopes to have navigation applications, significantly reducing the cost of navigation grade gyroscopes. Simultaneous extraction of the scale factor and the cross-axis sensitivity of a commercial 6-DOF Inertial Measurement Unit (IMU) is shown using a multi-axis, mm-scale piezoelectric dither stage. The stage is 25.4 x 25.4 x 0.5 mm, with a platform disk of diameter 7.5 mm, onto which the IMU chip is adhesively attached. The mechanical stage with a 3-axis angular dither capability

is used to calibrate a 3-axis gyroscope chip. A combination of piezoelectric and magnetic actuation provides in-plane and out-of-plane motion. The 3-axis dither capability is crucial for fully calibrating the scale factor and bias of a commercial 3-axis MEMS gyroscope. The stage has small inertia, which allows for high bandwidth on-the-fly calibration and tracking of scale factor drift using rotation dither rates and accelerations as high as 100 deg/sec and 90 m/s^2, respectively. The measured magnetically-actuated dither stage scale factor in the out-of-plane mode is 0.250 (^{o}/s)/mA as a function of current, or 5.57 x 10^{-2} (^{o}/s)/Hz as a function of frequency. The power consumption of the magnetic stage is 33.5 mW/mdeg. The maximum dither angle obtained is 8.95 mdeg at 300 mW. The impact of high power can be minimal on periodic low duty-cycle calibration. A pathway to improving commercial IMUs is demonstrated, reaching performance needed for personal navigation.

Chapter 5 explains PZT-bimorph-based actuators designed for ULF communication. The rationale is that most commercial wireless transmitters use radio waves in the megahertz and gigahertz ranges, which are absorptive in conductive media and reflective at interfaces between media with different impedances [35]–[38]. Therefore, reliable wireless communication cannot be achieved when media are conductive or reflective when operated underwater or in underground environments, or due to communication between air and underwater interfaces. An ultralow frequency (ULF: 300 Hz - 3 kHz) magnetic induction (MI) can wirelessly communicate through soil, water, and air with low absorption, refraction, and reflection. However, conventional ULF MI loop antenna transmitters are several meters in size to achieve low resonance frequencies. Here, a small (2.4 cm^3) and lightweight (2.7 g) mechanical ULF transmitter is achieved by using a permanent magnet actuated by a PZT dither stage. The magnet is driven in an angular oscillation resonance mode by in-plane PZT bimorph actuators. The mechanical motion of the magnet generates time-varying

magnetic fields, which can be used for wireless communication. With a drive voltage of 0.5 V and power of 1.8 μW, the transmitter can communicate up to 20 m while using a commercially available receiver. The ULF transmitter operates with a ULF MI at 893 Hz with a modulation bandwidth of 2.4 Hz. Transmission over 1 m to a loop antenna receiver with on-off keying (OOK) and amplitude modulation (AM) is demonstrated. Due to low absorption, refraction, and reflection, this transmitter potentially allows for direct communication from air to underwater and underground. The ULF transmitters are suitable for use in unmanned aerial vehicles and IoT devices because of their small size, and low power consumption.

Chapters 6-7 examine high-overtone bulk diffraction wave gyroscopes. Chapter 6 presents the experiment that led to the discovery of the high-overtone bulk acoustic wave gyroscopes. Chapter 7 seeks to explain in theory the operation of the bulk diffraction wave gyroscope. The rationale is that commercial MEMS Coriolis vibratory gyroscopes are sensitive to high levels of shock since its released proof mass can impact surrounding structures [39]. Developing high-shock tolerant gyroscopes allows for various applications such as to increase safety levels in smart automobiles, to aid in space exploration, and to enhance military technology.

High-overtone bulk diffraction wave gyroscopes utilize the Coriolis force on diffracted bulk ultrasonic waves in lithium niobate piezoelectric substrate in order to measure rotation. Using diffracting bulk waves eliminates the need for released spring and masses, enabling operation in extreme shock and vibration. The gyroscope uses interdigitated electrodes that excite thickness-mode resonances in a lithium niobate substrate. The diffraction of pressure and shear waves occurs due to finite electrode aperture. The shear waves undergo Coriolis force modified reflections, with modified waves transduced at receiver interdigitated transducers. The measured unamplified

gyroscope scale factor is 191 μV/(deg/s), which is one of the largest scale factors reported for an all-solid-state gyroscope.

CHAPTER 2

ZERO-POWER SENSORS WITH NANOWATTS CLASSIFIERS FOR WAKE-UP SENSING

2.1 Introduction

Reducing power consumption is important for the Internet of Things (IoT), especially in applications with a large number of IoT devices such as smart cities, smart agriculture, and security [40]. Directly connecting these IoT devices to a power line is impractical in many applications [3]. Wirelessly powered IoT devices such as passive RFID tags are powered by an interrogating RF signal and send data back by scattering. These devices can work only in the presence of the interrogating RF signal [41]. Energy harvesting schemes utilizing solar, RF, and vibrational energy may enable continuous operation, but the energy sources are often not available or not reliable under all scenarios [3]. Batteries serve as reliable power sources to IoT devices, but battery life is generally limited and battery replacement can be costly [42].

In many applications, battery powered IoT devices are deployed to monitor only occasional pertinent events such as intruders, vehicles, pests, precipitation, etc. If the relevant events are infrequent, using low power monitoring to detect events and send wake-up triggers to turn on power-hungry parts such as cameras and radios can extend battery life. Developing near-zero power active monitoring systems with power consumption less than the battery leakage (10-100 nW) can extend device operation life when powered with a typical compact battery [42]. Alternatively, it can work forever if the harvested energy is more than the power consumed.

The pertinent events can be detected by processing various signal modalities such as vibration [43], [44], infrared [45], light [46], RF [47]–[49], temperature [50], [51], or a fusion of several sensors [52], [53]. Among these signal sources, sound is one of the most suitable for low power event detection. Sound contains high amounts of

relevant information about the environment and requires less computation than video or image processing, specially in places with low light.

Low power event detection by sound has been shown previously [54]–[58]. Jeong *et al*. used a MEMS microphone with a classifier chip to detect events, but the microphone needs DC bias and has low sensitivity (18 mV/Pa with 12V bias) [54]. References [55]–[58] show microphones with a resonance structure, but the sensitivity is still relatively small (< 0.6 V/Pa) and microphones have high resonance frequencies (> 430 Hz) which may not be suitable to detect sounds from low frequency sources such as trucks, generators, and machines.

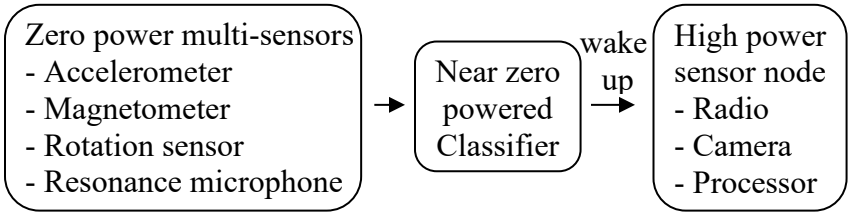

Figure 2.1: Block diagram of the zero power multisensor platform.

In this chapter, a near zero-power "alert but not awake" solution for monitoring time critical events is presented as shown in Figure 2.1 [42], [52], [53], [59]. The sensors monitor the environment continuously, utilizing energy from the incoming signal, while near zero-power classifiers detect events of interest and send a wakeup trigger to a high-power sensor node. The sensors made of piezoelectric materials hold the promise of sensing signals without *any* power consumption, owing to a charge being generated as a result of strain in the materials. The sensor suite measures acceleration, rotation, magnetic field, and sound based on piezoelectric lead zirconate titanate (PZT) lateral bimorphs [52], [53], [59]. For sound sensing, low resonance frequency microphones with high sensitivity for increasing the event detection range are developed [59]. The resonance frequency can be tuned to match desired sources with the ability to reach the

low frequencies of sound from most man-made machines. For signal classifiers, two types of near zero-power classifiers are shown which are low-power CMOS ICs and multi-gate NEMS switches. The classifiers compare a weighted combination of sensor outputs to allow the tuning of the system for the identification of a desired signal pattern. A system application for detecting gasoline electric generators, cars, and trucks in the vicinity is shown.

In the following section of this chapter (2.2), the PZT lateral bimorph which is the building block of the zero-power sensors is discussed. Next, each zero-power sensor design and characterization are discussed in 2.3. These sensors consist of accelerometers which are discussed in 2.3.1, magnetometers which are discussed in 2.3.2, angular accelerometers which are discussed in 2.3.3, and resonance microphones which are discussed in 2.3.4. Next, near zero power classifier topologies and measurements are discussed in 2.4. The classifier measurements are 1) NEMS switch classifiers integrated with accelerometers tested on a shaker table, as discussed in 2.4.1, 2) CMOS classifiers integrated with multiple sensors for detecting gasoline electric generators, as discussed in 2.4.2, and 3) CMOS classifiers integrated with resonance microphones for detecting gasoline electric generators, cars, and trucks, as discussed in 2.4.3.

2.2 PZT lateral bimorphs for zero-power sensors

Zero-power sensors are based on PZT lateral bimorphs which are formed by the laser-micromachining of bulk PZT plates with silver electrodes on the top and bottom [60]. Cutting through PZT substrates defines the beam and the proof mass structures, while removing only the top silver electrode defines the sense electrodes and wire bond pads. The fabrication process is explained in Chapter 5. Using an LPKF Protolaser U results in feature sizes as low as 150 μm for 500-μm thick PZT plates. The cross-section of the sensing bimorph, with thickness h and polarization $\vec{P}$, is shown in Figure 2.2a which consists of two output electrodes on the top, and one ground electrode at the

bottom. The top view of a laterally bent sensing bimorph with dimensions is shown in Figure 2.2b.

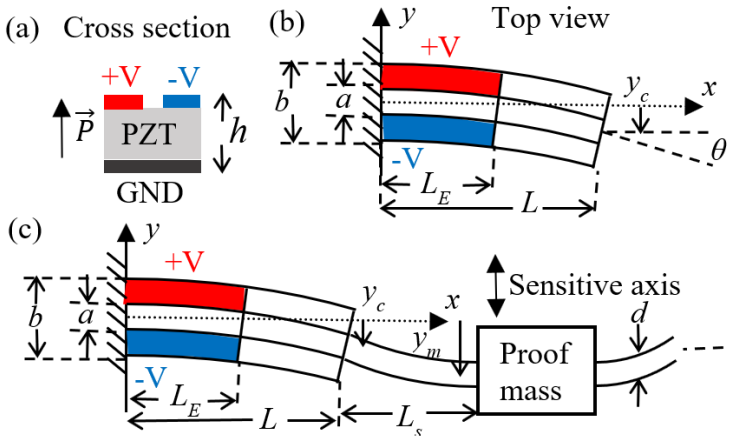

Figure 2.2: (a) PZT in-plane sensing bimorph cross-section with thickness h, and polarization $\vec{P}$. The bottom electrode is grounded, and top electrodes are outputs. (b) Top view of a laterally bent sensing bimorph with tip displacement y_c. (c) Top view of the sensing bimorph with a cantilever spring in a clamped-guided configuration.

Constraining a proof mass in a clamped-clamped configuration with multiple sensing bimorphs (Figure 2.2c) reduces cross-axis sensitivity. Sensing bimorphs in this configuration can be considered as a clamped-guided beam spring [8]. However, a uniform piezoelectric bimorph in a clamped-guided beam configuration will produce an opposite charge for the halves closest to the anchor and proof mass. Separated electrodes on each half are possible, but extra routing is required. Alternatively, a smaller cantilever spring with height d and length L_s can be added between the cantilever tip and the proof mass as shown in Figure 2.2c. To illustrate the operation, a 3D model of the sensing bimorph with a cantilever spring is shown in Figure 2.3a. When the bimorph deflects in the clamped-guided configuration, the stress in the x-direction is shown in Figure 2.3b. The tensile and compressive stress switch the polarity at the deflection point, where the bimorph connects to the cantilever spring.

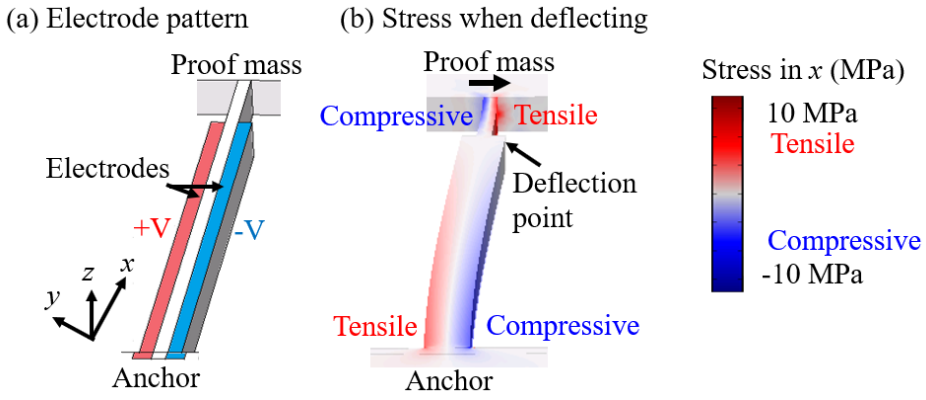

Figure 2.3 3D model of the sensing bimorph with a cantilever spring in a clamped-guided configuration (a) Electrode pattern (b) Stress distribution when deflecting.

In order to maximize the bending moment, the length of the spring is chosen to match the angle at the tip with the condition

$$\theta = \frac{F}{EI}\frac{L^2}{2} = \frac{6FL^2}{Etb^3} = \frac{6FL_s^2}{Etd^3}, \tag{2.1}$$

where dimension variables are shown in Figure 2.2c. The condition leads to the length of the spring

$$L_s = L(d/b)^{3/2}. \tag{2.2}$$

The displacement of the sensing cantilever is reduced from the displacement of the proof mass resulting in

$$y_c = \frac{y_m}{1+(d/b)^{3/2}}. \tag{2.3}$$

The output voltage of the sensing bimorphs can be calculated from piezoelectric constitutive equations

$$(a)\ [S] = [s^E][T] + [d]^t[E], \qquad (b)\ [D] = [d][T] + [\epsilon^T][E], \tag{2.4}$$

where $[S]$ is a strain tensor, $[T]$ is a stress tensor, $[E]$ is an electric field vector, $[D]$ is an electrical displacement vector, $[s^E]$ is a compliance tensor measured under a constant

electric field, $[\epsilon^T]$ is an electrical permittivity matrix measured under constant stress, and $[d]^T$ is a transposed piezoelectric coefficient tensor.

Considering only the piezoelectric coefficients that are relevant to the in-plane bending of the lateral bimorph, the constitutive equations (2.4) are reduced to

$$(a)\ S_{11} = s_{11}^E T_1 + d_{31} E_3, \qquad (b)\ D_3 = \epsilon_3^T E_3 + d_{31} T_1. \tag{2.5}$$

The constitutive equations (2.5) can be solved by substituting T_1 from (2.5)a into (2.5)b. The electric displacement D_3 can be written as

$$D_3(x,y) = \epsilon_3^T \left(1 - \frac{d_{31}^2}{s_{11}^E \epsilon_3^T}\right) E_3 + \frac{1}{s_{11}^E} d_{31} S_{11}(x,y). \tag{2.6}$$

From Euler–Bernoulli beam theory, in-plane strain $S_{11}(x,y)$ in the bending cantilever is

$$S_{11}(x,y) = \frac{s_{11} y_c k_c}{I}(L-x)y = \frac{3y_c}{L^3}(L-x)y, \tag{2.7}$$

where y_c is the tip displacement, L is the cantilever length, k_c is the cantilever spring constant, and I is the second moment of inertia. The parameters for the cantilever geometry are illustrated in Figure 2.2. The cantilever spring constant is

$$k_c = \frac{3I}{s_{11} L^3}, \tag{2.8}$$

and the second moment of inertia I is

$$I = \frac{1}{12} h b^3, \tag{2.9}$$

where t is the thickness of the PZT, and b is the width of the cantilever, illustrated in Figure 2.2. Substitute $S_{11}(x,y)$ from (2.7) into (2.6), and the displacement becomes

$$D_3(x,y) = \epsilon_3^T \left(1 - \frac{d_{31}^2}{s_{11} \epsilon_3^T}\right) E_3 + \frac{1}{s_{11}^E} d_{31} \frac{3y_c}{L^3}(L-x)y. \tag{2.10}$$

Using Gauss' law, the charge generated on the top electrodes q can be found. From Figure 2.2, the charge accumulated on the +V electrode is

$$q_+ = \int_{y=a/2}^{b/2} \int_{x=0}^{L_E} D_3(x,y)\, dx\, dy, \tag{2.11}$$

The charge accumulated on the +V electrode is calculated by substituting $D_3(x,y)$ from (2.10) and (2.11) as

$$q_+ = \int_{y=a/2}^{b/2} \int_{x=0}^{L_E} \epsilon_3^T \left(1 - \frac{d_{31}^2}{s_{11}^E \epsilon_0 \epsilon_r}\right) E_3 + \frac{d_{31}}{s_{11}^E} \frac{3y_c}{L^3} (L-x) y\, dx\, dy. \tag{2.12}$$

After integrating and simplifying, the charge accumulated on the +V electrode q_+ is

$$q_+ = \epsilon_3^T \left(1 - \frac{d_{31}^2}{s_{11}^E \epsilon_3^T}\right) L_E \frac{\mathrm{b-a}}{2} E_3 + \frac{d_{31}}{s_{11}^E} \frac{3y_c}{L^3} \left(L L_E - \frac{L_E^2}{2}\right) \frac{b^2 - a^2}{8}. \tag{2.13}$$

The charge can be written as a function of voltage by substituting $E_3 = V/h$ as

$$q_+ = \left[\epsilon_3^T \left(1 - \frac{d_{31}^2}{s_{11}^E \epsilon_3^T}\right) L_E \frac{\mathrm{b-a}}{2} \frac{1}{h}\right] V + \left[\frac{d_{31}}{s_{11}^E} \frac{3}{L^3} \left(L L_E - \frac{L_E^2}{2}\right) \frac{b^2 - a^2}{8}\right] y_c, \tag{2.14}$$

This equation can be rewritten as

$$q_+ = C_0\, V + \Gamma_Q y_c, \tag{2.15}$$

where the modified bimorph capacitance C_0 is

$$C_0 = \epsilon_3^T \left(1 - \frac{d_{31}^2}{s_{11}^E \epsilon_3^T}\right) \frac{L_E (b-a)}{2h}, \tag{2.16}$$

and the tip displacement-charge coefficient Γ_Q is

$$\Gamma_Q = \frac{d_{31}}{s_{11}^E} \frac{3}{L^3} \left(L L_E - \frac{L_E^2}{2}\right) \frac{b^2 - a^2}{8}. \tag{2.17}$$

From (2.15), the in-plane PZT bimorph can be considered as a charge source connected in paralleled with a capacitor [52], [53], [59]. In near zero power sensor applications,

the sensors are connected to NEMS switches or CMOS classifiers, which can be modeled as resistive and capacitive loads as shown in Figure 2.4 [52], [53], [59].

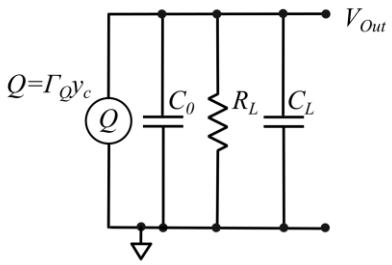

Figure 2.4 A circuit diagram shows PZT in-plane sensing bimorph output voltage with resistive and capacitive load.

To analyze the circuit in Figure 2.4, the equation for voltage and current in the Fourier domain can be obtained by taking a derivative on both sides of (2.15) as

$$I = j\omega C_0\, V + j\omega \Gamma_Q y_c. \tag{2.18}$$

The current I can be substituted by the current that flows to capacitance and external loads as

$$-\frac{V}{R_L} - j\omega C_L V = j\omega C_0\, V + j\omega \Gamma_Q y_c. \tag{2.19}$$

The output voltage is

$$V_{out} = -\frac{\Gamma_Q y_c}{(C_L+C_0)} \left(\frac{j\omega R_L(C_L+C_0)}{1+j\omega R(C_L+C_0)}\right). \tag{2.20}$$

When the frequency is much greater than 1/RC time constant ($\omega \gg 1/RC$), the output voltage V_{out} is

$$V_{out} = -\frac{\Gamma_Q y_c}{(C_L+C_0)}, \tag{2.21}$$

where Γ_Q and C_0 are explained in (2.16) and (2.17). The source capacitance of the bimorphs presented here is in the range of 100-200 pF. This source capacitance is much

larger than the pad capacitance (including parasitic capacitance from ESD protection) ensuring that signals are not degraded by load and parasitic capacitance.

2.3 Zero-power sensors

Zero-power sensors are designed based on the PZT lateral bimorph which is discussed in the previous section. The sensors are designed to measure signals by using the energy from the signal and generating an output voltage by piezoelectric transduction. The zero-power sensors consist of accelerometers which are discussed in 2.3.1, magnetometers which are discussed in 2.3.2, angular accelerometers which are discussed in 2.3.3, and resonance microphones which are discussed in 2.3.4.

2.3.1 Accelerometers

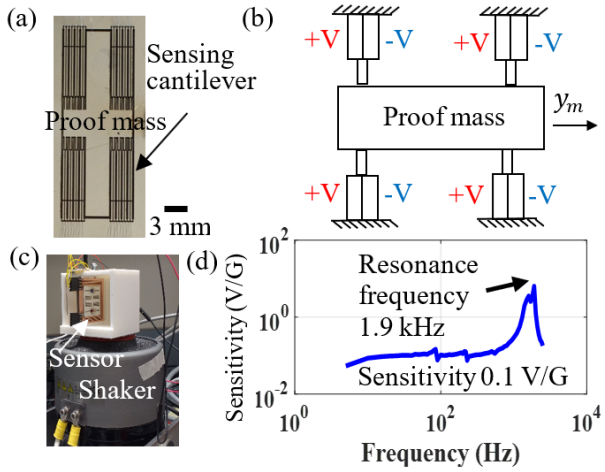

Figure 2.5 (a) Photograph of PZT accelerometer (b) Sketch of simplified model (c) Photograph of accelerometer calibration on VR shaker table (d) Bode plot sensitivity of accelerometer.

The accelerometer design consists of 16 sensing bimorphs. A photograph of a fabricated sensor is shown in Figure 2.5a. The sketch for the accelerometer electrode combination is shown in Figure 2.5b. The equation of motion is given by

$$m\,\ddot{y}_f = m\,\ddot{y}_m + b\dot{y}_m + k y_m, \tag{2.22}$$

where m is the total proof mass, y_m is the proof mass displacement in the y (sensitive) direction relative to a frame. $\ddot{y}_\mathrm{f}$ is acceleration of the frame, b is the damping coefficient, and k is the total spring constant. Equation (2.22) can be solved in a frequency domain to get the proof mass displacement,

$$y_m = \frac{m}{k}\frac{\omega_0^2}{-\omega^2+2j\gamma\omega_0\omega+\omega_0^2}\ddot{y}_\mathrm{f}, \tag{2.23}$$

where $\omega_0 = \sqrt{k/m}$ is the resonance frequency of the spring mass system and $\gamma = B/(2\sqrt{km})$ is the damping ratio.

By design, the spring constant is 28.4 kN/m, the proof mass is 290 mg, and the resonance frequency is 1.5 kHz. The accelerometer is calibrated by mounting on a Vibration Research (VR) shaker table with a 3D-printed holder (Figure 2.5c). The measured accelerometer flat band sensitivity is 0.1 V/G with a resonance frequency of 1.9 kHz (Figure 2.5d).

2.3.2 Magnetometers

Magnetometers are made by adhesively bonding two permanent magnets, pointing in opposite directions, on two separate clamped-clamped PZT beams (Figure 2.6a). The magnetometer schematic is shown in Figure 2.6b. Two permanent magnets are attached, on two separate clamped-clamped beams, pointing in opposite directions to cancel out torque caused by rotation.

Force and torque on the permanent magnet in an external magnetic field B are

$$\vec{F} = \nabla\left(\vec{m}_s \cdot \vec{B}\right), \tag{2.24}$$

$$\vec{\tau} = \vec{m}_s \times \vec{B}, \tag{2.25}$$

where $\vec{F}$ is the force on the sensing magnet, $\vec{m}_s$ is the total magnetic dipole moment of a magnet, and $\vec{\tau}$ is the torque applied on the magnet. Since magnetic force (2.24) can only measure the gradient of a magnetic field, magnetic torque (2.25) is used to produce

a linear response to any magnetic field. The sensitive direction of the assembled magnetometer is perpendicular to the north-south axis of the magnet. Connecting electrodes as shown in Figure 2.6b cancels out the charge generated due to linear and angular acceleration of the masses, and makes the output proportional to the magnetic field alone.

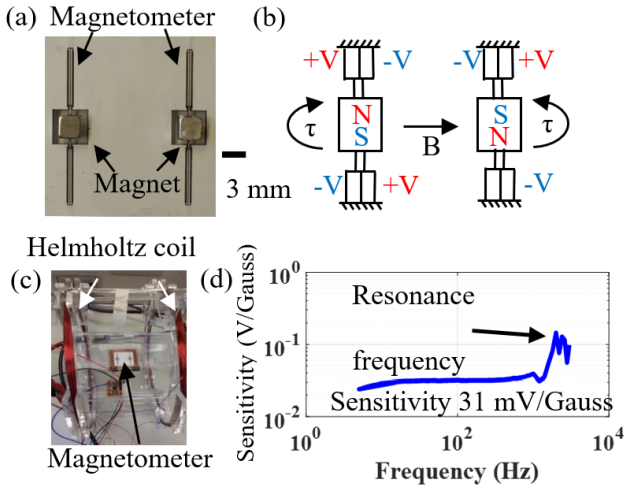

Figure 2.6 (a) Photograph of PZT magnetometer (b) Sketch of magnetometer (c) Magnetometer calibration setup with Helmholtz coil (d) Bode plot sensitivity of magnetometer.

The photograph of our measurement setup is shown in Figure 2.6c. The magnetometer is calibrated by a Helmholtz coil with 100 turns on each coil. The spacing between coils and coil radius is 10 cm. The coil is driven by an Agilent 33500B function generator. The sensitivity measurement is calibrated by a commercial TI DRV425 fluxgate magnetic-field sensor. The calibrated sensitivity is shown in Figure 2.6d. The flat band sensitivity is 31 mV/Gauss, the resonance frequency is 1.6 kHz, and the high pass pole is 10 Hz.

2.3.3 Angular accelerometers

A set of eight bimorphs and proof masses are connected to obtain a zero-power rotation sensor (Figure 2.7a) by measuring the angular acceleration during rotation. The

geometry and the electrical configurations cancel the cross-axis coupling while maximizing sensitive axis output without active amplifications. Rotation induced acceleration on the proof mass is given by

$$y_m(j\omega) = \frac{m}{k}\frac{\omega_0^2}{-\omega^2+2j\gamma\omega_0\omega+\omega_0^2} j\omega\,\Omega R, \tag{2.26}$$

where Ω is the external rotation rate, and R is the radius of the sensor proof mass measured from the sensor center. The rotation sensor is calibrated on an Acutronic BD122 rate table at 30 Hz. The sensitivity is 0.3 mV/(°/s) (Figure 2.7b).

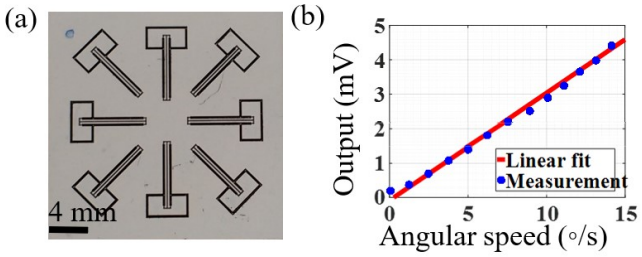

Figure 2.7 (a) Photograph of PZT rotation sensor (b) Plot of sensitivity calibration on Acutronic BD122 rate table at 30 Hz angular dither.

2.3.4 Resonance microphones

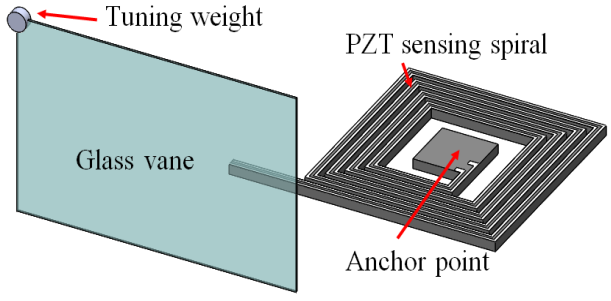

Figure 2.8 3D model of the tunable microphone.

The tunable zero-power microphone consists of a sensing lead zirconate titanate (PZT) spiral, a glass vane, and a tuning weight as shown in Figure 2.8. The PZT spiral helps to achieve the low resonance frequency zero power sensing. It converts energy

from incoming sound to an electrical signal without consuming external power. The spiral design increases output capacitance and decreases resonance frequency while keeping the device size small. The thin glass vane enables the extrac tion of sound from a larger area, and the tuning mass adjusts the microphone resonance frequency to match with the sources.

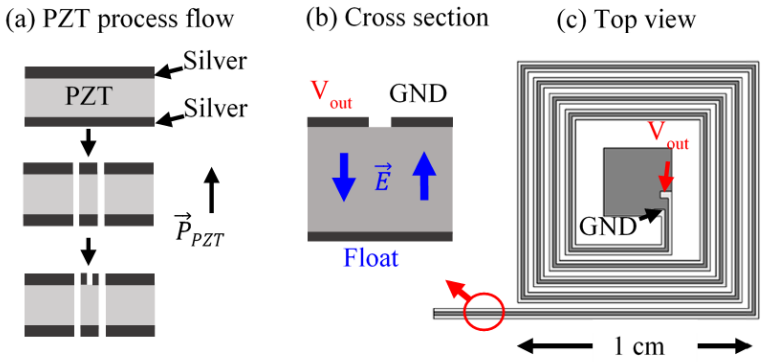

Figure 2.9 PZT sensing coil details (a) PZT laser-micromachining process (b) Cross-section of the cantilever (c) Top view of the sensing spiral.

The PZT laser-micromachining fabrication process flow is shown in Figure 2.9a [60]. The substrate is a 0.5-mm thick APC 840 bulk PZT plate with silver on the top and bottom. The mechanical structure and electrodes are formed by selectively raster scanning a UV laser with an LPKF Protolaser U. Figure 2.9b shows the cross-section of a PZT substrate patterned for sensing with an output electrode (V_{out}) and ground electrode (GND) on the top, whereas the bottom electrode is left floating. Bending the PZT spiral in-plane results in an output voltage [52], [53]. This structure can also be used as an actuator [61], [62]. The top view of the PZT sensing spiral is shown in Figure 2.9c. The anchor point with two wire bond pads is at the middle. Two electrodes run through the spiral.

The microphone components comprised the PZT spiral, glass vane, and tuning weight (Figure 2.10). The glass vane is laser machined by a MicroLux Laserknife 2525

CO_2 laser cutter from a #0 cover slip and attached to the PZT spiral by a UV-activated cyanoacrylate adhesive. The tuning mass is either magnets or clay. Changing the location of the magnet or clay mass can shift the resonance frequency down by up to 15% to match with the source of interest.

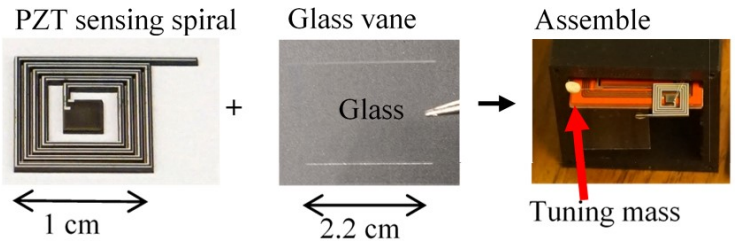

Figure 2.10 Assembly process photographs consist of a PZT sensing spiral, cut glass, and fully assembled microphone with frequency tuning mass.

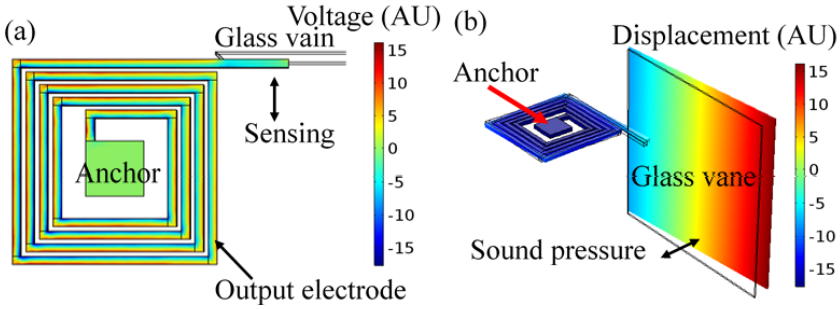

Figure 2.11 Microphone simulation (a) Voltage on top electrode (b) Fundamental vibration mode shape.

The microphone design is investigated by COMSOL finite element simulation software. First, the open circuit voltage when applying a force at the tip of the PZT spiral is studied by a stationary study (Figure 2.11a). The electrode pattern location is optimized for maximum and minimum voltages. The resonance mode shape is studied by eigenfrequency analysis. The fundamental vibration mode shape is shown in Figure 2.11b. The dimensions of the PZT spiral and glass are purposefully chosen to make the simulated resonance frequency 10% higher than the target frequency. After adding the tuning mass, the resonance frequency shifts down to match the desired sound source.

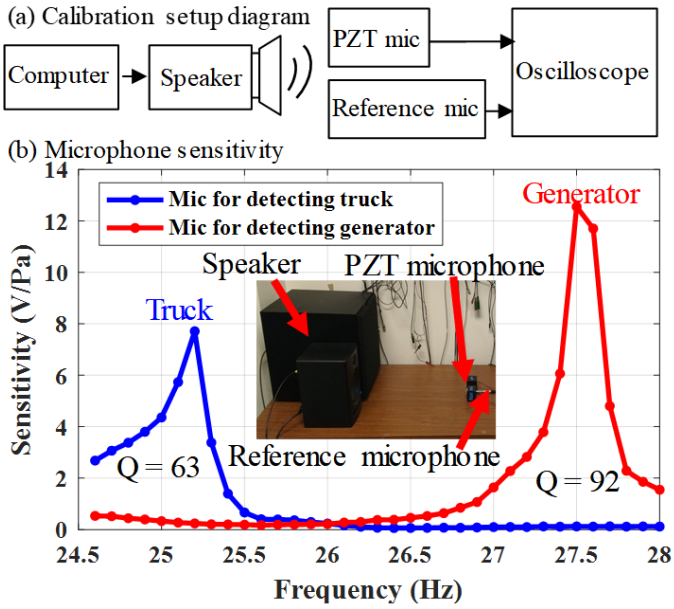

Figure 2.12 (a) Block diagram shows microphone calibration setup (b) Sensitivity of microphone for detecting truck and generator as a function of frequency.

A diagram of the sensitivity calibration setup is shown in Figure 2.12a. The function generator generates a sine wave which is amplified by an amplifier to drive a Presonus Eris E5 studio monitor and Klipsch Reference R-10SW subwoofer. PZT microphones are placed next to a type 4955 low noise Brüel & Kjær reference microphone to monitor the sound pressure level. For calibration purposes, the output of the PZT microphone is buffered by a 3-pF input capacitance JFET OPAMP Texas Instruments TL082. The output from the PZT microphone and reference microphone is recorded by an oscilloscope. An example of PZT microphone sensitivity for detecting generators and trucks is shown in Figure 2.12b, and the calibration setup photograph is shown in the inset. The microphone for detecting generators has a fundamental resonance frequency of 27.5 Hz with sensitivity of 12.6 V/Pa, and the microphone for detecting trucks has a fundamental resonance frequency of 25.2 Hz with sensitivity of 7.7 V/Pa. The sensitivity and lowest resonance frequency compared with previous work are shown in Table 2.1.

Table 2.1: Comparison with previous work on resonance microphones.

	Sensitivity (V/Pa)	***Lowest resonance frequency (Hz)***	***Sensor size***
Jeong *et al.* [54]	0.018	Broadband (>500 Hz)	2 mm x 2 mm
Kusano *et al.* [55]	0.019	430 Hz	5 cm x 5 cm x 1 cm
Baumgartel *et al.* [56]	0.200	900 Hz	4 mm x 11 mm
Zhang *et al.* [57]	0.42	1702 Hz	3.8 mm x 1.8 mm
Reger *et al.* [58]	0.6	430 Hz	No information
This work	**12.6**	**25.2 Hz**	**3.2 cm x 2.2 cm x 1 cm**

2.4 Near-zero powered classifiers

Near-zero powered classifiers are designed to detect signals from the zero-power sensors, which are discussed in the previous section. The classifiers are designed to classify sensor outputs based on characteristics such as frequency and correlation of output from different sensors. Different classifier measurements are 1) NEMS switch classifiers integrated with accelerometers tested on a shaker table as discussed in 2.4.1, 2) CMOS classifiers integrated with multiple sensors for detecting gasoline electric generators, as discussed in 2.4.2, and 3) CMOS classifiers integrated with resonance microphones for detecting gasoline electric generators, cars, and trucks, as discussed in 2.4.3.

2.4.1 NEMS switch classifiers

In this section, NEMS switch classifiers integrated with accelerometers tested on a shaker table are discussed. The NEMS switches used to detect the signals are laterally actuated electrostatic switches. A single photomask process (Figure 2.13a) is used to fabricate the NEMS switches on SOI substrate, where the patterned structures are etched by reactive ion etching (RIE) and released by vapor HF, followed by a metal deposition for reliable switching.

A completed switch is shown in Figure 2.13b. Multiple sized gates are used to actuate the switch to enable a lower turn on voltage and weighing of input signals [63]. Initial testing shows a turn on voltage of 14.36 V and turn off voltage of 14.08 V when actuating with only the largest area gate, as shown in Figure 2.13c. In the shaker table test, a bias lower than the found turn on voltage is applied to the largest area gate and the sensor is connected to the second largest area gate.

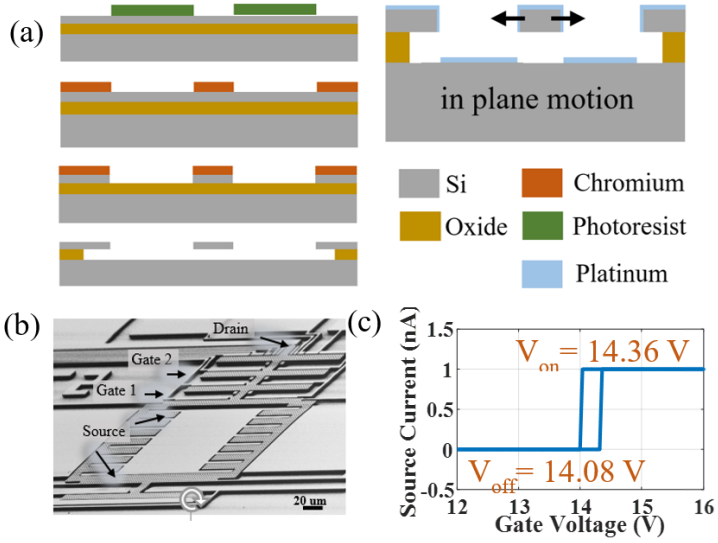

Figure 2.13 (a) Fabrication process flow (b) SEM image of NEMS switch (c) Switching hysteresis plot.

The combined operation of the switch with pre-biased gates generates the digital wake-up signal. Figure 2.14a shows the output from a z-axis PZT accelerometer with added proof mass, directly coupled to the gate of a pre-biased NEMS switch. The resistance of the NEMS switch is shown in Figure 2.14b, when closing the switch to generate a wake-up signal. The switch was pre-biased at 10 V, and the accelerometer was actuated by a shaker table at 280 Hz with an amplitude of 0.12 g. The total power consumption of the wake-up systems is estimated to be < 5 nW, mainly dominated by the 10 V bias power supply leakage current.

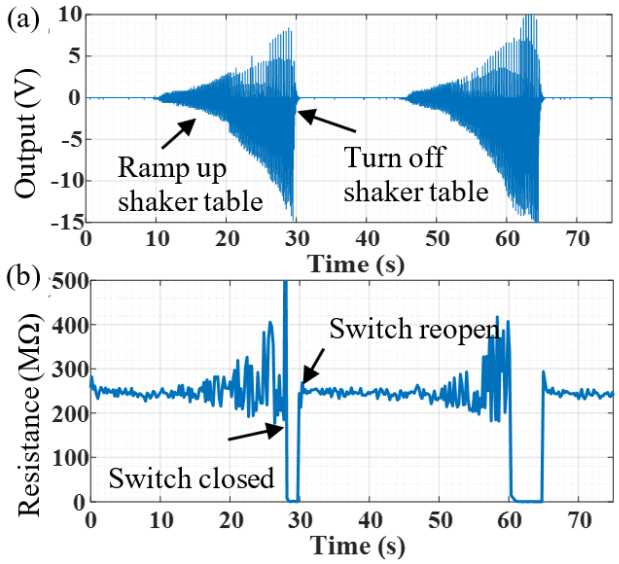

Figure 2.14 (a) PZT accelerometer output voltage. (b) NEMS switch resistance indicating switch close for trigger.

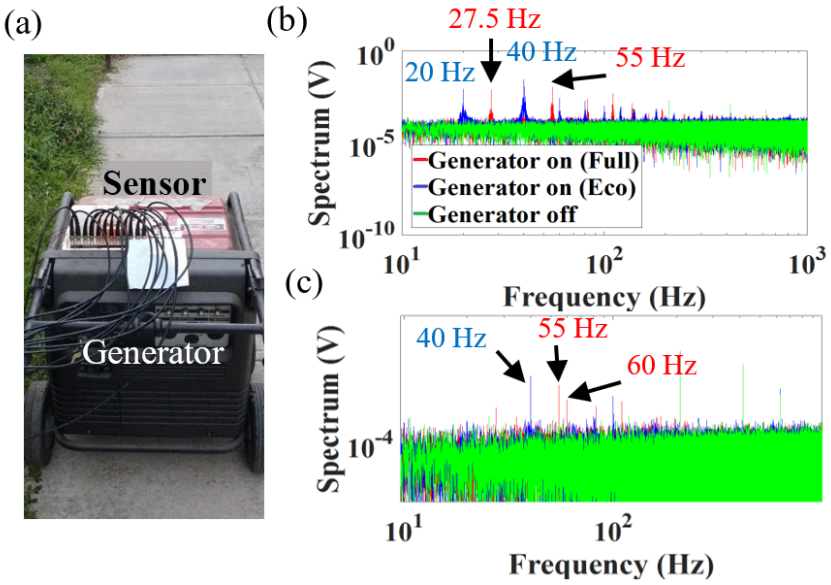

Figure 2.15 Field test by using zero power sensor for generator detection (a) Photograph of sensors on top of generator (b) Spectrum of PZT accelerometer for generator detection (c) Spectrum of PZT magnetometer for generator detection.

In order to measure the efficacy of the zero-power sensor triggered NEMS switches, the fabricated sensors are used to monitor the operation of an internal combustion engine-powered portable electrical generator by measuring the physical

signals (Figure 2.15a). Figure 2.15b-c shows the clear frequency signature difference in the acquired spectrum signal between different modes.

2.4.2 CMOS classifiers in multiple sensors

In this section, CMOS classifiers integrated with multiple sensors for detecting a gasoline electric generator are discussed. In order to combine the analog sensor signals to generate the digital wake-up trigger, the low power comparator given in Figure 2.16 and fabricated in the TSMC 180nm process is used. Up to six sensor signals are AC coupled into sub-threshold NFETs whose drain currents perform a squaring function on the input gate voltage. Four of the six signals can be added together (IN+) while the remaining two perform subtraction (IN-) allowing for not only the combination of signals, but also the extraction of correlation. This CMOS work was performed with Robin Ying, studying with Prof. Alyosha Molnar.

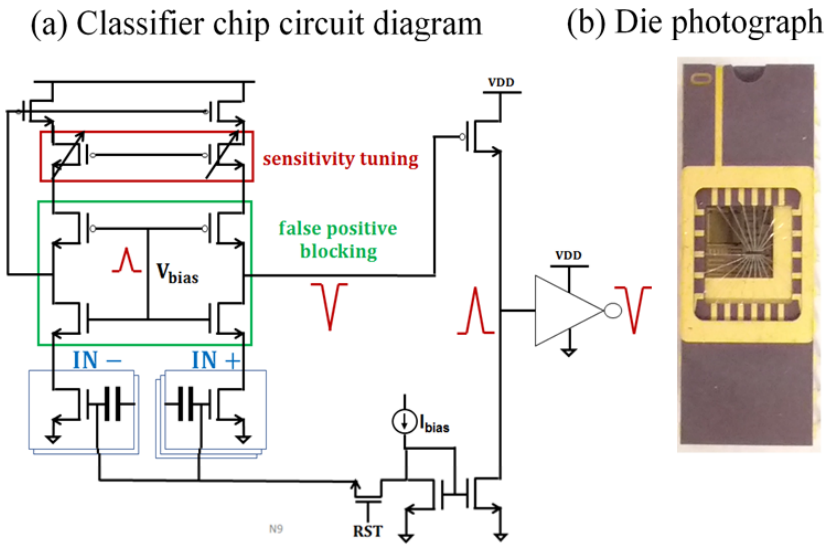

Figure 2.16 Ultra low power CMOS comparator (a) Simplified circuit diagram (b) Wire bonded chip with 0.06 mm^2 active area.

Suppose the feature vector of the correlation of the accelerometer and microphone signals is used, then the two signals can be capacitively coupled together to

generate the signal (A+M). If the signal (A+M) is fed to one of the four addition inputs, and the original A and M signals are fed to the subtraction inputs, then the output is proportional to $(A+M)^2 - A^2 - M^2 = 2AM$. If correlation between signals is not necessary, as is true when detecting whether a generator is on or off, simple squaring using the IN+ inputs will suffice. However, future work will aim to distinguish between generators and cars, which will make use of the correlation. In order to perform the thresholding that generates a digital output, the load impedance is tunable with six-bit control. These bits also control the trade-off between the false-positive rate and signal-detection sensitivity. In the testing, the bit setting is determined such that would cause random false positive triggers, then backed-off by one LSB. Under repeated testing, with a single chip, this calibration setting would not vary. However, between chips, there was slight variation in both the calibration setting and power consumption.

The integrated sensor platform was mounted and tested on an electrical generator (Honda EU6500is) and an automobile. In a ten-hour test with severe wind and rain, as well as various people passing by, there were no false positives while maintaining 100% detection probability and less than 1 ms wakeup delay. Across 8 comparator chips under the testing conditions, off-state power consumption varied from 2 nW to 4.1 nW. Additionally, the probability of detection remained at 100% with significant false positive detection when the sensor suite was reduced to just the accelerometer or just the microphone. This indicates that the combination of signal modalities helped to distinguish the generator signature from false triggers such as wind or people passing by.

2.4.3 CMOS classifiers in resonance microphones

The objective in this test is to distinguish between a generator and a truck with microphones tuned to distinguish between different stimuli. The sensitivity of the ultra-

low power classifier chips is set to optimize for the best probability of detection (POD) with the lowest false alarm rate (FAR). Since the classifier chip transistors are biased in the subthreshold regime (in TSMC 180nm technology), differential signals are used to null the linear term and extract a strong-enough second-order, or squared term. The sensitivity is set by a 6-bit tunable PFET load and is detailed in [53]. To ensure maximum POD with simultaneous minimum FAR, the topology from [53] is slightly modified to include feedback which prevents simultaneous detection of generators and trucks in the presence of only one stimulus. For example, in the presence of a strong generator signature, we do not want a false positive detection of the truck. When the filtering (provided by the generator-tuned microphone) and the squared current generate enough energy to cross a threshold, the ultra-low power classifier triggers a 1 V output indicating that a generator has been detected. At this instant, because this "generator detected" signal controls the V_{bias} node of the truck's classifier circuit, it pulls down the output for the truck classifier if the "generator detected" signal is high regardless of what unwanted signal is coming from the truck-tuned microphone. Note here that false positives can arise in the presence of a strong unwanted signal; however, high POD with low FAR can be realized by reducing sensitivity. The circuit diagram and signal flow for this false-positive blocking mechanism and die photo are shown in Figure 2.16.

Next, the microphones are connected to the classifier chip to test detection. Sound databases of electrical generators, cars, and trucks are provided by a third-party research lab. The sound files are played by a computer. The detection testing block diagram is shown in Figure 2.17a. The setup is tested by playing a frequency sweep from 10-200 Hz. The sound level is adjusted by equalization until the frequency response is flat within ±3 dB from 10-200 Hz. Then, the sound of generators and trucks is played. The output from the classifier chip and reference microphone is recorded by an oscilloscope. Figure 2.17b shows an example of generator detection at 10 m in a rural

environment. The system detects the generator within 10 s while truck detection is not triggered. Figure 2.18 shows an example of truck detection without triggering generator detection at 0.5 m in a rural environment. The power consumption is monitored by a Keithley 2400 SourceMeter and remained under 6 nW throughout the experiment. The achieved POD was 100% for 5 trials and the achieved FAR was 1 per hour.

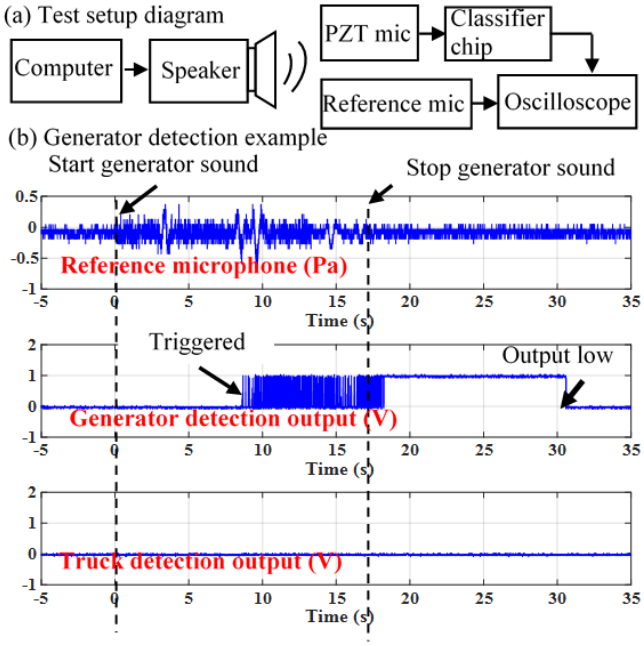

Figure 2.17 (a) Block diagram for testing with recorded sound (b) Example of generator detection.

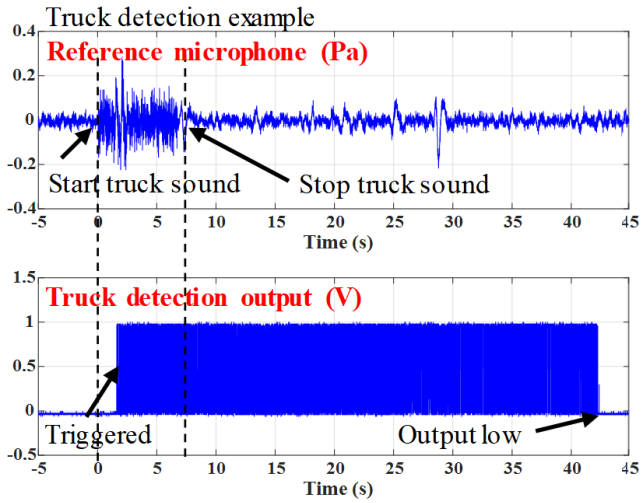

Figure 2.18 Example of truck detection.

2.5 Conclusion

The piezoelectric zero-power sensors suite is demonstrated by using parallel and series combinations of laser micromachined PZT bimorphs that generate voltages in the millivolts to several volts in the signal range of interest. These voltage levels are sufficient to trigger lateral NEMS switches. This binary trigger based on threshold-based activation proves the possibility of a near-zero power wake-up signal for a fully powered sensor suite. The design of acceleration, rotation and magnetic field sensors using the lateral bimorphs is based on a monolithic sensor technology that can be used to make compact sensor systems.

Integration of a PZT multi-sensor platform with a low power CMOS classifier is demonstrated. PZT sensors include accelerometers, rotation sensors, magnetometers, and a microphone. Overall power consumption is as low as 2 nW limited to the power required by the CMOS classifier circuit.

A tunable, high sensitivity, low resonance frequency, zero-power microphone for ultra-low power detection is shown. The sensor is based on a laser-cut lateral PZT bimorph transducer that enables scaling of sensitivity and frequency by increasing the number of arms and sensing masses. The process enables rapid prototyping and potential mass-scale production using several laser cutting tools. The microphone uses a spiral structure which has a low resonance frequency to match man-made machines such as generators, cars, and trucks. Overall power consumption is as low as 6 nW in deeply subthreshold CMOS voltage comparators used as detectors of sufficient voltage. The high sensitivity (12.6 V/Pa) allows detection at a longer range. The size of the sensor is large, but for many applications such as the detection of automobiles or placement of sensors in large building cavities, the sensor size would be acceptable. Generator detection at 10 m, and truck detection at 0.5 m in a rural environment is demonstrated.

CHAPTER 3

HYBRID PZT LATERAL BIMORPHS AND 3D-PRINTED SPRING-MASS RESONATORS FOR BATTERY-LESS RF TRANSMISSION AND VIBRATION IDENTIFICATION

3.1 Introduction

The Internet of Things (IoT) is comprised of sensors reporting data to central data processors for enhancing safety, efficiency, and lifetime of infrastructure such as transportation and manufacturing [32]. It is forecasted that 25 billion IoT devices will be in use by 2021 [4]. However, IoT electronics require energy, typically supplied by batteries. As the number of IoT devices grows to billions, the cost of replacing batteries can negate the economic and societal advantage of acquiring data from the devices [3]. This problem is exacerbated in applications integrating countless devices such as smart cities and smart agriculture [2]. Scavenging environmentally available energy sources such as light, mechanical vibration, and ambient RF is a competitive option to provide power for IoT devices [3], [32], [33], [64]. For passive sensing, mechanical vibration is one of the most promising candidates. Vibrations contain not only meaningful information, but also harvestable energy. Vibrations resulting from sources such as cars, machines, and humans have unique spectral signatures [33]. As such, identification of vibration sources can be achieved passively by matching sensor response to the spectrum of the source [43], [55], [56], [59], [65], [66]. An example scheme for using vibration as a wireless intruder detection system is shown in Figure 3.1. A car (intruder) is driven close to a battery-less vibration event detector and RF transmitter. The sensor passively harvests energy from the vibrations generated by the vehicle and utilizes this energy to transmit RF pulses. Battery-powered IoT devices in the vicinity can be set into sleep mode until these RF pulses are detected [42]. In this example, the IoT devices can turn on a camera and long-range radio communication to report intrusion. Near zero

power (≈ 10 nW) circuits for detecting RF pulses with high sensitivity (≈ -70 dBm) are shown by several research groups [47], [67]–[71].

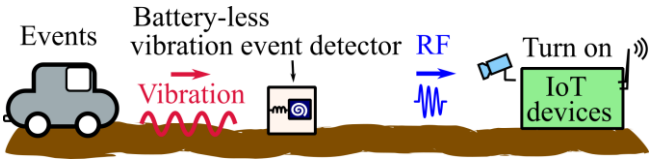

Figure 3.1: Operational scheme of the battery-less vibration event detector and RF transmitter is shown. The sensor node harvests energy from vibration and transmits RF pulses to wake up other battery powered IoT devices.

RFID tags are an example of battery-less wireless vibration detectors. A typical methodology has been developed in which a motion event changes the electrical impedance of an RFID antenna, modulating the backscattered signal to be picked up by a reader [41], [72]. Despite the zero-power requirement of the antennas themselves, RFIDs need a reader to continuously interrogate the RFID tags, so the system is constantly consuming power. Other architectures for battery-less vibration event detectors and RF transmitters that forgo active reading were also reported [73], [74]. These devices harvest energy from vibration and directly convert the energy into transmitted RF which is modulated by the DC output voltage from other sensors. Hence, this architecture still needs an external bias voltage from a battery.

A major challenge in harvesting vibrational energy is that most environmental sources such as generators, cars, and fans have low acceleration (< 1 g), and a low-frequency fundamental peak (< 150 Hz) [33], [75]. Traditional vibration energy harvester designs consist of piezoelectric or silicon springs and proof masses, which typically results in resonance frequencies much higher than this region of interest. In order to maximize energy generation, the resonance frequency of the cantilever should be tuned to match the source frequency [33], so reducing this resonance and broadening the resonance bandwidth is important for operation. Several techniques have been proposed to do this including multi-mode oscillators [76], multi-degree-of-freedom

(DOF) oscillators [77], and energy harvesters with stoppers [78], [79]. The energy harvester in this chapter combines techniques from [76]–[79] to efficiently collect energy from low-frequency sources. 3D printing allows for the creation of structures with low resonance frequencies due to the very low elastic moduli of the plastics used as the print material. This facilitates the creation of structures with low spring constants while also having the added benefit of being able to undertake large strains [80].

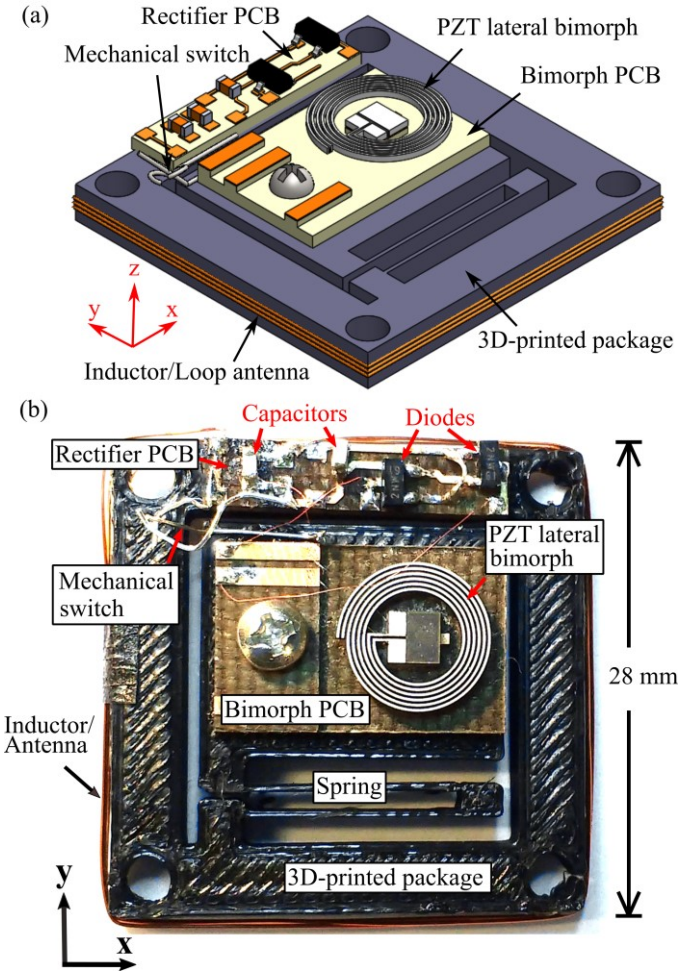

Figure 3.2: (a) Assembly of the battery-less vibration event detector and RF transmitter consisting of a PZT lateral bimorph and PCB mounted on top of a 3D-printed package with an integrated mechanical switch. (b) A photograph of the sensor. The transmitting antenna is formed by wrapping a coil around the fixed frame of the 3D-printed package.

3D printing is an additive manufacturing technique that creates 3D objects by joining materials under computer control. Compared with conventional manufacturing methods such as machining and injection molding, 3D printing enables faster turnaround time from designing to manufacturing and enables fabricating parts with complex geometry [80]. For energy harvesters, 3D printing is widely used for manufacturing supporting parts such as the casing and mounting [80], [81]. A few energy harvesters using 3D-printed parts in the spring-mass system are shown where the cantilever spring [82], a nonlinear spring [80], and a 3D coil spring [83] are 3D printed. In this chapter, 3D printing is used to make a package with a low resonance frequency spring-mass system to enable low frequency energy harvesting. The package can be rapidly redesigned for different resonance frequencies. 3D printing can be a prelude to implementing the plastic components using injection molding for lower cost devices [84].

This chapter reports a battery-less vibration event detector and RF transmitter. The detector integrates a mechanical energy harvester and an RF transmitter circuit (Figure 3.2). The 3D-printed spring-mass system responds to the external vibration, reaching high amplitudes at resonance frequencies. The 3D-printed package is integrated to enable low frequency (17-40 Hz) energy harvesting by frequency up-conversion through impact with stoppers [78], [79]. Upon sufficient amplitude of the 3D-printed stage, the vibration actuated switch impacts, triggering the impulse response of the PZT lateral bimorph. The bimorph can be considered both a multi-mode oscillator and a multi-degree-of-freedom (DOF) oscillator which can capture energy from all directions [76], [77]. The resonance frequencies of the PZT lateral bimorphs are in the 300 Hz range and generate voltages across rectifiers and a storage capacitor. The stage motion also shorts out the LC oscillator connected across the storage battery generating an RF pulse once sufficient amplitude is reached, serving the role of a mechanical

comparator. The event detector architecture is modular: the 3D-printed plastic package can be modified to tune to a desired frequency spectrum. For example, for a given mechanical energy spectrum, a 3D printer can quickly, generate a structure that can be integrated within the structure for optimized operation.

3.2 Design and Fabrication

The battery-less vibration event detector consists of a mechanical energy harvester and a RF transmitter circuit, both of which are explained in detail in Subsection 3.2.1 and 3.2.2, respectively. A 3D model and a photograph of the sensor are shown in Figure 3.2. The energy harvester part consists of a PZT lateral bimorph and a 3D-printed plastic package with mechanical stopper switches. The transmitter circuit consists of a rectifier, capacitors, switches, LC oscillator, and a loop antenna.

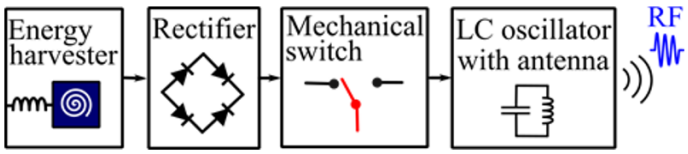

Figure 3.3: Block diagram of the battery-less vibration event detector and RF transmitter.

The operation block diagram is shown in Figure 3.3. The energy harvester converts energy from vibration into DC voltage stored in a capacitor. When vibrations are strong enough to close a mechanical switch, the switch connects the capacitor with an LC oscillator. The LC oscillator transmits RF pulses to the environment through a loop antenna.

From Figure 3.2, the PZT bimorph is mounted on top of the bimorph PCB, which is attached to a 3D-printed plastic proof mass. The 3D-printed plastic structure consists of a proof mass connected to a fixed frame through a serpentine spring providing substantial motion at low frequency. The rectifier PCB is attached to the plastic frame. It consists of a contact switch, a rectifier circuit, an LC oscillator, and a loop antenna.

The inductor of the LC oscillator is made from a magnet wire wrapped around the battery-less vibration event detector and functions as a loop antenna.

3.2.1 Energy Harvester and 3D Printed Package

The energy harvester is designed to capture energy from low-frequency vibrations in all directions. This is enabled by an impulse provided by the 3D-printed package as a stopper, along with several resonant modes of the spiral bimorph and the 3D-printed package. The energy harvester combines multiple techniques for broadband operation: multi-mode, multi-degree-of-freedom, and stoppers [76]–[79].

Table 3.1: Example of material properties for energy harvester [80].

Fabrication method	Material	Density (g/cm^3)	Modulus (GPa)	Normalized resonance frequency
3D printing	PLA	1.24	3.8	f_{PLA}
Microfabricating	Silicon	2.33	190	5.2 f_{PLA}
Machining	Steel	7.85	205	2.9 f_{PLA}

Materials for 3D printing such as polylactic acid (PLA) have lower Young's modulus than materials used in other common techniques such as microfabricated silicon and machined steel (Table 1.1) [80]. Using low Young's modulus materials in energy harvesters decreases the resonance frequency of a spring-mass system with the same geometry. For example, a simple energy harvester structure with a cantilever and a proof mass (Figure 3.4) has an in-plane bending mode resonance frequency of,

$$f = \frac{1}{2\pi}\sqrt{\frac{k}{m}} = \frac{1}{4\pi}\sqrt{\frac{w^3}{AL^3}}\sqrt{\frac{E}{\rho}} \tag{3.1}$$

where k is the cantilever spring constant, m is the mass of the proof mass, E is Young's modulus, h is cantilever height, w is cantilever width, ρ is density, and A is proof mass area. A resonance frequency ratio of spring mass systems with identical geometry, but

different material is shown in Table 1.1. From this table, using 3D-printed PLA decreases the resonance frequency compared to silicon by 5.2 times, and steel by 2.9 times.

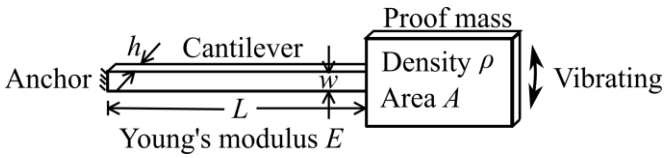

Figure 3.4: Dimension for cantilever and proof mass energy harvester.

The 3D-printed package used in this device is designed to have resonance modes at 13 Hz and 40 Hz, which are closely matched to the vibration frequencies of interest of our sample sources (electrical generators). The meander spring is designed to achieve low resonance frequency while keeping the device size small. Holes with a 2-mm diameter are included for mounting purposes. The proof mass is connected to a switch which acts as a mechanical stopper. The switch gap is closer than the gaps between the proof mass and outside edges, so the switches will collide before the proof mass hits the edges. This impact provides an impulse force to the PZT bimorph mounted on the proof mass.

The 3D-printed package plastic spring-mass system is fabricated by a MakerBot Replicator 2 Desktop 3D-printer with PLA filament with 3 mm thickness. The serpentine spring segments have dimensions of 15.5 mm × 0.3 mm and 2 mm × 2.5 mm. The proof mass has an area of 18 mm × 14 mm and a weight of 714.2 mg. The inertial frame has inner dimensions of 20 mm × 20 mm with a 4-mm width and weight of 1153.3 mg.

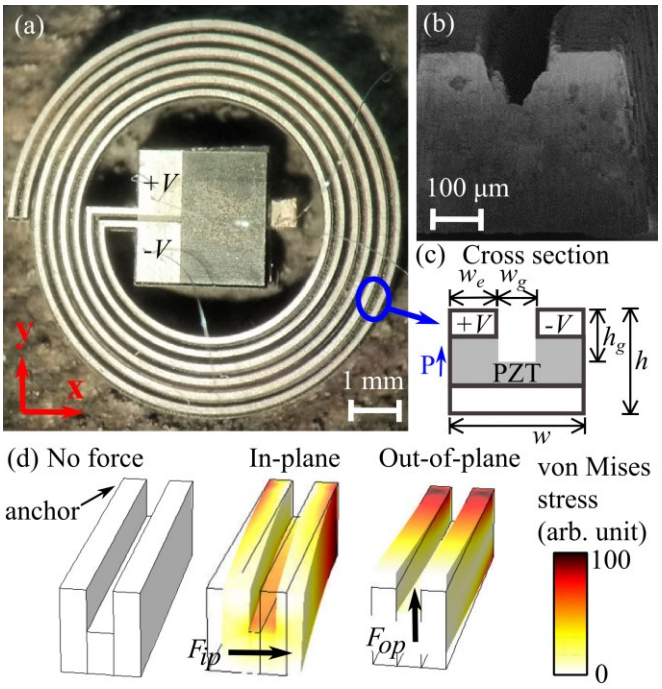

Figure 3.5: PZT lateral bimorph for 3-axis energy harvesting. (a) Photograph of the bimorph. (b) Scanning electron microscope photograph of bimorph cross section. (c) Cross section of the bimorph. Parameters are the following: PZT thickness h = 0.5 mm, beam width w_e = 0.15 mm, groove width w_g = 0.15 mm, groove height h_g = 0.25 mm. (d) 3D model showing straight bimorph with a groove without external force, bending bimorph in-plane by force F_{ip}, and bending out-of-plane by force F_{op}.

The PZT bimorph, shown in Figure 3.5a, is made of lead zirconate titanate (PZT) with dimensions 8.7 mm × 9.0 mm × 0.5 mm, 146.6 mg. The structure is adapted from a monolithic 2-axis in-plane PZT lateral bimorph energy harvester [85], [86]. An additional groove is cut into the bimorph, along the middle of the spiral bimorph to allow out-of-plane sensitivity for three-axis energy harvesting [44], [87]. Different stress in the top and bottom half of the PZT bimorph results in the output voltage when the bimorph is bended out-of-plane. A scanning electron microscope (SEM) photograph (Figure 3.5b) shows the micromachined groove cut, with the concept illustrated in Figure 3.5c. The bimorph has a floating electrode on the bottom side, and positive and negative output electrodes on the top side. The von Mises stress profiles during cantilever bending in-plane and out-of-plane are shown in Figure 3.5d. In-plane force

(F_{ip}) results in a different stress in the left and right parts of the bimorph, whereas the out-of-plane force (F_{op}) results in a different stress on the top and bottom. This stress is transduced to energy through the d_{31} and d_{33} piezoelectric coefficients. The bimorph is a spiral shape to lower the resonance frequency by increasing length but minimizing the lateral area of the device.

The PZT bimorph is fabricated by selective scanning of a LPFK Protolaser U on a 25.4 mm × 25.4 mm × 0.5 mm APC International 840 bulk lead zirconate titanate (PZT) plate with silver on top and bottom [60]. The laser micromachining process enables a simple, single step process for achieving feature sizes as small as 150 µm with a high aspect ratio (3.3:1). Precision actuators, and zero-power sensors can also be fabricated by this process [52], [53], [61], [88]. After fabrication, the bimorph is attached to the 11 mm × 17 mm × 1.5 mm, 400.0 mg PCB using conductive silver paint. The PCB, made of FR4, is etched by laser scanning to provide clearance for the released part of the bimorph. The electrodes of the bimorph are wire-bonded to the PCB.

3.2.2 Circuit and Transmitter

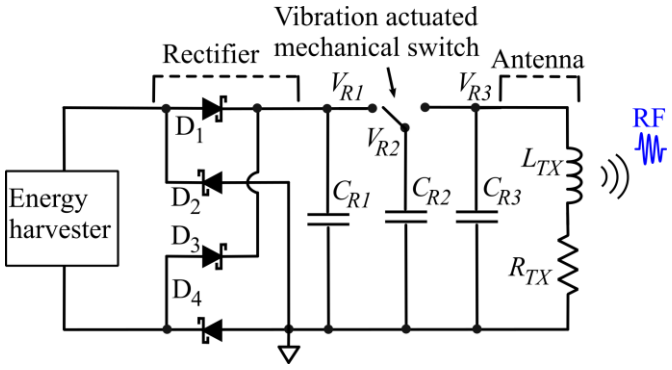

Figure 3.6: An electrical diagram of the battery-less vibration event detector consists of the PZT bimorph, rectifier, mechanically actuated switch, and transmitter circuit.

An equivalent circuit of the transmitter is shown in Figure 3.6, with the estimated and experimentally measured (using a HP 4194A impedance analyzer) parameter values listed in Table 3.2. The transmitter circuit consists of the energy harvesting bimorph,

bimorph PCB, and rectifier PCB which houses a rectifier circuit with a capacitor (C_{R1}), an LC oscillator consisting of capacitors (C_{R2}, C_{R3}) and an inductor/antenna. The bridge rectifier is made of four Nexperia BAT754 Schottky barrier diodes with a 0.2 V forward voltage (V_F). The low voltage drop across the diodes minimizes the diode-voltage drop energy loss in the rectifier. Fixed parts of the contact switch are soldered to the rectifier PCB. The PCB is attached to the fixed frame of the plastic package. The moving part of the contact switch is attached to the plastic proof mass with cyanoacrylate adhesive. The bimorph output and the moving part of the contact switch of the bimorph PCB are connected to the rectifier PCB using Whitmor MWRD46SPN magnet wire. This thin wire (40 μm copper diameter with 2.5-5 μm polyurethane nylon insulator) provides negligible mechanical loading to the moving proof mass. The inductor/antenna is made of 3 turns of AWG31 magnet wire wrapped around the 3D-printed plastic package frame and soldered to the rectifier PCB.

Table 3.2: Transmitter circuit parameters.

Parameter	*Estimated value*	*Measured value*
C_{R2}	147 pF	148.6 pF
C_{R3}	147 pF	154.2 pF
L_{TX}	960 nH	989.7 nH
R_{TX}	0.15 Ω	2.88 Ω

When vibrating with a small amplitude (Figure 3.7a), the piezoelectric bimorph generates an electrical charge that is rectified and stored onto a reservoir capacitor C_{R1}. The switch at node V_{R2} is connected to the moving plastic proof mass and toggles between the reservoir capacitor C_{R1} (node V_{R1}) and a transmitting LC oscillator (node V_{R3}). As the proof mass displacement exceeds the gap size (g_1), the contact switch node V_{R2} is connected to the node V_{R1} (Figure 3.7b) and collects charge from the reservoir

capacitor C_{R1}. As the proof mass continues to move, the switch will then close between nodes V_{R2} and V_{R3} (Figure 3.7c). This releases the collected charge into an LC oscillator for RF transmission. The energy stored on the capacitors triggers oscillations of the LC oscillator in the HF band (≈ 10-15 MHz) [89]. The LC oscillator transmits RF pulses that can be detected using a tuned radio. Since the contact switch only closes upon enough amplitude of motion equal to the switch gap, the gap can be adjusted so that the battery-less vibration event detector only transmits upon a set threshold of motion.

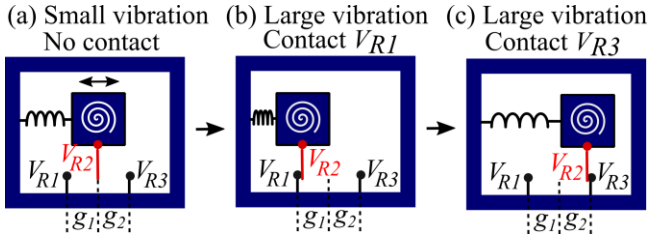

Figure 3.7: Battery-less vibration event detector operation (a) vibration energy harvester increases charge stored in C_{R1} (b) impact switch connects and transfers charge from C_{R1} to C_{R2} (c) impact switch connects and transfers charge from C_{R2} to LC oscillator and an antenna.

A loop antenna is designed specifically to match the resonance frequency of the LC oscillator transmission. The antenna has a 2.5 cm radius with 9 turns of AWG magnet wire. An equivalent circuit of the antenna is shown in Figure 3.8a, and a photograph is shown in Figure 3.8b. The equivalent circuit consists of the inductance of the antenna L_{RX}, a wire resistance R_{RX}, the parasitic capacitance of the oscilloscope probe and antenna C_P, and a damping resistor R_D. Table 3.3 lists the estimated and experimentally determined (using an HP 4194A impedance analyzer) parameter values for the equivalent receive circuit. A typical loop antenna of our design has a quality factor (Q) around 20 in order to have a reasonable gain and bandwidth [89], and so a damping resistor R_D is added in parallel as shown in Figure 3.8a to reduce the Q to this desired range.

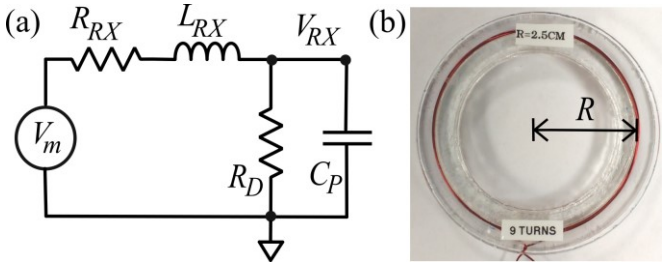

Figure 3.8: (a) The equivalent circuit model of the receiver (b) Photograph of the receiver antenna.

Table 3.3: Receiver circuit parameters.

Parameter	*Estimated value*	*Measured value*
C_P	15 pF	21 pF
R_D	22 kΩ	22 kΩ
L_{RX}	12.8 μH	8.8 μH
R_{RX}	0.23 Ω	0.1 Ω
F_{RX}	11.5 MHz	11.7 MHz
Q	24	9.1

3.3 Modeling and Analysis

The analysis is broken into mechanical and electrical parts. The mechanical analysis has two sections: First, the PZT bimorph is modeled to identify the resonance frequencies and open circuit voltage response to vibration. Second, the bimorph anchored on the plastic spring-mass resonator is investigated. The bimorph mass is much lower than the plastic package mass, so the coupling from the bimorph oscillation back to the plastic package is negligible.

The PZT bimorph resonance modes are investigated with COMSOL finite element simulation software. The backside of the electrode is anchored with a fixed boundary condition. A COMSOL eigenfrequency study estimates the resonance frequency of translation modes (x, y, z), and rotation modes (ω_{xy1}, ω_{xy2}, ω_z) as 775 Hz,

734 Hz, 245 Hz, 369 Hz, 398 Hz, and 425 Hz, respectively. The ω_{xy1} and ω_{xy2} modes refer to angular oscillation around different axes in the XY plane. These resonance mode shapes are shown in Figure 3.9.

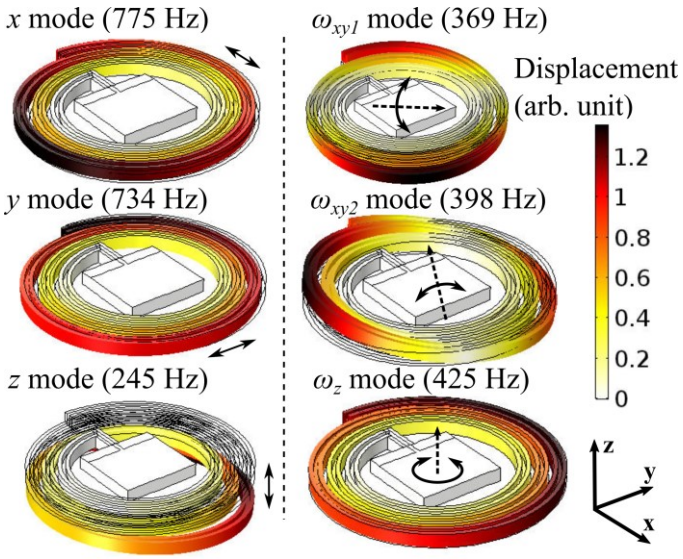

Figure 3.9: PZT bimorph mode shapes from COMSOL finite element eigenfrequency study that corresponds to the translation (x, y, z) and rotation (ω_{xy1}, ω_{xy2}, ω_z) modes. ω_{xy1} and ω_{xy2} modes refer to angular oscillation around different axes in the XY plane.

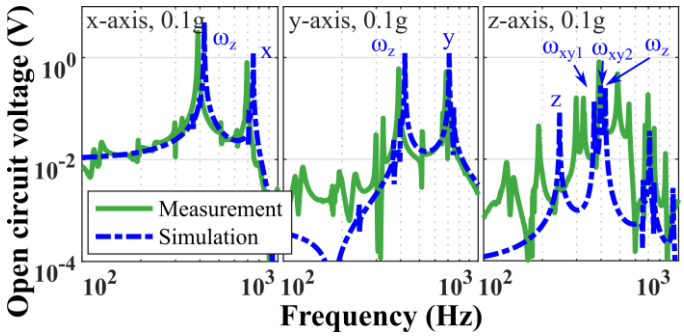

Figure 3.10: Comparison of simulation and measurement of the open circuit voltage of the PZT bimorph without the 3D-printed package. The bimorph is excited at 0.1 g by a shaker table along the x-, y-, and z-axes.

The open circuit voltage of the PZT bimorph is investigated with a COMSOL frequency domain analysis. The simulated result is compared with the measurement in Figure 3.10. The electrical load is set to 100 MΩ for each terminal. The mechanical damping is added as an isotropic loss factor $\eta = 2.9 \times 10^{-3}$. The frequency for *x*, *y*, and

ω_z matched with the FEA results with an error of 12%, 7%, and 9%, respectively and other modes are matched within 30% error. The variation in laser cutting profile and a misalignment in mounting angle can all contribute to the error found.

COMSOL eigenfrequency simulation loaded by the equivalent mass of the PZT bimorph, PCB, and mounting hardware estimates the three lowest resonance modes of the 3D-printed plastic package as 13.2 Hz, 40.7 Hz, and 13.8 Hz for x-, y-, and z- modes respectively. The mode shapes are shown in Figure 3.11. The low resonance frequency of the 3D-printed package allows the vibration event detector to harvest energy more effectively from low-frequency vibration sources.

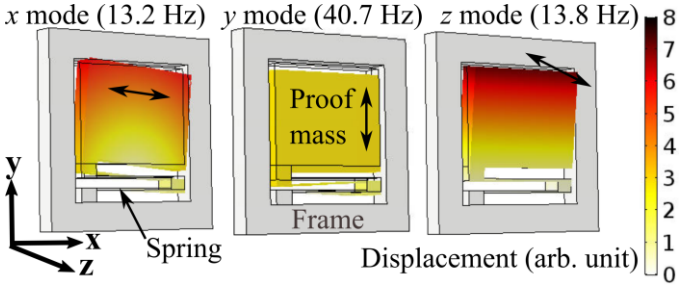

Figure 3.11: 3D-printed plastic package mode shapes from COMSOL finite element eigenfrequency study that correspond to measured vibration event detector output voltage peaks.

The charge from the bimorph is rectified and stored onto a reservoir capacitor C_{R1} (147 pF) which is charged until no more current flows through the rectifier diodes. The maximum reservoir voltage, $V_{R1,max}$ is

$$V_{R1,max} = V_{B,max} - V_F \tag{3.2}$$

where $V_{B,max}$ is the maximum open circuit voltage amplitude across of the bimorph ($V_B = V_+ - V_-$), and V_F is the forward bias voltage of the rectifier diodes. The voltage before switch closing is defined as

$$V_{R1,0} = V_{R1}(t = 0^-) \leq V_{R1,max} \tag{3.3}$$

Reservoir capacitance C_{R1} was chosen to be comparable with the measured output capacitance of the bimorph C_0 so that the reservoir capacitance is fully charged to the peak voltage of the bimorph after a few periods of bimorph oscillation.

When the vibration amplitude is large enough, the moving part of the contact switch, V_{R2}, touches either V_{R1} or V_{R3}. V_{R1} and V_{R3} act as mechanical stoppers to the movable part of the switch. These stoppers can be modeled as piecewise linear differential equations [89]. Frequency response for motion in one dimension can be obtained analytically in an implicit form [78], [79], [90]. When the switch, V_{R2}, contacts V_{R1}, the reservoir capacitor C_{R1} is connected to a second reservoir capacitor C_{R2}. The voltage in capacitor C_{R2}, determined by charge sharing between two parallel capacitors, is given by

$$V_{R2,0} = V_{R1,0}C_{R1}/(C_{R1} + C_{R2}) \tag{3.4}$$

As the proof mass continues to move, the contact switch then connects the capacitor C_{R2} to capacitor C_{R3}. The voltage in capacitor C_{R3}, as dictated by further charge sharing, is given by

$$V_{R3,0} = V_{R1,0}C_{R1}C_{R2}/[(C_{R1} + C_{R2})(C_{R2} + C_{R3})] \tag{3.5}$$

An LC oscillator is implemented by the capacitors and an inductor with an inductance L_{TX}, and its parasitic wire resistance R_{TX}. An antenna capacitor C_{R3} is added to prevent energy loss at the beginning of switch closure before a fully closed contact is made. Without capacitor C_{R3}, the antenna forms an LC oscillator with parasitic capacitance and the oscilloscope probe capacitance. This LC oscillator rings at a higher frequency and dissipates energy before the switch completely closes. The capacitors C_{R2} and C_{R3} are chosen to optimize energy transfer and target a frequency of $f_{TX} \approx 10$ MHz. The inductance of the square coil is given by

$$L_{TX} \approx 2\,\mu_0\mu_r N_{TX}^2 w[ln\,(w/a) - 0.774]/\pi \quad (3.6)$$

where N_{TX} is the number of turns, w is the width of the rectangle plastic package (28 mm), and a is wire radius (0.12 mm). After the switch closes, there are two possibilities. Case 1: the switch bounces back much faster than the LC oscillation period. In this case, the LC oscillation capacitance $C_{TX} = C_{R3}$. Case 2: the switch remains closed until the oscillation ends. In this case, $C_{TX} = C_{R2}+C_{R3}$. The experimental results have shown that the switch closing time is typically much longer than the LC ring-down time; therefore, the capacitance for the transmission LC oscillator is,

$$C_{TX} = C_{R2} + C_{R3} \quad (3.7)$$

Each cycle energy is stored in the capacitor before transmitting, so the energy extracted per cycle is

$$E_{TX} = \frac{1}{2}\,(\,C_{R2} + C_{R3})\,V_{R3,0}^2 \quad (3.8)$$

The voltage across an antenna V_{R3} (t) is

$$V_{R3,0}(t > 0) = V_{R3,0}\exp(-\gamma_{TX,0}t)\left(\cos(\omega_{TX,0}t) + \left(\frac{\gamma_{TX,0}}{\omega_{TX,0}}\right)\sin(\omega_{TX,0}t)\right) \quad (3.9)$$

where the oscillation angular frequency of the LC oscillator $\omega_{TX} = 2\pi f$ is,

$$\omega_{TX} = \sqrt{\frac{1}{L_{TX}C_{TX}} - \left(\frac{R_{TX}}{2L_{TX}}\right)^2} \quad (3.10)$$

the damping coefficient of the LC oscillator γ_{TX} is,

$$\gamma_{TX} = \frac{R_{TX}}{2L_{TX}} \quad (3.11)$$

and the current flow in the inductor/antenna I_A is

$$I_{TX}(t) = \frac{V_{R3,0}}{L_{TX}\omega_{TX,0}}(\exp -\gamma_{TX}t)\sin(\omega_{TX}t) \quad (3.12)$$

In the HF band of RFID, RF mainly transmits through near field magnetic field coupling [89]. The inductor which also functions as a loop antenna can be considered as an oscillating point magnetic dipole $m = N_{TX} A_{TX} I_{TX}(t)$, where A_{TX} is the area of the antenna.

3.4 Experimental Results

3.4.1 Energy Harvester Testing

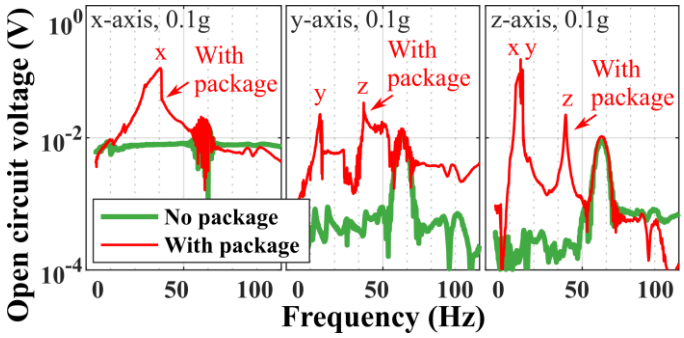

Figure 3.12: Open circuit voltage of PZT bimorph with and without 3D-printed package when excited at 0.1 g by a shaker table along the x-, y-, and z-axes.

The individual PZT bimorph without the plastic package is tested on a Vibration Research VR9500 single axis shaker table at 0.1 g in the x, y, and z directions. The bimorph is attached to a PCB which is screwed onto the shaker table. The open circuit voltage of the bimorph is buffered by a Texas Instruments TL082 JFET-Input operational amplifier with a 100 MΩ load resistor. The JFET-input stage also provides a low input capacitance of about 3 pF, including the parasitic capacitance. This is much smaller than output capacitance of the bimorph (148 pF), so voltage attenuation due to capacitive loading should be negligible. The open circuit voltage as a function of frequency is shown in Figure 3.12. The voltage peaks correspond to x, y, z, ω_{xy1}, ω_{xy2}, and ω_z are at 695, 685, 192, 299, 326, and 391 Hz, respectively. The bimorph impedance between electrode $+V$ and $-V$ is measured by an HP 4194A impedance analyzer. The resonance frequency for the mode ω_z was found to be 390 Hz. The measured impedance

is fitted to the Butterworth-Van Dyke model for the ω_z mode, and the extracted equivalent circuit parameters are C_0 = 148 pF, C_1 = 5.22 pF, R_1 = 451 kΩ, L_1 = 31.9 kH.

The PZT bimorph mounted on top of the 3D-printed plastic package is tested on the shaker table at 0.1 g as a function of frequency. At 0.1 g of acceleration, the plastic proof mass does not impact the surrounding frame nor does the contact switch close. The testing scheme is identical to individual PZT bimorph testing. The output voltage of the bimorph is shown in in Figure 3.12 when excited along the x-, y-, and z- axis. These plots show that the plastic package resonance increases the output voltage of the vibration event detector in the low-frequency region. In the x-direction, the increased output voltage has peaks at 19 Hz and 38 Hz. In the y-direction, the peaks are at 17 Hz and 40 Hz. In the z-direction, the peaks are at 18 Hz and 40 Hz. From COMSOL simulation, resonance frequencies for the x-, y-, and z- modes are 13.2 Hz, 40.7 Hz, and 13.8 Hz, respectively. Small mounting angle error may lead to excitation of modes in different directions. 3D-printed material properties are known to highly depend on the printing parameters and direction [91].

Next, the vibration is increased above the threshold needed to trigger the switch by an impact. The fully integrated vibration event detector is excited on the shaker table in the y-direction at 40 Hz, and the acceleration is swept from 0.05 g to 0.8 g. Figure 3.13 shows the spiral PZT bimorph open circuit voltage amplitude over the input acceleration range. In Figure 3.13a, the maximum amplitude reached is ≈ 10 V at an acceleration of 0.6 g. From (3.2), this vibration event detector should be able to charge the reservoir capacitor up to ≈ 10 V. Figure 3.13b shows an acceleration sweep before the proof mass starts impacting the fixed frame and closing the switches. The open circuit voltage was fitted to a linear function and the bimorph output was found to be only 71 mV/g before hitting the package at 0.17 g, which is the threshold acceleration. The threshold level is rapidly adjustable by changing the switch gap or 3D-printed

package dimension. At accelerations above the threshold, the output voltage increases to 11.1 V/g, 156 times greater than the voltage generated before impact. The impact generates sufficiently higher accelerations, triggering the impulse response of the harvester at its resonance frequencies at > 245 Hz.

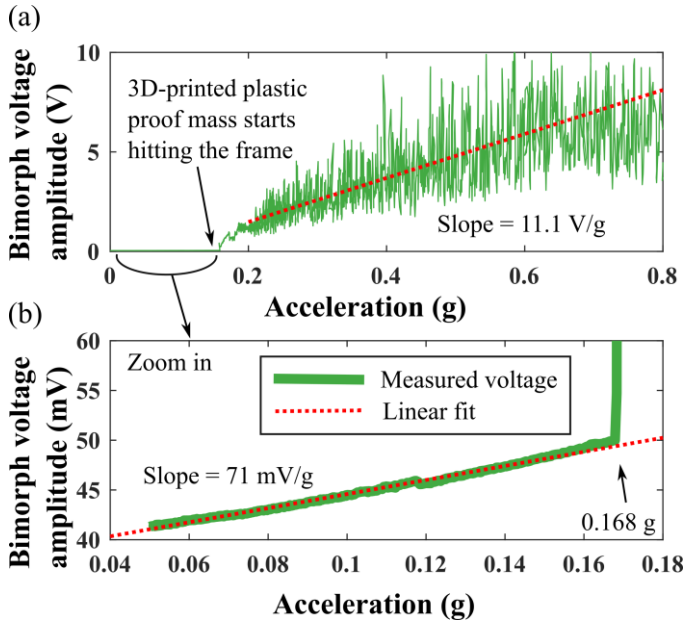

Figure 3.13: PZT bimorph voltage amplitude as a function of acceleration at 40 Hz along the y-axis. (a) acceleration sweep from 0.05 g to 0.8 g shows the output voltage with and without the induced impulse response of the PZT bimorph. (b) A zoomed in plot for accelerations before the impulse response of the PZT bimorph is induced.

At even higher applied accelerations, multiple impacts occur between the mass and the frame creating multiple switching events. The vibration event detector was vibrated along all three axes on the shaker table, sweeping the frequency at 0.75 g. The results are shown in Figure 3.14. Not only does the vibration event detector capture energy from low frequencies, but it exhibits a broadband response as well. This gives the potential to harvest energy from a variety of different sources as discussed previously.

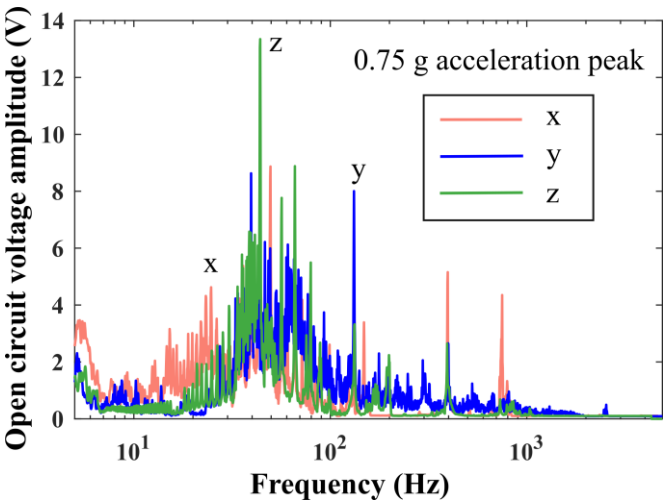

Figure 3.14: PZT bimorph open circuit voltage amplitude as a function of shaker table excitation frequency along x-, y-, and z-axis, when excited at 0.75 g.

3.4.2 RF Pulse Transmission Testing

The vibration event detector was excited on the shaker table in the y-direction at 40 Hz with an acceleration peak of 0.75 g. The frequency of 40 Hz was chosen as it corresponds to the frequency of output from the electrical generator that was to be detected using the sensor system. The transmitter voltages (V_{R2} and V_{R3}) are shown in Figure 3.15a. The reservoir capacitor's voltage V_{R2} starts from 5.1 V from past vibration excitation, but before the switch contacts for RF transmission. The received pulse is picked up by a loop antenna 5-meters away from the vibration event detector with a voltage shown in Figure 3.15b and an SNR of 22.8 dB. Figure 3.16 shows the period where the switch begins to close. For the first 6.5 ns, the switch is not fully closed and the voltage of the reservoir and antenna capacitors (V_{R2}, and V_{R3}) start to oscillate independently. Around 100 ns, the switch is fully closed, and the two capacitors maintain the same voltage. C_{R2}, C_{R3}, and L_{TX} form an LC oscillator with $V_{R2} \approx V_{R3}$. From experiment, if capacitor C_{R3} is removed, the antenna forms an LC oscillator with parasitic capacitance. This LC oscillator rings at a much higher frequency and dissipates energy before the switch completely closes. Figure 3.16 also confirmed that the switch

stays closed much longer than the oscillation time, so the total capacitance is $C_{TX} = C_{R2} + C_{R3}$ as in (3.7). From (3.8), energy extracted per cycle from piezoelectric energy harvester to the LC oscillator is $E_{TX} = \frac{1}{2}\,(C_{R2} + C_{R3})\,V_{R3,0}^2 = 0.95$ nJ. Voltage across reservoir capacitor (V_{R2}) and antenna (V_{R3}) predicted by (3.9) are compared with experimental data as shown in Figure 3.17. Parameters $f_{TX} = \omega_{TX}/(2\pi)$ and γ_{TX} predicted by (3.10) and (3.11) are compared with parameters that are extracted by a least square fitting and shown in Table 3.4. The frequency of the transmitted pulse is 10.9 MHz while the calculated frequency from (3.10) and measured component value in Table 3.2 is 9.2 MHz. This discrepancy may be due to overestimation of capacitance and inductance caused by parasitic capacitance and inductance when components were measured using an HP 4194A impedance analyzer.

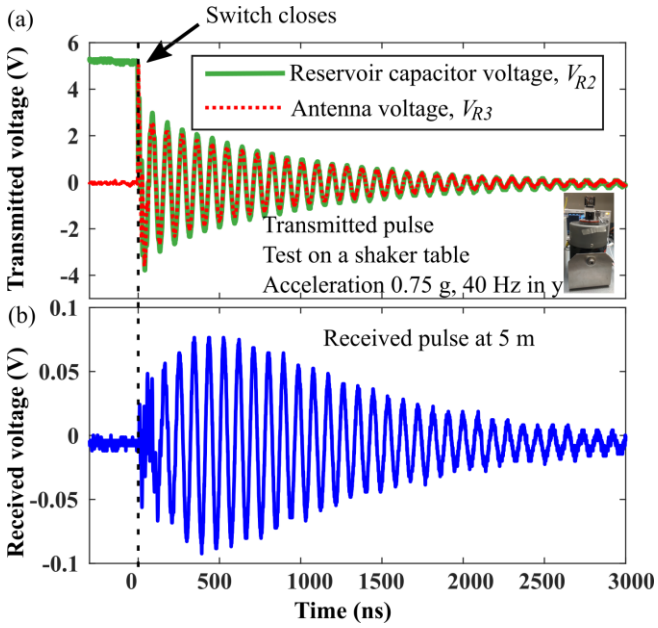

Figure 3.15: (a) Transmitted pulse of the vibration event detector excited at 40 Hz and 0.75 g in the y-direction by a shaker table. (b) Received pulse from transmission.

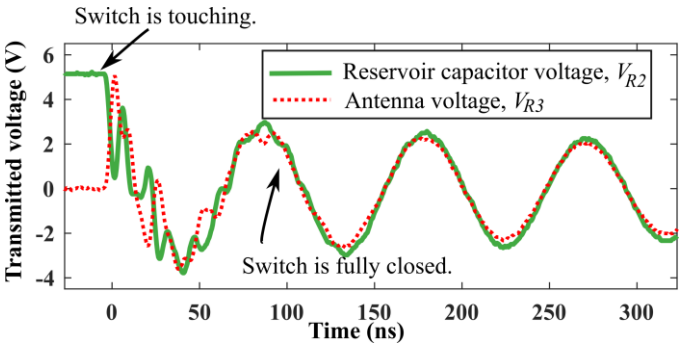

Figure 3.16: Plot of the beginning of the transmitted voltage vs. time showing that the switch is not fully closed until around 100 ns and stays closed much longer than the oscillation time. C_{R3} is necessary to decrease the frequency of the ringing caused by the LC oscillator formed by the parasitic capacitance and antenna inductance. Without this capacitor, significant energy would be dissipated before the switch completely closes.

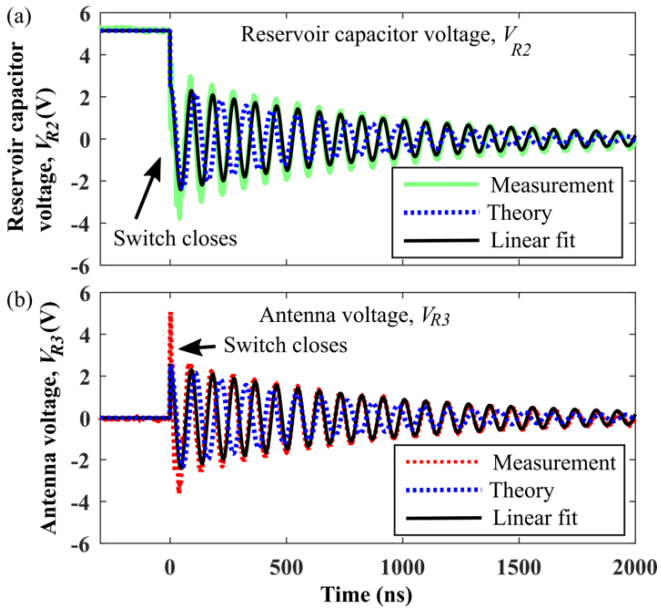

Figure 3.17: Comparison between measurement and theory with measured parameter and fitted parameter (a) Reservoir capacitor voltage V_{R2} (excited at 40 Hz and 0.75 g in the y-direction by a shaker table) (b) Antenna voltage V_{R3}.

Table 3.4: Parameter for voltage across transmission antenna

Value	Description	Calculated	Measured	Error
$f_{TX,0}$	Damped resonance frequency	9.2 MHz	10.9 MHz	15.9 %
$\gamma_{TX,0}$	Attenuation	1.5 MHz	1.1 MHz	-27.4%
Q	Qualify factor	19.9	30.1	33.9%

3.4.3 *Field Testing*

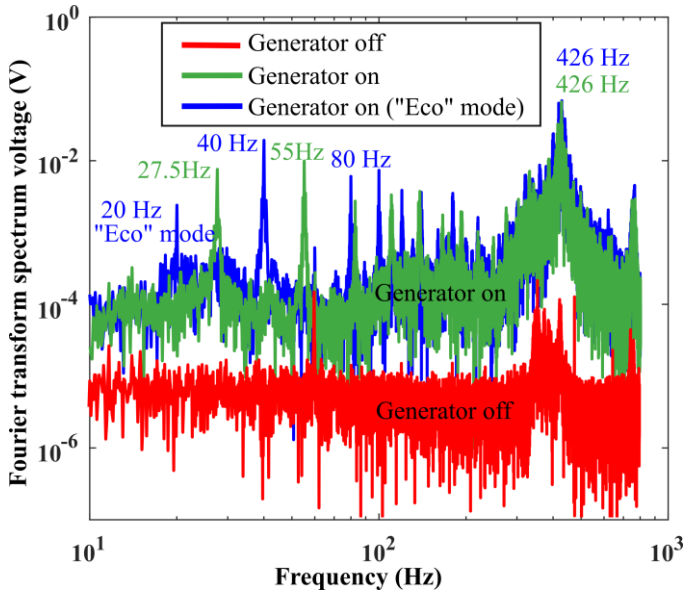

Figure 3.18: Spectrum of the voltage output of the PZT bimorph when mounted on an electric generator. Different motion signatures are shown when the generator is off, on, and on with eco mode.

The vibration event detector is mounted by tape with the y-direction pointing upwards, and x and z axis in-plane, on the top side of a Honda EU6500is portable gasoline electric generator. A receive antenna is placed 1-meter away. Figure 3.18 shows the bimorph capturing different motion signatures when the generator is off, on with high power mode, and on with “eco” mode. Eco and high power mode correspond to two different generator motor rotation rates of 2400 and 3600 RPM, resulting in vibration frequencies of 40 and 60 Hz as shown in Figure 3.18 [92].

The bimorph can be used as a zero-power sensor to classify the operation modes of the generator. Figure 3.19 shows transmitted and received pulses once the sensor detects motion from the generator. When the generator was turned on, the vibration event detector transmitted RF to the receive antenna placed 1 meter away with an SNR of 6.6 dB. The transmitted and received pulses have a lower voltage than the pulses from the sensor mounted on the shaker table because the generator does not vibrate with

a pure sinusoidal acceleration at the sensor resonance frequency. Therefore, the voltage induced in the bimorph is less than the voltage generated from the sensor on the shaker table.

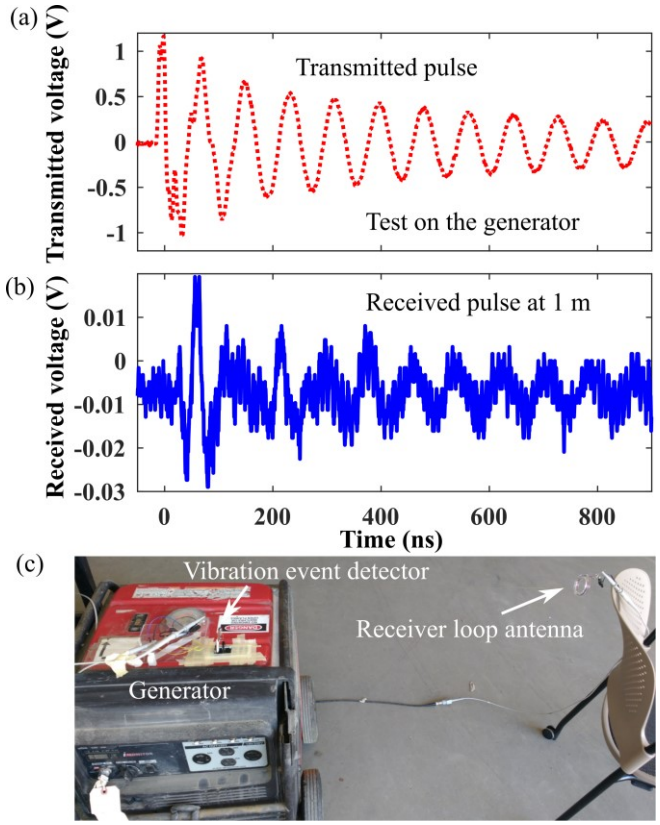

Figure 3.19: (a) Transmitted pulse of the vibration event detector mounted on top of an electric generator (Honda EU6500is) with eco and high-power modes corresponding to two different motor rotation rates of 2400 RPM and 3600 RPM, resulting in vibration frequencies of 40 and 60 Hz. (b) Received pulse from a loop antenna 1 meter away. (c) Photograph of the field test setup.

3.5 Conclusion

This chapter describes a battery-less vibration event detector that sends an RF pulse corresponding to the onset of a motion event once a threshold of motion is reached. The vibration event detector uses a novel design that integrates a multi-axis PZT bimorph, 3D-printed plastic package, mechanically actuated contact switch, and passive LC oscillator transmitter. The energy harvester unique PZT bimorph results in

significant sensitivity in all three axes of vibration excitation and by leveraging the low Young's modulus of plastics compared to PZT, the low-frequency sensitivity of the piezoelectric bimorph is enhanced. Furthermore, the contact switch significantly amplifies the output signal enabling successful detection of RF sent by a completely integrated transmitter.

The system is specifically designed for a portable gasoline generate showing operation and detection of 10.9 MHz RF output for a variety of operational modes. Due to the modular nature of the system, most parameters such as the low-frequency mechanical resonance, and the RF output frequency are easily altered for application in a variety of scenarios.

In the future, multiple RF transmitters at different frequencies could be used for each axis of the vibration event detector to determine the direction of the excitation vibration. In order to improve reliability, the switch itself can be manufactured with a greater repeatability of gap using better 3D printer capabilities, or replaced with a MEMS switch, where the gap is defined using lithography.

This device is applicable to a variety of IoT applications such as detecting cars for smart cities or monitoring for intruder motion. The ability to differentiate between sources with unique vibration spectra is an added benefit for applications where classification is necessary. Beyond this, the battery-less and totally integrated nature of the device make it ideal for sensing situations where a large number of widely distributed sensor are desired, like in environmental sensing of rain or wind induced vibration signals.

CHAPTER 4

PIEZOELECTRIC AND MAGNETIC MEMS IMU CALIBRATION STAGE FOR INERTIAL NAVIGATION

4.1 Introduction

The recent growth of interest in deployment of autonomous IoT platforms such as robots, unmanned aerial vehicles (UAVs) and self-driving cars has significantly increased the demand for reliable navigation technologies [93]–[95]. Although the Global Positioning System (GPS) is widely used for navigation, there exist numerous circumstances under which GPS technology cannot be relied upon [96], [97]. This is because GPS navigation devices calculate their positions based on external GPS radio signals transmitted from satellites [34]. Therefore, accurate navigation cannot be achieved when GPS signals are not available due to operation in indoor, underwater or underground environments, or due to deliberate jamming by military adversaries [96], [97].

An alternative technique that may be preferable under these circumstances is inertial navigation. In contrast to GPS, inertial navigation does not require the use of an external signal, as the technique utilizes internal measurements of accelerations and rotation rates by on-vehicle sensors [34]. Therefore, inertial navigation can be used for indoor navigation, underwater-underground navigation, and can be combined with GPS information by a Kalman filter to increase the position accuracy [98]–[101].

While inertial navigation has the advantage of not requiring an external signal, as is required by GPS, the position accuracy is critically dependent on the accuracy of the inertial sensor [102]. In particular, gyroscope scale factor error and bias fluctuation cause position error that grows as t^3, where t is the navigation time [34]. Gyroscope scale factor error refers to the ratio of the gyroscope output error versus the real rotation rate while bias error is the offset that exists between the gyroscope output and the real

rotation rate. Most inertial navigation systems use expensive tactical and navigation grade gyroscopes with low scale factor and bias error (examples in Table 4.1) [34], [102]–[105]. However, this low error comes at a cost – due to market forces and the cost of implementing advanced control loops and reducing fabrication errors, these gyroscopes are expensive, large, heavy, and consume power much greater than afforded by portable applications [34].

Table 4.1: Examples of tactical and navigation grade IMUs and their specifications.

Part number		ADIS16497-3BMLZ [103]	HG4930CA51 [104]	HG9900 [105]
Manufacturer		Analog Devices	Honeywell	Honeywell
Size (mm^3)		47x44x14	65x51x35.5	152x152x152
Power (mW)		294	2000	10,000
Cost ($/each) - Digikey 1 unit [106]		$2,610	$9,999	≈ $100,000 [107]
Accelerometer	Velocity random walk (m/s/√Hr)	0.04	0.09	N/A
	Scale factor error (ppm)	100	600	100
	Bias repeatability (mg)	6	5	0.025
	Cross axis sensitivity (%)	0.4	0.35	N/A
Gyroscope	Angle random walk (deg/√Hr)	0.18	0.09	0.002
	Scale factor error (ppm)	2,000	600	5
	Bias repeatability (deg/hr)	252	20	0.0035
	Cross axis sensitivity (%)	0.4	0.35	N/A

Note: N/A indicates that the specification is not available.

Table 4.2: Examples of consumer grade IMU and their specifications.

Part number		ICM-42605 [114]	LSM6DSOX [112]	BMI160 [113]
Manufacturer		TDK InvenSense	ST-Microelectronics	Bosch sensortec
Size (mm^3)		2.5 x 3 x 0.91	2.5 x 3 x 0.83	2.5 x 3 x 0.83
Power (mW)		1.2	0.99	2.78
Cost ($/each) (Digikey, 5000-unit reel) [106]		$2.00	$2.30	$1.94
Accelerometer	White noise (μg/√Hz)	70	70	180
	Scale factor error (ppm)	5,000	10,000	10,000
	Bias repeatability (mg)	20	20	25
	Bias fluctuation (mg/ºC)	0.15	0.01	1
	Cross axis sensitivity (%)	1	N/A	1
Gyroscope	White noise (º/s/√Hz)	0.0038	0.0038	0.007
	Scale factor error (ppm)	5,000	10,000	10,000
	Bias repeatability (º/hr)	1,800	3,600	10,800
	Bias fluctuation ((º/hr)/ºC)	72	25	10,800
	Cross axis sensitivity (%)	1	N/A	2

Note: N/A indicates that the specification is not provided.

In contrast to the thousands of dollars one might expect to pay for a tactical or navigation grade IMU, consumer grade IMUs are much affordable, with prices on the order of a few dollars per IMU chip. One of the most popular IMU (inertial measurement unit) topologies used in consumer grade applications today is the 6-axis microelectromechanical systems (MEMS) IMU [108]. The 6-axis MEMS IMU consists of a 3-axis accelerometer, and a 3-axis gyroscope integrated on a single silicon substrate through the intimate integration of CMOS circuits and MEMS sensors [109]. This technology enables MEMS IMUs to be small, have low power consumption, and most importantly, be available at low cost with acceptable bias and scale factor performance for consumer products [110]–[114]. Examples of consumer grade IMU costs and specifications are shown in Table 4.2. While these consumer grade IMUs are used in

products such as smartphones and game consoles, they cannot be used for inertial navigation due to their high scale factor errors and high bias errors [34]. It is therefore desirable to find a way to mitigate these effects such that one may utilize these low-cost gyroscopes for navigation grade applications, greatly reducing the cost of navigation grade gyroscopes.

One way to overcome the effects of these undesired properties of scale factor drift and bias fluctuation that consumer grade MEMS IMUs exhibit is by using an integrated precise self-calibration system. Available methods for self-calibration include: 1) direct electronic rate injection [115]–[119], 2) sensor fusion [120]–[126], and 3) integrated high precision motion dither stage [127]–[135]. In direct electronic rate injection, a self-test electrical signal is applied to directly actuate the sensor proof mass by an electrostatic or piezoelectric force [117]. This force simulates the inertial force and Coriolis force stemming from the acceleration and rotation of the proof mass. However, the inability of the simulated force to fully mimic real mechanical motion limits the accuracy of the calibration. In sensor fusion, application specific calibration algorithms work based on output obtained from devices such as cameras [124], GPS units [125], barometric pressure sensors [126], and accelerometers measuring Earth's gravity [121]. The disadvantage is that incorporation of measurements from external sensors at high accuracies under varying conditions and locations is challenging. Applying known external mechanical stimuli can be accomplished accurately by typical bulky rate tables, but the rate table is prohibitively large and consumes much higher power than the gyroscope itself [136].

The third method is integration of a miniature high precision dither stage to calibrate out scale factor drift and bias fluctuation. In this method, a precision stage known as a dither stage applies known motion to calibrate the gyroscope and track scale factor drift in the field (*in situ*) or while using (in-run) [13], [61], [62], [88], [137]. The

advantage of using a precision dither stage for calibration over the other calibration methods discussed earlier is that the dither stage does not require information from other sensors and preserves the small form-factor of a 6-axis MEMS IMU. A detailed of comparison of calibration with a dither stage versus other calibration methods is shown in Table 4.3. As can be seen, the use of a precision miniature dither stage results in the highest possible improvement in scale factor error without the use of a bulky rate table.

Table 4.3: Examples of gyroscope calibration techniques.

Technique	Details	Gyroscope scale factor error (ppm)		Gyroscope bias fluctuation (deg/hr)	
		Before	After	Before	After
Rate table	Traditional rate table [136]	N/A	0.05	N/A	$7.3x10^{-4}$
Electronic rate injection	Axisymmetric bulk acoustic gyroscope [118], [119]	9,300	62	243,000	5,400
	Force-feedback with quadrature cancellation [120]	N/A	N/A	N/A	360
Sensor fusion	Sensor fusion fiber optic gyroscope with LiDar [138]	40,000	30,000	159,000	120,000
Precision miniature dither stage	PZT bonding on silicon dither stage [127]–[129], [139]	40,000	286	N/A	N/A
	Bulk PZT dither stage (This work)	**55,556**	**50**	**12**	**N/A**

Note: N/A indicates that the specification is not available.

In this chapter, a novel gyroscope calibration dither stage with 3-axis angular dither and in-plane (x-, y-) linear dither capability is presented [62], [88]. The dither stage provides precise measurements of the instantaneous scale factor to within 50 ppm [13], [137]. This error is comparable with tactical and navigation grade gyroscopes and better than existing errors on the scale of 50,000 PPM [13], [137]. The use of the calibration stage would therefore allow for long-term monitoring of sensor biases and may enable navigation with the 6 DOF IMU chips [13], [61], [62], [88], [137].

The dither stage discussed in this chapter comprises of two parts: 1) a monolithic bulk piezoelectric stage for in-plane dithering, capable of calibrating 1-axis gyroscopes [60], and 2) a magnetic actuator for out-of-plane dithering, capable of calibrating additional 2-axis gyroscopes [62]. Although having a piezoelectric actuation dither stage for 3-axis gyroscope calibration is preferred, the applied motion in the z-axis is coupled strongly to the in-plane motion, producing a significant dither stage induced cross-axis actuation of the gyroscope. In order to achieve a practical actuation and sensing platform for in-situ calibration of a gyroscope, 3-axis scale factor calibration is required where each axis is minimally cross-coupled. Therefore, a physically different actuation mechanism – magnetic actuation – is used for the third axis to potentially decouple the in-plane and out-of-plane actuation of the dither stage. It can be noted that for a full IMU, the accelerometer should also be calibrated; however, a gyroscope calibration dither stage is the focus of this work because position error from gyroscope scale factor drift and bias fluctuation is more critical for inertial navigation than the error contribution from accelerometers [34].

In the following sections of this chapter (4.2), the dither stage will be discussed in further detail, starting with an introduction to the micromachined piezoelectric dither stage structure used for in-plane dithering in 4.2.1, and the associated electronic control system in 4.2.2, and the out-of-plane magnetic dithering mechanism in 4.2.3. Next, in 4.2.4, the derivation of the applied angular rate is presented – this is an important metric that can be used to quantify the performance of a fabricated dither stage as the angular rate is the rotation rate applied by the stage to calibrate and correct for gyroscope scale factor error. This scale factor error and other error sources for the IMU to be calibrated by the stage are presented in 4.2.5, followed by a discussion of the thermal noise error contribution in 4.2.6. Experimental results of the fabricated stage will be presented in section 4.3.

4.2 Materials and Methods

Miniature motion stages for gyroscope calibration must provide precise rotation rates without adding significant noise to the gyroscopes. Stages that rotate continuously, such as motorized platforms, are preferred because the stages apply constant rotation rate to the gyroscope. However, power and signal routing to the gyroscope through structures such as slip rings is challenging to implement at a small scale [140]. Instead, a dither stage oscillating at a small angle can be used for gyroscope calibration [61], [130]. Gyroscope signal and power can be routed through to wire bonds that can bend without any impact on gyroscope performance, when the stage oscillates. The dither stage should be small and consume low power to be competitive in the market for consumer applications.

A dither stage for single axis gyroscope calibration is designed on laser-micro machined lead zirconation titanate (PZT), as explained in 4.2.1. A printed circuit board (PCB) is designed and assembled for controlling the dither stage and the gyroscope, as described in 4.2.2. Magnetic actuation is added for out-of-plane motion to realize 3-axis gyroscope calibration, as described in 4.2.3. The angular rate achieved by the combination of these different actuation mechanisms is analyzed in 4.2.4. As mentioned earlier, the angular rate is equivalent to the rotation rate that is applied to the gyroscope that is being calibrated, and is therefore an important metric in determining how much error reduction can be achieved by a calibration stage. An error model for 6-axis inertial measurement unit (IMU), including 3-axis gyroscope and 3-axis accelerometer is described in 4.2.5. From this model, a formula for correcting bias and scale factor errors after the gyroscope calibration is derived. Mechanical Brownian motion of the stage is derived and quantified in 4.2.6 to ensure that the Brownian motion adds negligible noise to the gyroscope.

4.2.1 Dither stage for gyroscope calibration

The calibration system consists of a monolithic, planar, laser-micro machined dither stage actuated by four coil PZT lateral bimorphs, as shown in Figure 4.1a [60], [61], [141]. The cross section of the bimorph structure with two electrodes on the top and one electrode at the bottom is shown in Figure 4.1b. Each bimorph can be actuated in different directions by controlling voltages on the top electrodes while grounding the bottom electrode, as shown in Figure 4.1c for the case of in-plane bending. Undesired out-of-plane motion is suppressed by a spring connecting between the coil and the dither stage, as shown in Figure 4.1d.

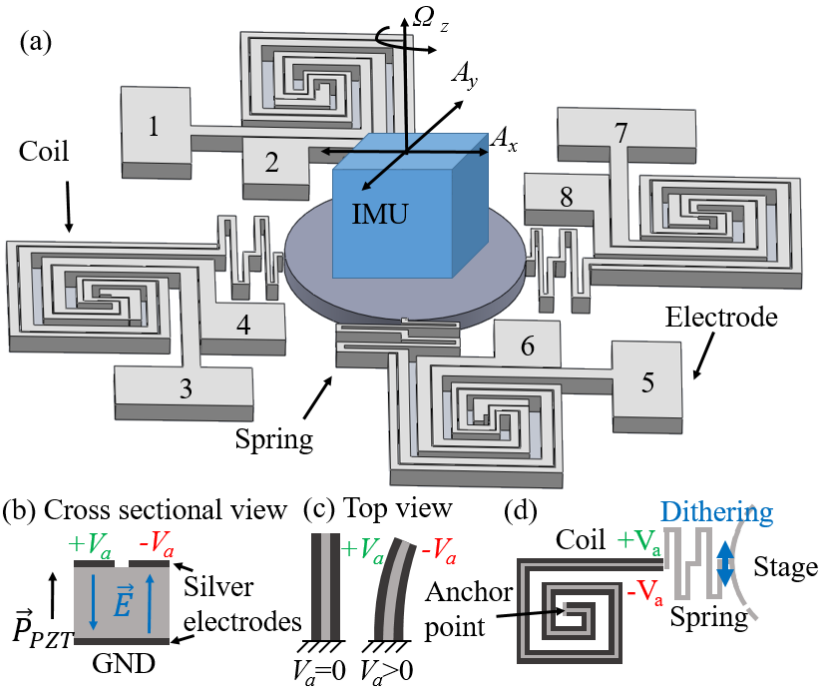

Figure 4.1: (a) 3D illustration of the dither stage with 8 electrodes for mechanical stimulate IMU in 3 modes (A_x, A_y, Ω_z) (b) Cross section of the PZT bimorph consisting of a ground electrode and separated top electrodes (c) Top view of the PZT lateral bimorph (d) A coil lateral bimorph and a spring actuates the dither stage.

The dither stage is designed to dither in 3 modes - A_x, A_y and Ω_z, as illustrated in Figure 4.1a. 1) A_x mode dithering refers to dithering to generate acceleration in the x-

direction for calibrating x-axis accelerometers. 2) A_y mode dithering refers to dithering to generate acceleration in the y-direction for calibrating y-axis accelerometers. 3) Ω_z mode dithering refers to dithering to generate angular rate around the z-direction for calibrating z-axis gyroscopes. The dither mode applied by the stage is determined by the polarity of the applied voltage to the 8 different electrodes of the stage, as shown in Figure 4.2, and summarized in Table 2.1. The angular dither speed and acceleration can be controlled by varying the frequency or amplitude of the sine wave excitation to the dither stage, as explained in 4.2.4.

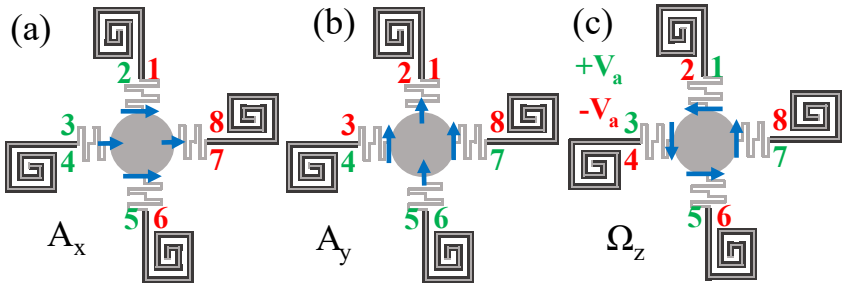

Figure 4.2: Electrode voltage combination for 3 dither stage modes (a) A_x, (b) A_y, (c) Ω_z.

Table 4.4: Electrode voltage combination for 3 dither stage modes (A_x, A_y, Ω_z), for which actuator voltage is $V_a = V_0 \sin(\omega t)$.

	Electrode							
Mode	**1**	**2**	**3**	**4**	**5**	**6**	**7**	**8**
A_x	$-V_a$	V_a	V_a	V_a	V_a	$-V_a$	$-V_a$	$-V_a$
A_y	$-V_a$	$-V_a$	$-V_a$	V_a	V_a	V_a	V_a	$-V_a$
Ω_z	V_a	$-V_a$	V_a	$-V_a$	V_a	$-V_a$	V_a	$-V_a$

4.2.2 PCB for dither stage control and gyroscope calibration

A prototype printed circuit board (PCB) (Figure 4.3) system was fabricated and assembled for testing the gyroscope calibration capability of the dither stage. While in this work, the system was built on a PCB using commercial off-the-shelf (COTS)

components, the system can conceivably be miniaturized using a high voltage CMOS process. A 6 degree-of-freedom IMU (Maxim Integrated MAX21105) is mounted upside down and wire bonded to the dither stage board, as shown in Figure 4.3a. The dither stage board is coated with a silver finish so that the surface can be wire bonded by an aluminum ultrasonic wedge wire bonder (Westbond 7400A). The block diagram of the system is shown in Figure 4.3b. The system comprises of a microcontroller, voltage amplifiers, and relays for interfacing with the computer, controlling the stage, and reading outputs from the gyroscope. The dither stage board is mounted on the control circuit board with pin headers, as shown in Figure 4.3c. The dither stage board is separated from the control board so that the dither stage board can be swapped out to evaluate various designs.

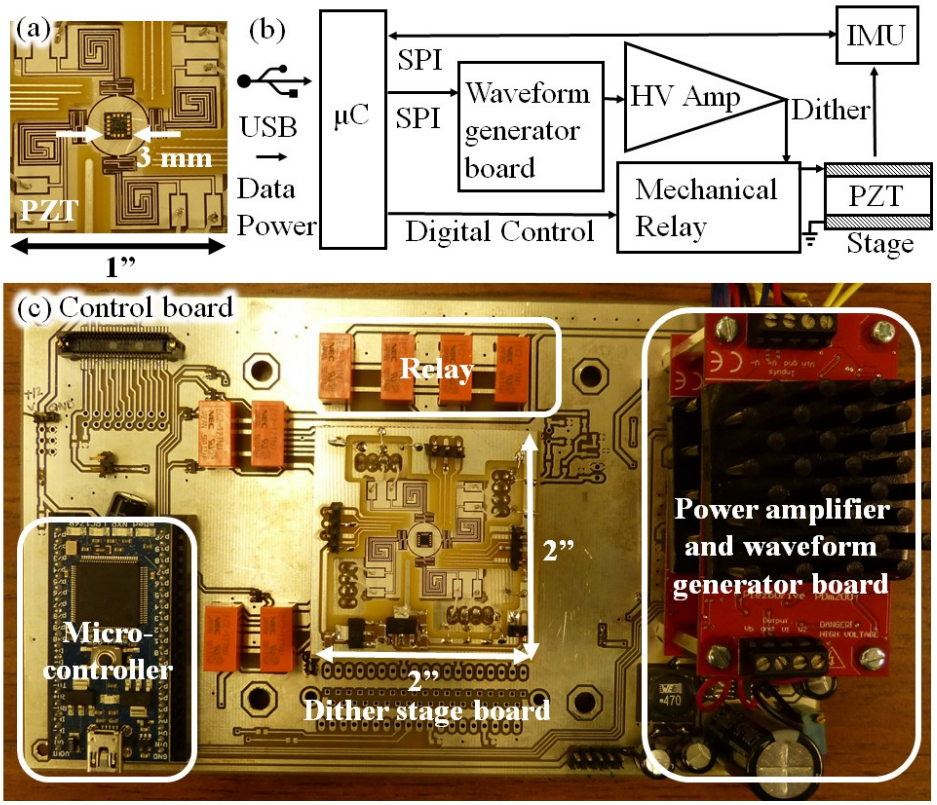

Figure 4.3: (a) 6-DOF IMU (MAX21105) mounted upside down on dither stage (b) A block diagram of the IMU testing (c) A photograph of the control PCB used for calibrating the IMU.

The control board consists of a waveform generator board, voltage amplifiers, mechanical relays, and a microcontroller. In the waveform generator board, an AD9833 waveform generator, timed by a CTS636 reference clock, is used to generate a 0.6 Vpp sine wave with 0.3 V_{DC} offset by direct digital synthesis (DDS). A LC low pass filter is used to remove high frequency quantization noise. Series LM833 amplifier amplifiers are used to create two output voltages with the opposite polarity $V(t) = \pm 5V \sin(\omega t)$. Alternatively, the waveform can be generated by an external function generator to achieve greater accuracy. Two PDM200 high performance piezo drivers amplify voltage to $V(t) = \pm 100V \sin(\omega t)$. The dither stage electrodes connect to Kemet EC2 miniature dual coiled, latched signal relays to control polarity. An MBED NXP LPC1768 microcontroller controls waveform generators and mechanical relays as it acquires 6-axis data with on-chip temperature from the IMU via SPI communication. MATLAB software controls and records data from the board via a generic USB connection to a computer. The board, which has dimensions of 7.4" x 4.4", was designed to be powered by either a single 5 V or 12 V power source, such as from USB or batteries, in order to be portable and easy to test on a rate table. The control board layout, schematics, and components are detailed in Appendix A.

4.2.3 Magnetic actuation for out-of-plane motion

The dither stage is actuated by piezoelectric actuation to calibrate a single-axis gyroscope (Ω_z mode) and 2-axis accelerometers (A_x and A_y modes), as explained in 4.2.1. Magnetic actuation is integrated to the dither stage to enable out-of-plane mode (Ω_x and Ω_y modes) for 3-axis gyroscope calibration. The device is shown in Figure 4.4 and consists of the piezoelectric dither stage integrated with 4 magnets actuated by 4 solenoids. A 3-axis gyroscope calibration dither stage with 3-axis piezoelectric actuation can be designed by adding grooves into the actuators, or other methods [87]. However, the out-of-plane modes (Ω_x and Ω_y modes) are strongly coupled with the in-

plane mode (Ω_z mode), causing the gyroscope to produce signals corrupted in the axis being calibrated due to cross-axis sensitivity to motion in the other axes excited by the dither stage. Ω_z mode is excited by lateral bimorph actuators and magnetic actuators are used for Ω_x and Ω_y. The two physical methods reduce the effect of cross-axis sensitivities.

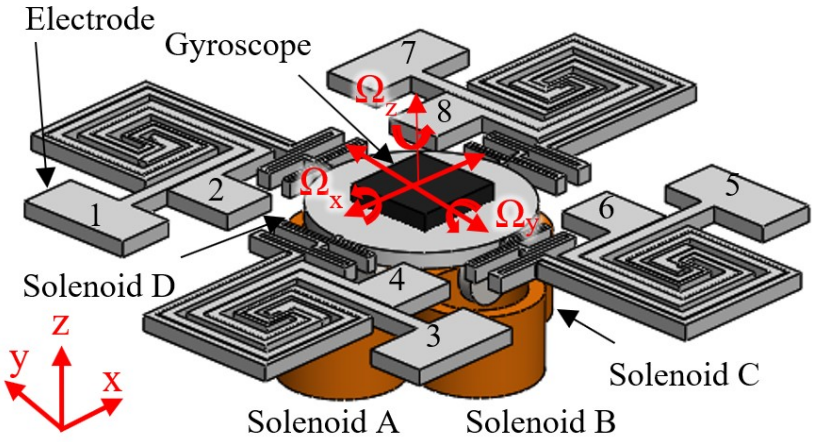

Figure 4.4: Piezoelectric dither stage with permanent magnets mounted underneath the dither stage and gyroscope on top. Solenoids are placed under the magnets to tilt the dither stage.

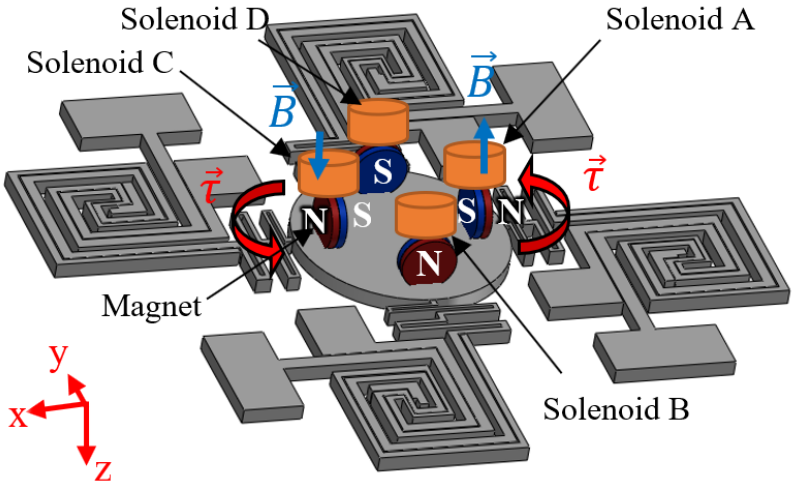

Figure 4.5: 3D view from the bottom side of the piezoelectric dither stage with 4 magnets.

The dither stage is actuated out-of-plane by using torque from the permanent magnets. The bottom side of the dither stage operating in Ω_y mode is shown in shown in Figure 4.5. Four permanent magnets are bonded to the dither stage such that the south pole of the magnets is oriented facing the center of the stage. For Ω_y mode, the dither stage is actuated by torque on the permanent magnet A and C due to magnetic field generated by the solenoids A and C.

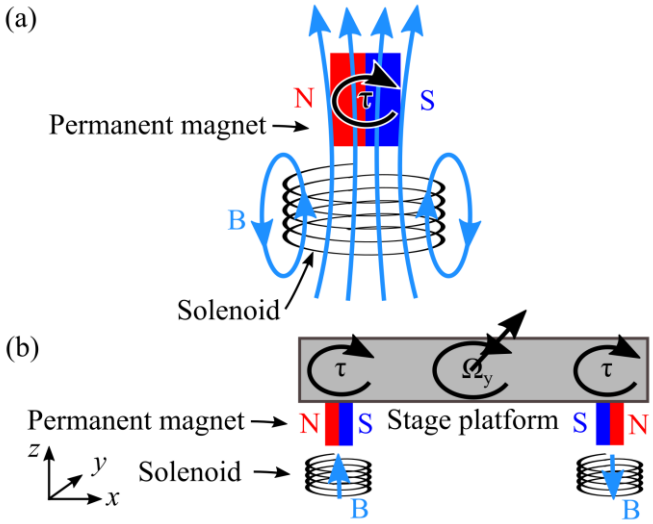

Figure 4.6: (a) The solenoid generates the magnetic field causing a torque on the permanent magnet. (b) Cross-sectional view piezoelectric dither stage operating in Ω_y mode.

For one magnet, magnetic field generated by one solenoid resulting in torque on the magnet is illustrated in Figure 4.6a. The magnet can be considered as a point dipole with total magnetic moment $\vec{\boldsymbol{m}}$. Magnetic field produced by the solenoid $\vec{\boldsymbol{B}}$ results in force $\vec{\boldsymbol{F}}$ and torque $\vec{\boldsymbol{\tau}}$ on the permanent magnet as [142],

$$\vec{\boldsymbol{F}} = \nabla(\vec{\boldsymbol{m}} \cdot \vec{\boldsymbol{B}}), \tag{4.1}$$

$$\vec{\boldsymbol{\tau}} = \vec{\boldsymbol{m}} \times \vec{\boldsymbol{B}}. \tag{4.2}$$

From (4.1), the dipoles of the magnets $\vec{\boldsymbol{m}}$ are perpendicular to the magnetic field $\vec{\boldsymbol{B}}$, so there is no force $\vec{\boldsymbol{F}}$ on the magnet. From (4.2), torque $\vec{\boldsymbol{\tau}}$ on the magnet is in the direction

attempting to rotate the magnet dipole to align with the magnetic field, as illustrated in Figure 4.6a. A cross-sectional view of the dither stage operating in Ω_y mode is shown in Figure 4.6b. When driving solenoids A and C with sinusoidal signal, the total torque generated by the two magnets will actuate the dither stage in Ω_y mode.

In order to calibrate the full range of rotation rate that can be measured by a gyroscope, the maximum angular rate applied by the dither stage should be comparable to the gyroscope full scale sensitivity because the angular rate is equivalent to the rotation rate measured by the gyroscope, as explained in 4.2.4. Using larger magnets and solenoids increases the maximum dither rate at the expense of increasing the size of the dither stage. To derive the angular rate, the dither stage can be considered as a torsional resonator driven by torque $\vec{\boldsymbol{\tau}} = \vec{\boldsymbol{m}} \times \vec{\boldsymbol{B}}$ generated by the magnets, as described in (4.2).

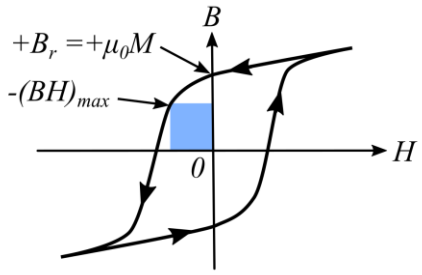

Figure 4.7: A hysteresis loop of a permanent magnet.

The magnetic moment $\vec{\boldsymbol{m}}$ is calculated from the permanent magnet specification. Most vendors define neodymium magnet grades as Nxx, where N indicates a neodymium magnet and xx is a 2-digit number representing the maximum magnet energy product $(BH)_{max}$ in the unit of mega Gauss Oersted (MGOe) [143]–[145]. The $(BH)_{max}$ is the maximum magnetic potential corresponding to the operation point with the maximum product of B and H on the hysteresis loop (Figure 4.7). The magnetic moment can be found from the relation [146],

$$-(BH)_{max} = \mu_0 \left(\frac{M}{2}\right)^2, \tag{4.3}$$

where M is the magnetic moment density, and μ_0 is the permeability of free space. Some vendors specify a residual magnetic field or remanence B_r, which is the magnetic field without an external magnetic field ($H = 0$) [143]. From the definition of H [142],

$$\vec{H} = \frac{1}{\mu_0}\vec{B} - \vec{M}, \tag{4.4}$$

the magnetic moment $\vec{m}$ can be found as

$$\vec{m} = V\vec{M} = \frac{1}{\mu_0} V\vec{B}_r, \tag{4.5}$$

where V is the permanent magnet volume. For this magnetic actuated dither stage, N50 neodymium magnets are used, so $(BH)_{max} = 50\ \mathrm{MGOe}$. From (4.3), the magnetic moment $\vec{m}$ can be calculated as

$$m = VM = 2V\sqrt{\frac{|(BH)_{max}|}{\mu_0}} = 0.99\ mA \cdot m^2. \tag{4.6}$$

This calculated magnetic moment may be larger than actual experimental values due to demagnetization over time.

The magnetic field produced by a solenoid is given by [142], [147],

$$B = \frac{\mu_0 nI}{2}\left(\frac{x+L/2}{\sqrt{(x+L/2)^2+R^2}} - \frac{x-L/2}{\sqrt{(x-L/2)^2+R^2}}\right) \tag{4.7}$$

where x is the distance measured from the center of the solenoid to the center of the magnet, n is the number of solenoid turns, I is the solenoid current, L is the length, and R is the radius of the solenoid. At low frequency far from the dither stage resonance, the dither angle amplitude is,

$$\theta_0 = \frac{2\tau}{\kappa_\theta} = \frac{\mu_0 nIm}{\kappa_\theta}\left(\frac{x+L/2}{\sqrt{(x+L/2)^2+R^2}} - \frac{x-L/2}{\sqrt{(x-L/2)^2+R^2}}\right) \tag{4.8}$$

where $\kappa_\theta = 2.87 \times 10^{-2}\ \mathrm{N \cdot m}$ is torsional spring constant. The angular rate at frequency f is $\Omega(\mathrm{t}) = 2\pi f \theta_0 \sin(\omega t)$.

After designing the dither stage with magnetic actuation, a prototype is assembled for 3-axis gyroscope calibration. The dither stage is fabricated on a PZT substrate and integrated with MAX21000 3-axis gyroscope, as described in 4.2.1. Four neodymium magnets (NanoAct N50, OD1.5x0.5 mm) are manually attached under the dither stage platform in lithographically defined cavities in the dither stage. The four solenoids that are used to generate a magnetic field for out-of-plane actuation are mounted on an acrylic sheet. The dither stage is assembled with a printed circuit board and the acrylic sheet such that the four solenoids are right under the four magnets. Sinusoidal currents with opposite polarities, $\pm I_a = \pm I_0 \sin(\omega t)$, are applied to the two solenoids with a combination shown in Table 4.5 to dither the stage in Ω_x or Ω_y modes.

Table 4.5 Solenoid current combinations for tilt dither modes.

Mode	**Solenoid**			
	A	***B***	***C***	***D***
Ω_x	0	$+V_a$	0	$-V_a$
Ω_y	$+V_a$	0	$-V_a$	0

The out-of-plane angular rate is applied to the MAX21000 3-axis gyroscope by magnetic actuation to dither the stage. The gyroscope is attached on the dither stage upside down and wire bonded to the dither stage board, as shown in Figure 4.8a. Figure 4.8b shows under the dither stage, where four solenoids are attached to the acrylic sheet. The dither rate is controlled by the amplitude and frequency of the current applied to the solenoids. Figure 4.8c shows a diagram of the system. MATLAB is used on a PC to control a calibration loop with the MBED LPC1768 microcontroller and an Agilent 33500B function generator. The MBED initializes and reads the angular rates from the gyroscope while actuated by the dither stage. The function generator changes voltage and frequency of the output to control the dither rate. For the piezoelectric in-plane

dither mode, outputs from function generator are amplified 20 times to 100 V amplitude by PiezoDrive PDM200 miniature high voltage amplifier. To change dither stage operation mode, the MBED sends square pulses to switches latching mechanical relays into electrode combinations shown in Table 2.1 and Table 4.5. For magnetic actuation, a function generator (Agilent 33500B) drives the two solenoids in series to guarantee that the current in both coils is matched, generating force in the opposite directions.

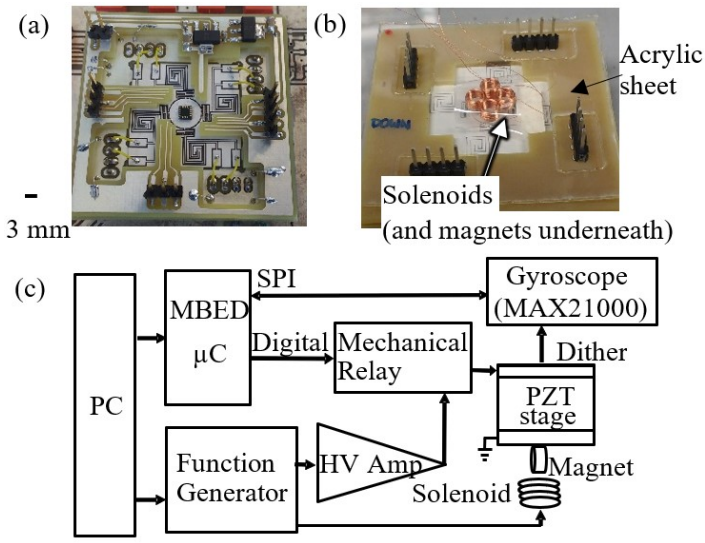

Figure 4.8: (a) Top view: MAX21000 3-axis gyroscope attached on the dither stage (b) Bottom view: solenoids mounted close to the magnets. (c) Diagram of the calibration system.

4.2.4 Angular rate and acceleration of a dither stage

The dither stage oscillates at small amplitudes to calibrate IMUs, consisting of gyroscopes and accelerometers. For gyroscope calibration, the dither stage oscillates at small angles to generate angular rate, which is equivalent to a rotation rate at a short period of time [61], [130]. The dither stage should be able to actuate the gyroscope with angular rate comparable to the maximum rotation rate that the gyroscope can measure so that the dither stage can calibrate most of the gyroscope full-scale range. The angular rate depends on the frequency and the amplitude of the oscillation, which will be derived

in this section. The frequency should be much lower than the -3 dB bandwidth of the gyroscope to achieve accurate calibration without attenuating gyroscope output. The dither angle amplitude should be smaller than the angle operating in nonlinear regime to actuate the gyroscope with precise sinusoidal angular rate. For accelerometer calibration, the dither stage oscillates over small linear distances to generate acceleration. Therefore, to evaluate the efficacy of an IMU calibration stage design, it is important to be able to estimate the theoretical angular rate and acceleration that the design can achieve.

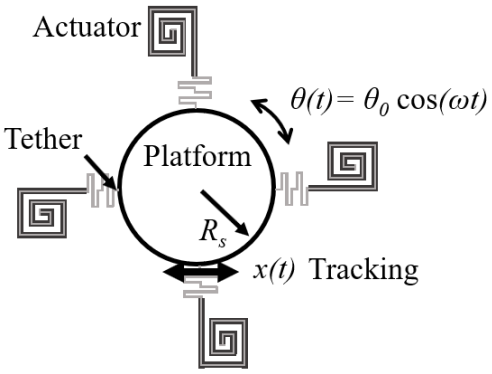

Figure 4.9: A schematic shows a dynamic of dither stage with the angular dither angle θ(t) and edge displacement x(t).

Dither stage dynamic is investigated to derive the angular rate, which is equivalent to the rotation rate measured by gyroscopes. Different angular rates are applied to the gyroscope for scale factor calibration to correct scale factor error, as explained in 4.2.5. A schematic of a dither stage with a circular platform radius R_s is shown in Figure 4.9. The dither stage is dithered with an angular amplitude θ_0 at an angular frequency ω, the dither stage angle, angular rate, and angular acceleration are,

$$\theta_\theta(t) = \theta_0 \cos(\omega t) \tag{4.9}$$

$$\Omega_\theta(t) = -\omega\theta_0 \sin(\omega t) \tag{4.10}$$

$$\alpha_\theta(t) = -\omega^2\theta_0 \cos(\omega t) \tag{4.11}$$

where $\theta_\theta(t)$ is the angle of the dither stage as a function of time *t,* Ω_θ is the angular rate, α_θ is the angular dither acceleration. Thus, the angular rate amplitude applied to IMU for gyroscope calibration is,

$$\Omega_{\theta 0} = \omega\theta_0 \tag{4.12}$$

where $\Omega_{\theta 0}$ is the angular rate amplitude. In this case, the angular rate $\Omega_{\theta 0}$ is linearly proportional to the frequency when the dither angle amplitude θ_0 is fixed. For the dither stage calibration by the stroboscopic technique described in Section 4.3.1, the dither stage edge displacement $x_\theta(t)$ for small dither amplitude θ_0 is

$$x_\theta(t) = R_s\theta_0\cos(\omega t) \tag{4.13}$$

where R_s is the dither stage radius.

For acceleration mode testing, the dither stage is dithered with displacement amplitude x_0 at an angular frequency ω, the dither stage displacement x_{Ax}, linear velocity v_{Ax} and, linear acceleration a_{Ax} are

$$x_{Ax}(t) = x_0\cos(\omega t) \tag{4.14}$$

$$v_{Ax}(t) = -\omega x_0\sin(\omega t) \tag{4.15}$$

$$a_{Ax}(t) = -\omega^2 x_0\cos(\omega t) \tag{4.16}$$

where $x_{Ax}(t)$ is the angle of the dither stage as a function of time *t*. Thus, the acceleration amplitude applied to IMU is,

$$a_{Ax0} = \omega^2 x_0 \tag{4.17}$$

where a_{Ax0} is the acceleration amplitude. In this case, the acceleration amplitude a_{Ax0} is proportional to the frequency squared when the dither displacement amplitude x_0 is fixed. As will be seen later in 4.3.1 and 4.3.3, the angular dither rate will show a linear

response as a function of frequency and the acceleration will show a quadratic response, as predicted by (4.12) and (4.17).

4.2.5 IMU error model

The error model of an inertial measurement unit (IMU) is investigated to derive how to use parameters obtained from the gyroscope calibration to reduce gyroscope errors. One of the most common IMU architecture is the 6-axis IMU integrating 3-axis accelerometers and 3-axis gyroscopes. In this section, an expression for correcting all 6-axis IMU outputs is derived. The expression can be used for 1-axis or 3-axis gyroscopes calibration by setting unknown terms to the ideal scenario.

All types of IMUs suffers from bias errors, scale factor errors, cross-axis errors, misalignment errors, thermal noise, and external electromagnetic interferences [34]. Other IMU errors depend on the IMU types such as quantization noise and vibration-induced error. Each IMU error source further consists of several components, including a fixed error term which is unchanged and error terms that vary from run-to-run (between each use), vary with temperature, or vary in-run (while using) [34]. Fixed errors such as manufacturing process variation can be minimized by factory calibration [136]. Run-to-run variations can be minimized by calibrating before each use [34]. Temperature-dependent variations can be compensated by equations or look-up tables created from IMU outputs calibrated in temperature control environment [148]. In-run variation can be minimized by in-run calibrations and sensor fusions [97], [102], [122].

IMU errors can be modeled as a relation between applied versus measured acceleration and rotation rate. Applied acceleration vector $\vec{\boldsymbol{a}}$ and acceleration measured by the accelerometer $\vec{\boldsymbol{a}}_{\boldsymbol{out}}$ can be written as:

$$\vec{\boldsymbol{a}} = \begin{bmatrix} a_x & a_y & a_z \end{bmatrix}^T, \qquad \vec{\boldsymbol{a}}_{\boldsymbol{out}} = \begin{bmatrix} a_{x,out} & a_{y,out} & a_{z,out} \end{bmatrix}^T, \tag{4.18}$$

where a_x, a_y, and a_z are component of $\vec{a}$, $a_{x,out}$, $a_{y,out}$, and $a_{z,out}$ are component $\vec{\boldsymbol{a}}_{\boldsymbol{out}}$, and the superscripted *T* represents transposed matrices. Similarly, applied rotation vector $\vec{\Omega}$ and rotation measured by the gyroscope $\vec{\boldsymbol{\Omega}}_{\boldsymbol{out}}$ can be written as:

$$\vec{\boldsymbol{\Omega}} = \begin{bmatrix} \Omega_x & \Omega_y & \Omega_z \end{bmatrix}^T, \quad \vec{\boldsymbol{\Omega}}_{\boldsymbol{out}} = \begin{bmatrix} \Omega_{x,out} & \Omega_{y,out} & \Omega_{z,out} \end{bmatrix}^T, \tag{4.19}$$

where Ω_x, Ω_y, and Ω_z are component of $\vec{\boldsymbol{\Omega}}$, and $\Omega_{x,out}$, $\Omega_{y,out}$, and $\Omega_{z,out}$ are component $\vec{\boldsymbol{\Omega}}_{\boldsymbol{out}}$. Scale factor error, misalignment error, and cross-axis error can be written as a transformation matrix $\bar{\boldsymbol{M}}_{\boldsymbol{a}}$ as [34]:

$$\vec{\boldsymbol{a}}_{\boldsymbol{out}} = \bar{\boldsymbol{M}}_{\boldsymbol{a}}\vec{\boldsymbol{a}} = \begin{bmatrix} s_{a,x} & m_{a,xy} & m_{a,xz} \\ m_{a,yx} & s_{a,y} & m_{a,yz} \\ m_{a,zx} & m_{a,zy} & s_{a,z} \end{bmatrix} \begin{bmatrix} a_x \\ a_y \\ a_z \end{bmatrix}, \tag{4.20}$$

$$\vec{\boldsymbol{\Omega}}_{\boldsymbol{out}} = \bar{\boldsymbol{M}}_{\boldsymbol{g}}\vec{\boldsymbol{\Omega}} = \begin{bmatrix} s_{g,x} & m_{g,xy} & m_{g,xz} \\ m_{g,yx} & s_{g,y} & m_{g,yz} \\ m_{g,zx} & m_{g,zy} & s_{g,z} \end{bmatrix} \begin{bmatrix} \Omega_x \\ \Omega_y \\ \Omega_z \end{bmatrix}, \tag{4.21}$$

where the diagonal elements s_x, s_y, and s_z are scale factor error in x, y, and z axes, and the off-diagonal elements m are cross-axis error and misalignment error. Gyroscope responds to acceleration can be written as a transformation matrix $\bar{\boldsymbol{G}}_{\boldsymbol{g}}$ as:

$$\vec{\boldsymbol{\Omega}}_{\boldsymbol{out}} = \bar{\boldsymbol{G}}_{\boldsymbol{g}}\vec{\boldsymbol{a}} = \begin{bmatrix} g_{xx} & g_{xy} & g_{xz} \\ g_{yx} & g_{yy} & g_{yz} \\ g_{zx} & g_{zy} & s_{zz} \end{bmatrix} \begin{bmatrix} a_x \\ a_y \\ a_z \end{bmatrix}, \tag{4.22}$$

where the elements g are vibration sensitivity. The bias and thermal noise of the accelerometers and gyroscopes can be written as:

$$\vec{\boldsymbol{b}}_{\boldsymbol{a}} = \begin{bmatrix} b_{ax} & b_{ay} & b_{az} \end{bmatrix}^T, \qquad \vec{\boldsymbol{w}}_{\boldsymbol{a}} = \begin{bmatrix} w_{ax} & w_{ay} & w_{az} \end{bmatrix}^T, \tag{4.23}$$

$$\vec{\boldsymbol{b}}_{\boldsymbol{g}} = \begin{bmatrix} b_{gx} & b_{gy} & b_{gz} \end{bmatrix}^T, \qquad \vec{\boldsymbol{w}}_{\boldsymbol{g}} = \begin{bmatrix} w_{gx} & w_{gy} & w_{gz} \end{bmatrix}^T, \tag{4.24}$$

where $\vec{b}_a$ is the accelerometer bias, $\vec{w}_a$ is the accelerometer thermal noise, $\vec{b}_g$ is the gyroscope bias, and $\vec{w}_g$ is the gyroscope thermal noise. An example of accelerometer bias $\vec{b}_a$ can be written as:

$$\vec{b}_a = \vec{b}_{a,fixed} + \vec{b}_{a,run} + \vec{b}_{a,temp}(T) + \vec{b}_{a,in}, \tag{4.25}$$

where $\vec{b}_{a,fixed}$ is a fixed error, $\vec{b}_{a,run}$ is run-to-run variation, $\vec{b}_{a,temp}(T)$ is temperature-dependent variation, and $\vec{b}_{a,in}$ is in-run variation.

From (4.18) to (4.25), the IMU output error can be written as:

$$\vec{a}_{out} = \bar{M}_a\vec{a} + \vec{b}_a + \vec{w}_a, \tag{4.26}$$

$$\vec{\Omega}_{out} = \bar{M}_g\vec{\Omega} + \vec{b}_g + \bar{G}_g\vec{a} + \vec{w}_g, \tag{4.27}$$

where $\vec{a}_{out}$ is the 3-axis accelerometer measured output, $\vec{a}$ is the 3-axis applied acceleration, $\vec{\Omega}_{out}$ is the 3-axis gyroscope measured output, $\vec{\Omega}$ is the 3-axis applied rotation input. Knowing the cross-coupling and bias terms allows one to make the following corrections [34],

$$\vec{a}_{corrected} = \bar{M}_a{}^{-1}(\vec{a}_{out} - \vec{b}_a), \tag{4.28}$$

$$\vec{\omega}_{corrected} = \bar{M}_a{}^{-1}(\vec{\omega}_{out} - \vec{b}_g - \bar{G}_g\vec{a}), \tag{4.29}$$

with accuracies limited by the thermal noise $\vec{w}_a$ and $\vec{w}_g$ and in-run variations.

4.2.6 The Brownian motion of a dither stage

The Brownian motion of a dither stage due to thermal noise may contribute to the gyroscope calibration error. The dither stage angular rate noise spectral density and the RMS value are analyzed and quantified in this section to ensure that the Brownian motion adds negligible noise to the gyroscope. A diagram of the dither stage mechanical system as a torsional resonator is shown in Figure 4.10. In this figure, θ is the dither

stage displacement angle, κ_θ is the torsional spring constant, I_θ is the moment of inertia, and b_θ is the damping coefficient, and τ_θ is the torque applied on the dither stage.

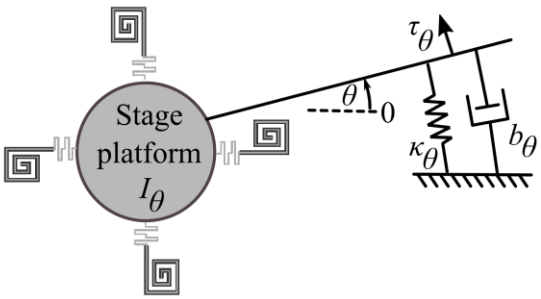

Figure 4.10: A schematic shows a torsional resonator mechanical model for the dither stage.

In electrical and mechanical systems, noise spectral density can be obtained by adding noise generators next to damping elements [8]. For an electrical system, voltage noise generators added in series with every resistor has a spectral density described by the well-known Johnson-Nyquist relation [149], [150],

$$\bar{V}_N = \sqrt{4k_B TR}, \qquad \left[\frac{V}{\sqrt{Hz}}\right], \tag{4.30}$$

where is k_B the Boltzmann constant, T is the temperature and R is the resistance. For mechanical system, voltage noise generators are added in series with every resistor with a spectral density [151],

$$\bar{F}_N = \sqrt{4k_B Tb}\,, \qquad \left[\frac{N}{\sqrt{Hz}}\right], \tag{4.31}$$

where is b is the damping coefficient.

The dither stage can be modeled as a torsional resonator shown in Figure 4.10. The noise generator for a torsional resonator may differ from the noise generator for a mechanical system in (4.30). For systems in thermal equilibrium, irreversible thermodynamics requires one to add a noise generator for every loss mechanism [152]. From fluctuation-dissipation theorem, dissipated energy will be replenished by noise

generators to reach thermal equilibrium. Noise spectral density due to Brownian motion mainly depends on the damping mechanisms [153]. External velocity damping such as viscous fluid damping results in white noise, while internal displacement damping such as internal friction results in 1/f noise [153], [154]. The dither stage operates in air, so energy loss is dominated by viscous air damping modeled by a damping coefficient b_θ. To analyze the noise, an equation of motion of the dither stage in Ω_z mode is

$$I_\theta \frac{\partial^2}{\partial t^2}\theta + b_\theta \frac{\partial}{\partial t}\theta + \kappa_\theta \theta = \tau_\theta, \tag{4.32}$$

where t is time. This equation can be solved in the Fourier domain to get the displacement angle solution as:

$$\theta = \frac{\tau_\theta/\kappa_\theta}{1+j\omega/(\omega_0 Q)-\omega^2/\omega_0^2}, \tag{4.33}$$

where the resonance frequency is

$$\omega_0 = \sqrt{\kappa_\theta/I_\theta}, \tag{4.34}$$

and the quality factor is

$$Q = \omega_0 I_\theta / b_\theta. \tag{4.35}$$

Consider a torque due to noise $\bar{\tau}_{\theta N}$, the equation of motion from (4.32) becomes,

$$I_\theta \frac{\partial^2}{\partial t^2}\theta + b_\theta \frac{\partial}{\partial t}\theta + \kappa_\theta \theta = \bar{\tau}_{\theta N} \tag{4.36}$$

Taking derivative on both sides, the equation of motion becomes,

$$I_\theta \frac{\partial^3}{\partial t^3}\theta + b_\theta \frac{\partial^2}{\partial t^2}\theta + \kappa_\theta \frac{\partial}{\partial t}\theta = \frac{\partial}{\partial t}\tau_{\theta N}\ . \tag{4.37}$$

The solution for the angular velocity in Fourier domain is,

$$\dot{\theta} = \frac{1}{b_\theta}\left(\frac{\tau_\theta}{j\omega I_\theta/b_\theta+1+\kappa_\theta/(j\omega b_\theta)}\right). \tag{4.38}$$

The energy spectral density E is,

$$E = \frac{1}{2} I_\theta \left|\bar{\dot{\theta}}\right|^2 = \frac{1}{2} I_\theta \frac{1}{b_\theta^2} \left(\frac{\overline{\tau_\theta^2}}{\left(1 + \frac{j\omega I_\theta}{b_\theta} + \frac{\kappa_\theta}{j\omega b_\theta}\right)\left(1 - \frac{j\omega I_\theta}{b_\theta} - \frac{\kappa_\theta}{j\omega b_\theta}\right)} \right). \tag{4.39}$$

The energy spectral density can be simplified as,

$$E = \frac{1}{2} I_\theta \frac{1}{b_\theta^2} \left(\frac{\overline{\tau_\theta^2}}{1 + Q^2\left(\frac{\omega}{\omega_0} - \frac{\omega_0}{\omega}\right)^2} \right). \tag{4.40}$$

The internal energy for all frequency spectrum U is,

$$U = \int_{f=0}^{\infty} E \, df = \int_{f=0}^{\infty} \frac{1}{2} Q \frac{1}{\omega_0 b_\theta} \left(\frac{\overline{\tau_\theta^2}}{1 + Q^2\left(\frac{\omega}{\omega_0} - \frac{\omega_0}{\omega}\right)^2} \right) df. \tag{4.41}$$

The internal energy U can be simplified as [8],

$$U = \frac{1}{4\pi b_\theta} \overline{\tau_\theta^2} \int_{f=0}^{\infty} \left(\frac{Q}{1 + Q^2\left(\frac{f}{f_0} - \frac{f_0}{f}\right)^2} \right) df/f_0 = \frac{1}{8 b_\theta} \overline{\tau_\theta^2}. \tag{4.42}$$

From the equipartition theorem, the noise generator can be obtained by equating U to $k_b T/2$. The torque due to Brownian motion is,

$$\bar{\tau}_{\theta N} = \sqrt{4 k_B T b_\theta} \qquad \left[\frac{\text{N·m}}{\sqrt{\text{Hz}}}\right]. \tag{4.43}$$

The noise generator torque $\bar{\tau}_{\theta N}$ is very similar to voltage and force noise generators in (4.30) and (4.31).

The dither stage operates at the frequency range much lower than the resonance frequency ($\omega \ll \omega_0$). The Fourier domain solution of the displacement angle in (4.33) can be simplified to $\bar{\tau}_{\theta N}/\kappa_\theta$ as

$$\bar{\theta}_N = \frac{\sqrt{4 k_B T b_\theta}}{\kappa_\theta} \qquad \left[\frac{\text{rad}}{\sqrt{\text{Hz}}}\right]. \tag{4.44}$$

From the parameters in Section 4.3.2, the angle noise spectral density at temperature 300 K can be estimated as,

$$\bar{\theta}_N = \frac{\sqrt{4k_B T b_\theta}}{\kappa_\theta} = 3.02 \times 10^{-11} \ \frac{\text{deg}}{\sqrt{\text{Hz}}} \tag{4.45}$$

From $\bar{\Omega}_{\theta N} = 2\pi f \bar{\theta}_N$ described in (4.12), angular rate noise applied to the gyroscope in the calibration frequency range ($\omega \ll \omega_0$) is,

$$\bar{\Omega}_{\theta N} = 2\pi \frac{\sqrt{4k_B T b_\theta}}{\kappa_\theta} f \qquad \left[\frac{\text{rad/s}}{\sqrt{\text{Hz}}}\right] \tag{4.46}$$

From the parameters in Section 4.3.2, angular rate noise applied to the gyroscope at temperature 300 K for maximum dither rate at 150 Hz can be estimated as,

$$\bar{\Omega}_{\theta N} = 2.84 \times 10^{-8} \ \frac{\text{deg/s}}{\sqrt{\text{Hz}}} = 0.286 \frac{\text{PPB}}{\sqrt{\text{Hz}}} \tag{4.47}$$

From the equipartition theorem, energy stored in the dither stage in each mode is $k_b T/2$. The potential energy can be equated to $k_b T/2$ to find a root-mean-square (RMS) of displacement angle noise as,

$$U = \frac{1}{2} k_b T = \frac{1}{2} \kappa_\theta \bar{\theta}^2 \tag{4.48}$$

The displacement angle noise is

$$\bar{\theta}_{RMS} = \sqrt{\frac{k_b T}{\kappa_\theta}} = 2.20 \times 10^{-8} \text{ deg.} \tag{4.49}$$

Similarly, the kinetic energy can be equated to $k_b T/2$ as,

$$U = \frac{1}{2} k_b T = \frac{1}{2} I_\theta \bar{\dot{\theta}}^2 \tag{4.50}$$

From the parameters in Section 4.3.2, the angular rate noise applied to the gyroscope at temperature 300 K for maximum dither rate at 150 Hz can be estimated as,

$$\bar{\dot{\theta}}_{RMS} = \sqrt{\frac{k_b T}{I_\theta}} = 1.23 \times 10^{-4} \frac{deg}{s} = 1.24 \text{ PPM} \tag{4.51}$$

Equations (4.47) and (4.51) indicate that angular rate noise spectral density due to Brownian motion is as low as $0.286 \text{ PPB}/\sqrt{\text{Hz}}$ and RMS noise is 1.24 PPM. This noise is negligible compared to the dither stage repeatability of 50 PPM [13].

4.3 Results

After the dither stage was designed, fabricated, and integrated into a system, as discussed in the previous section, the prototype was characterized, and gyroscope calibration was demonstrated. The dither stage operating in the in-plane modes (Ω_z, A_x and A_y) is calibrated by the stroboscopic technique, as explained in 4.3.1 to measure the angular rate as a function of applied voltage. In 4.3.2, the dither stage is characterized as a torsional resonator to measure or calculate parameters such as quality factor, mechanical bandwidth, torsional spring constant, moment of inertia, and damping coefficient. These parameters are used for choosing the frequency for gyroscope calibration in 4.3.3 and calculating noise in 4.2.6. In 4.3.3, the dither stage is driven in the in-plane modes (Ω_z, A_x and A_y) by piezoelectric actuation. Six-axis IMU output is measured to demonstrate gyroscope and accelerometer calibration capability. The output is compared with an IMU output calibrated by a commercial rate table and a commercial shaker table. In 4.3.4, the dither stage is driven in the out-of-plane modes (Ω_x and Ω_y) by magnetic actuation. IMU outputs are extracted to demonstrate 3-axis gyroscope calibration capability of the dither stage.

4.3.1 Dither stage calibration by the stroboscopic technique

The dither stage is calibrated by the stroboscopic technique using Polytec MSA-400 microsystem analyzer to measure angular rate versus drive frequency at fixed voltage. The stroboscopic technique captures slow-motion videos of the dither stage moving at the frequency higher than the image sensor frame rate by recording each

frame at different phases of the excitation voltage. The edge displacement $x(t)$, previously explained in (4.13), is measured by tracking image movement in the microscope video (Figure 4.11). The edge displacement $x(t)$ is fit to sine wave model to extract amplitude. The dither stage is actuated by sinusoidal voltage with fixed amplitude at 100 V and swept frequency from 5 Hz to 150 Hz. The angular rate Ω_z and acceleration A_x and A_y of the dither stage in 3 modes is calculated from (4.12) and (4.17), and plotted in Figure 4.12. The dither stage is integrated with the IMU chip wire bonded to the dither stage board.

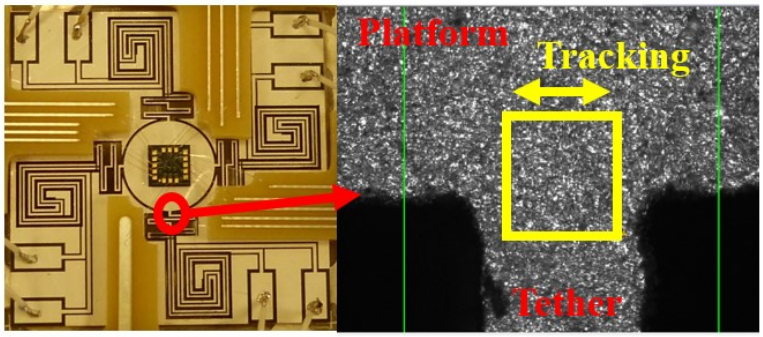

Figure 4.11: The dither stage is calibrated by a stroboscopic technique by tracking stage displacement.

The dither stage scale factors are extracted from Figure 4.12 by a linear fit for Ω_z mode and a quadratic fit for A_x and A_y modes. For an angular mode Ω_z, the angular rate Ω_z is fit to the model:

$$\Omega = c_{s\Omega} f, \tag{4.52}$$

where $c_{s\Omega}$ is the stage scale factor for angular modes, and f is the frequency of the driving voltage. For acceleration modes (A_x and A_y), the acceleration is fit to the model:

$$A = c_{sa} f^2, \tag{4.53}$$

where c_{sa} is the stage scale factor for acceleration modes. The dither stage scale factors for the modes Ω_z, A_x and A_y for fixed drive voltage of 100 V are shown in Table 4.6.

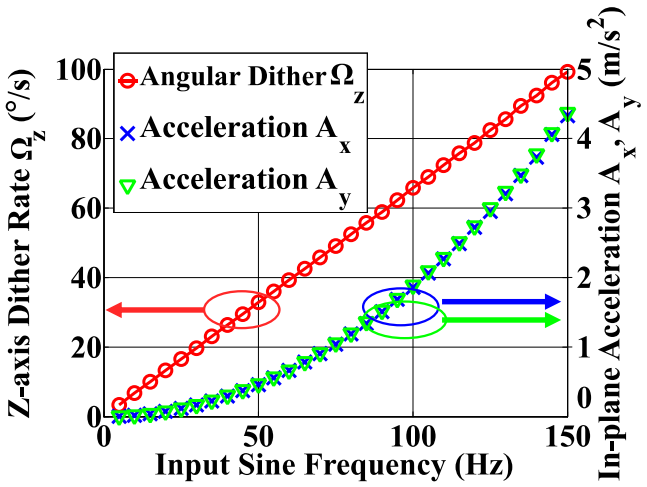

Figure 4.12: Dither stage response under 3 dither modes: (i) Rotational, (ii) X-translation, and (iii) Y-translation as measured by in-plane stroboscopy (Polytec MSA-400 Micro System Analyzer).

Table 4.6: Dither stage scale factor at fixed voltage amplitude of 100 V.

Variables	Dither modes	Stage scale factor	Unit
c_{sax}	X-axis acceleration (A_x)	201 ± 3	(μm/s^2)/Hz^2
c_{say}	Y-axis acceleration (A_y)	202 ± 3	(μm/s^2)/Hz^2
$c_{s\Omega z}$	Z-axis rotation (Ω_z)	0.662 ± 0.002	(Degree/s)/Hz

4.3.2 Dither stage characterization

A finite element method (FEM) model of the dither stage was simulated in COMSOL to extract parameters for a lumped torsional resonator previously shown in Figure 4.10. These parameters are used for determining the frequency for IMU calibration in 4.3.3 and for calculating noise, as discussed in 4.2.6. Only the PZT part of the dither stage is modeled in the FEM study. The electrodes are modeled as a voltage potential, and the integrated IMU is modeled as loading masses. The magnetic actuation is modeled as equivalent point forces acting on the location that the circular platform edge connects to the spring.

From the COMSOL eigenfrequency study, the resonance mode shapes are shown in Figure 4.13. The resonance frequencies extracted from the FEM model are 846 Hz for the x- and y-axis dither modes, and 835 Hz for the z-axis dither mode. The high resonance frequency allows high bandwidth operation of the dither stage for calibration. From the COMSOL model, the cross-axis coupling for out-of-plane mode by magnetic actuation is determined to be 70 ppm. The out-of-plane acceleration of 70 ppm should not affect gyroscope operation. From a stationary study simulation in COMSOL, the in-plane torsional spring constant k_θ was determined to be 2.81×10^{-2} N-m and the out-of-plane torsional spring constant k_θ was determined to be 2.87×10^{-2} N-m.

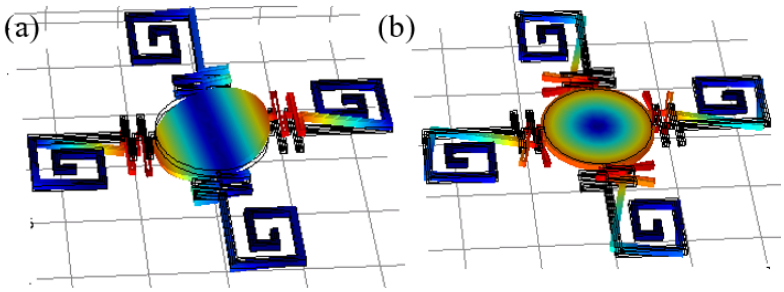

Figure 4.13: Dither stage mode shape from COMSOL simulation (a) out-of-plane mode shape with resonance frequency 846 Hz (b) in-plane mode with resonance frequency 835 Hz.

From the stroboscopic measurement in Chapter 5, the Ω_z mode resonance frequency was measured to be 893 Hz with a quality factor of 380. From (4.34), the moment of inertia is

$$I_\theta = \frac{\kappa_\theta}{\omega_0^2} = 8.93 \times 10^{-10}\ \text{kg} \cdot \text{m}^2. \tag{4.54}$$

From (4.35), the PZT dither damping coefficient is

$$b_\theta = \frac{\omega_0 I_\theta}{Q} = 1.32 \times 10^{-8}\ \text{kg} \cdot \text{m}^2/\text{s}. \tag{4.55}$$

The dither stage parameters are summarized in Table 4.7. The dither stage has a resonance frequency of 893 Hz, so the gyroscope calibration at the frequency range 5-150 Hz in Section 4.3.3 is much lower than the resonance frequency as designed. The dither stage mechanical bandwidth is f_0/Q = 2.35 Hz, allowing rapid settling time when changing frequency.

Table 4.7: The dither stage parameters for Ω_z dither mode.

Description	**Variable**	**Quantity**	**Unit**
Resonance frequency	f_0	893	Hz
Quality factor	Q	380	-
Mechanical bandwidth	f_{BW}	2.35	Hz
Torsional spring constant	κ_θ	2.81×10^{-2}	$\mathrm{N \cdot m}$
Moment of inertia	I_θ	8.93×10^{-10}	$\mathrm{kg \cdot m^2}$
Damping coefficient	b_θ	1.32×10^{-8}	$\mathrm{kg \cdot m^2/s}$

4.3.3 IMU calibration on the dither stage

The IMU output rotation rate and acceleration are recorded while actuating the dither stage to demonstrate gyroscope calibration. In order to extract scale factors, the output data rate of the IMU is set to 2 kHz, and 6 axis data are acquired. During this calibration process, the dithering frequency is swept, at constant amplitude, from 5 to 150 Hz in steps of 5 Hz. The IMU output full scale is set to ± 125 °/s for the gyroscopes and ± 2 g for the accelerometers. For each dither frequency, the raw data is recorded by the MBED for 0.5 seconds and sent to MATLAB for data processing. For each axis of actuation, all of the 6-axis output signals for the IMU are measured and stored. An example of the IMU output from Ω_z mode dither at 15 Hz is shown in Figure 4.14. In this plot, the IMU z-axis gyroscope output ω_z has a high signal-to-noise ratio because the excitation is in Ω_z axis. The outputs from other axes are noisy because the signals

are driven by cross-axis coupling. The 6-axis outputs are fitted to a sine wave model to extract signal amplitude. The plots for measured data are shown in blue, while the fitted sine waves are shown in red. The data is plotted in the unit of least significant bit (LSB), which can be converted to acceleration in m/s^2 and rotation rate in degree/s from scale factor shown in Table 4.10.

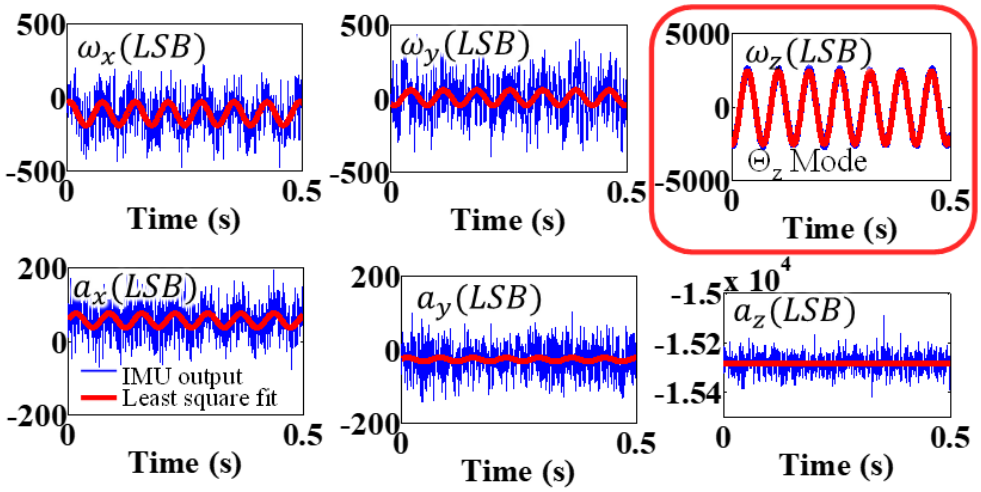

Figure 4.14: An example of the time domain outputs of the 6-axis IMU in Ω_z mode at the dither frequency 15 Hz.

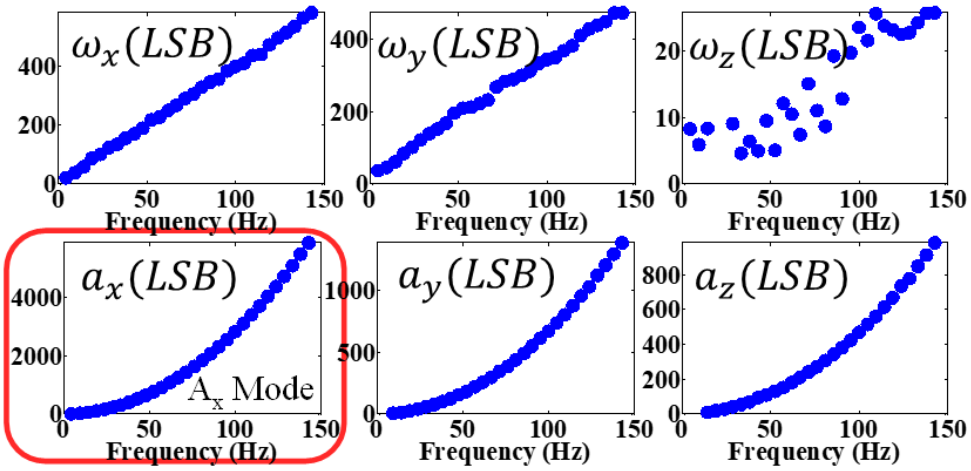

Figure 4.15: The output amplitudes of the 6-axis IMU versus the dither frequency in the A_x excitation mode.

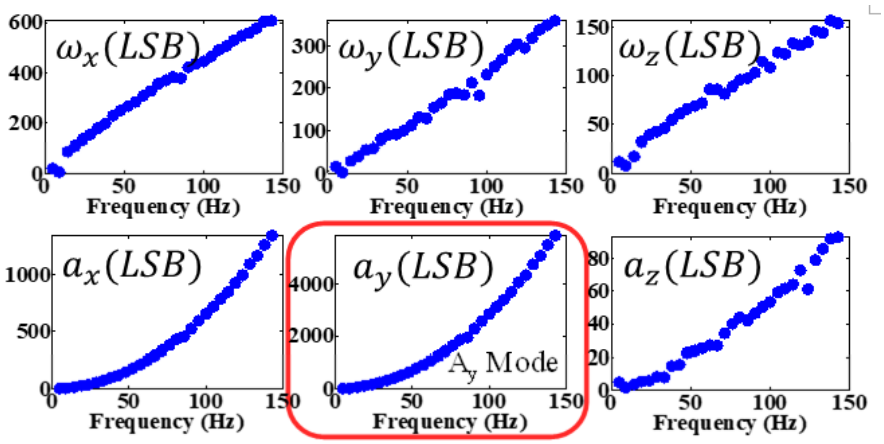

Figure 4.16: The output amplitudes of the 6-axis IMU versus the dither frequency in A_y excitation mode.

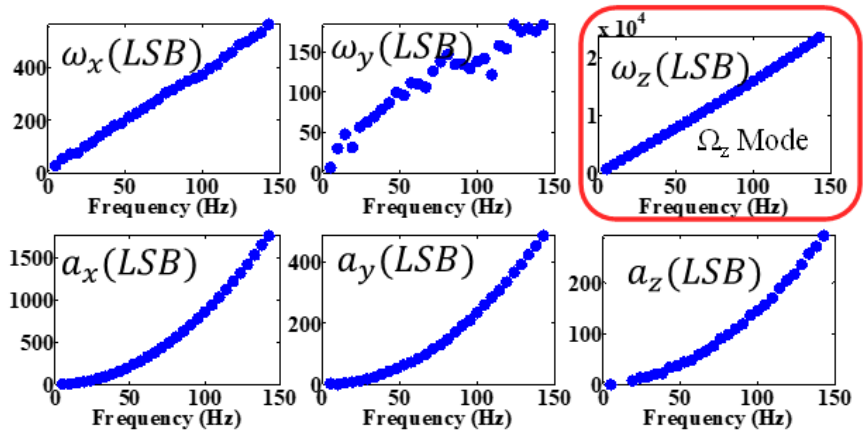

Figure 4.17: The output amplitudes of the 6-axis IMU versus the dither frequency in Ω_z excitation mode.

The dither frequency is swept from 5 to 150 Hz in steps of 5 Hz, while dither stage drive voltage is held constant at 100 V. At each drive frequency, 6-axis outputs are plotted and the amplitude is extracted, similar to Figure 4.14. The extracted amplitude of the 6-axis output as a function of dither frequency for A_x, A_y, and Ω_z modes are shown in Figure 4.15 - Figure 4.17, respectively. In these plots, the IMU output corresponding to excitation is marked in red. The IMU outputs in other axes are excited by cross-axis coupling; therefore, the output has lower amplitude and higher SNR.

Table 4.8: The extracted output dependence of the 3 gyroscopes in 3 different excitation modes calibrated with the fixed amplitude of 100 V and swept frequency 5-150 Hz.

Dither Mode	**Coefficient c_g extracted from the gyroscope outputs (LSB/Hz)**		
	X-axis	**Y-axis**	**Z-axis**
A_x	3.97 ± 0.05	3.18 ± 0.07	0.18 ± 0.03
A_y	4.2 ± 0.2	2.5 ± 0.1	1.03 ± 0.05
Ω_z	3.76 ± 0.06	1.1 ± 0.1	164 ± 2

Table 4.9: The extracted output quadratic dependence of the 3 accelerometers in 3 different excitation modes calibrated with the fixed amplitude of 100 V and swept frequency 5-150 Hz.

Dither Mode	**Coefficient c_a extracted from the accelerometer outputs (LSB/Hz^2)**		
	X-axis	**Y-axis**	**Z-axis**
A_x	0.288 ± 0.001	0.0677 ± 0.0002	0.0478 ± 0.0003
A_y	0.0663 ± 0.0004	0.287 ±0.002	0.0044 ± 0.0003
Ω_z	0.0864 ± 0.0004	0.0240 ± 0.0002	0.0142 ± 0.0002

The calibrated gyroscope and accelerometer scale factors are extracted from Figure 4.15 - Figure 4.17 by linear fitting to the gyroscope outputs and quadratic fitting to the accelerometer outputs. For example, the z-axis gyroscope output ω_z actuated in Ω_z mode (Figure 4.17) is fitted to a linear model:

$$\omega_z = c_{gz} f, \tag{4.56}$$

to extract the coefficient c_{gz} where f is the dither stage frequency. The c_g coefficients that were extracted from 3-axis gyroscopes actuated in 3 modes are shown in Table 4.8. The x-axis and y-axis accelerometer output a_x and a_y actuated in A_x and A_y modes (Figure 4.15 and Figure 4.16) are fitted to models:

$$a_x = c_{ax} f^2, \qquad a_y = c_{ay} f^2, \tag{4.57}$$

to extract the coefficient c_{ax} and c_{ay}. Coefficients c_a extracted from 3-axis accelerometers actuated in 3 modes are shown in Table 4.9. The gyroscope and accelerometer scale factor can be calculated from the dither stage scale factor $c_{s\Omega z}$, c_{sax} and c_{say} from Table 4.6 as,

$$s_{g,z} = c_{s\Omega z}/c_{gz}, \qquad s_{a,x} = c_{sax}/c_{ax}, \qquad s_{a,y} = c_{say}/c_{ay}, \tag{4.58}$$

where $s_{g,z}$, $s_{a,x}$, and $s_{a,y}$ are the scale factors of z-axis gyroscope, x-axis accelerometer, and y-axis accelerometer, as explained in (4.20) and (4.21).

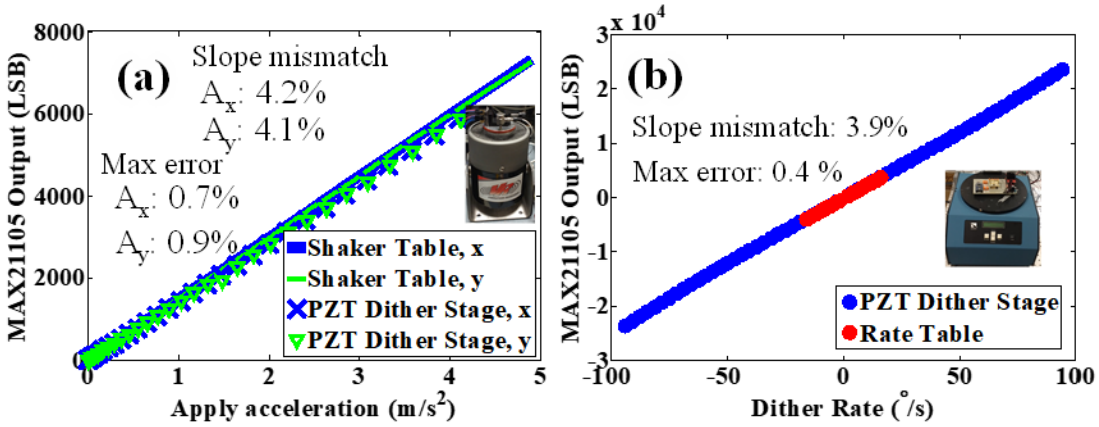

Figure 4.18: (a) The outputs of accelerometers calibrated by the dither stage are compared with the outputs calibrated by a Vibration Research VR2500 vibration controller and shaker. Inset shows a photograph of the experimental setup. (b) The outputs of the ω_z gyroscope calibrated by the dither stage are compared with the outputs calibrated by an Ideal Aerosmith 12700VS rate table with 1000 ppm rate repeatability. Inset shows a photograph of the experimental setup.

From (4.58), the scale factor can be extracted from the calibrated dither stage scale factor that was measured optically (Table 4.6), and the IMU output coefficient in Table 4.8 and Table 4.9. For example, the calibrated ω_z gyroscope scale factor from the dither stage is 0.662/164 (°/s)/LSB. The output from three accelerometers was measured, and then compared to the data read when excited by the dither stage and a Vibration Research VR2500 vibration controller and shaker as shown in Figure 4.18a. The output from 3-axis gyroscopes was also measured and compared between excitation from the

dither stage, and a rate table (Ideal Aerosmith 12700VS), as shown in Figure 4.18b. The calibrated IMU sensitivities (1/scale factor) from different methods are listed in Table 4.10. From this table, the gyroscope and accelerometer scale factors are within 3.3 % and 6.7 % of their datasheet specifications, respectively. Moreover, from Table 4.9, gyroscope cross-axis sensitivity calibrated by the dither stage is 2.4 %, which is within the IMU specification (± 5 %).

Table 4.10: Calibrated IMU sensitivity (1/scale factor).

	Datasheet	**Shaker/Rate Table**	**Dither stage**	**Unit**
a_x	15.0 ± 0.4	14.65 ± 0.05	14.03 ± 0.05	LSB/mg
a_y	15.0 ± 0.4	14.6 ± 0.1	14.0 ± 0.1	LSB/mg
ω_z	240 ± 6	238.7 ± 0.7	248 ± 2	LSB /(°/s)

4.3.4 Out-of-plane magnetic actuation

An out-of-plane angular rate was applied to the gyroscope to extract the x- and y-axis gyroscope scale factor. The frequency of the applied rate is fixed, and the angular rate magnitude is swept to avoid non-ideal gyroscope frequency dependence. Figure 4.19a shows time-dependent sinusoidal output from y-axis gyroscope at 11.25 deg/s (45 mA, 200 Hz). The angular rate amplitude can be extracted by fitting the output data to a sinusoidal model. An example of time-dependent output for the rate sweeping is shown in Figure 4.19b.

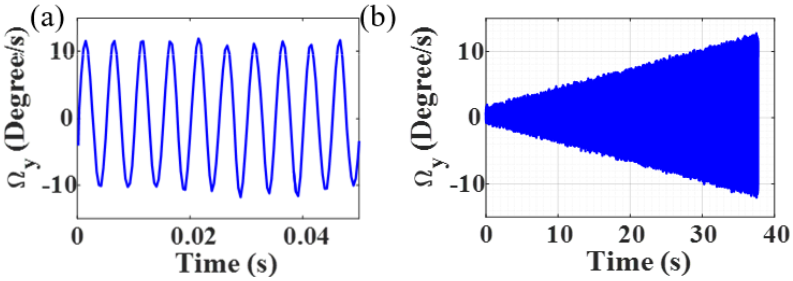

Figure 4.19: An example of a time-domain signal during calibration (a) sinusoidal angular rate output for 200 Hz and current 45 mA (b) angular rate output for the rate sweeping.

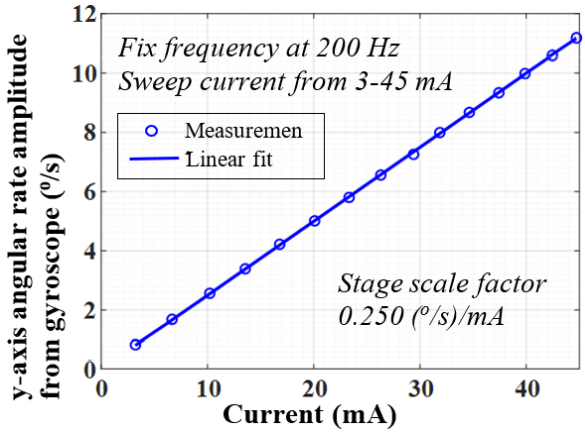

Figure 4.20: The extracted gyroscope angular rate amplitude for the current sweep in the Ω_y mode where the frequency is fixed at 200 Hz.

To demonstrate the magnetic stage operation, the angular rate of the y-axis gyroscope is extracted at 200 Hz, and the swept solenoid current 3-45 mA, as shown in Figure 4.20. The measured dither stage scale factor is 0.250 (°/s)/mA, as a function of current. Alternatively, the current amplitude can be fixed, and the frequency is swept from 5-200 Hz. The benefit of this method is reducing the demagnetization of the magnets. The gyroscope output for frequency sweeping with fixed solenoid current at 45 mA is shown in Figure 4.21. The dither stage scale factor is 5.57×10^{-2} (°/s)/Hz, as a function of frequency. The power consumption of the magnetic dither stage is $P = I^2R$, which is 33.5 mW/mdeg. The maximum dither angle obtained is 8.95 mdeg at 300 mW. Response in x- and z-direction is measured, as shown in Figure 4.22, where cross-axis sensitivity and the gyroscope misalignment are resulting in 5.9 % cross-axis sensitivity terms. The gyroscope cross-axis sensitivity 1 % exceeds the gyroscope specification. In the future, one can design the dither stage to have less cross-axis sensitivity or use signal processing with and without dithering to extract the cross-axis sensitivity to compensate when extracting the scale factor and bias.

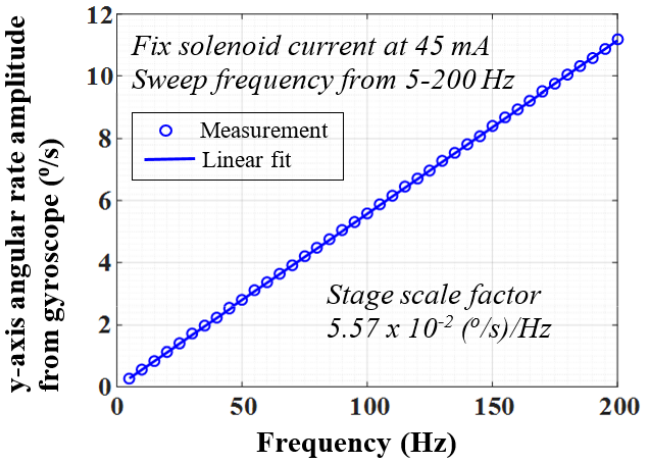

Figure 4.21: The extracted gyroscope angular rate amplitude for frequency sweep in the Ω_y mode where the solenoid current is fixed at 45 mA.

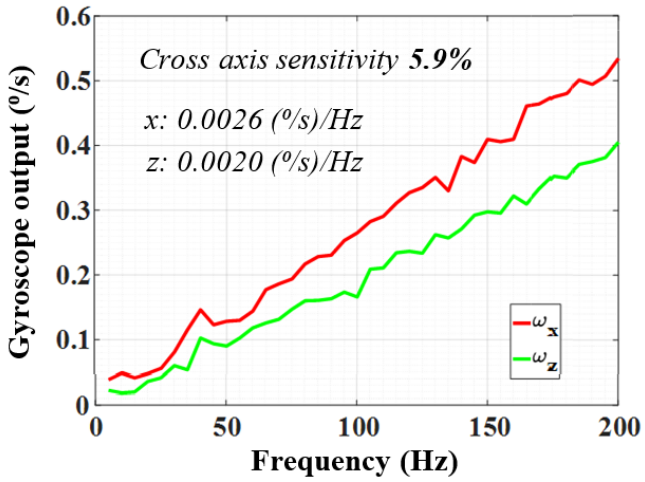

Figure 4.22: The x and z gyroscope outputs, when the dither stage is dithered around the y-axis, which represent misalignment and cross-axis sensitivity.

4.4 Discussion and Conclusions

A mechanical rate calibration dither stage with 3-axis dither capability is reported. A combination of piezoelectric and magnetic actuation provides in-plane and out-of-plane motion capabilities. The out-of-plane dither scale factor is 0.2495 (°/s)/mA as a function of current, or 0.0557 (°/s)/Hz as a function of frequency. The use of a miniature high bandwidth piezoelectric dither stage is demonstrated to calibrate in-plane acceleration and angular dither of a commercial IMU: MAX21105. The extracted

gyroscope and accelerometer scale factors are within 3.3 % and 6.7 % of their specifications provided by the manufacturer, showing the applicability of our multi-axis calibration system. The system is portable, self-contained, and can be used for *in situ* calibration and correction tool for any commercial MEMS IMU.

Further work is needed to decouple the micro dither stage motion aging and frequency accuracy of the dither stage to improve measurement accuracy and stability. Future work involves using new algorithms, coupled with Kalman filters, implemented in a microcontroller or an FPGA to compensate for drift in IMU parameters, while showing improvement in long term navigation accuracy.

CHAPTER 5

MECHANICAL ULF TRANSMITTERS: PERMANENT MAGNETS ACTUATED BY PIEZOELECTRIC DITHER STAGES

5.1 Introduction

Recent growing of interest in deployments of autonomous Internet-of-thing (IoT) platforms such as robots, unmanned aerial vehicles (UAVs), and unmanned underwater vehicles has significantly increased the demand for reliable wireless communication technologies [4], [155], [156]. Although the radio waves in the frequency range of megahertz to gigahertz is widely used for wireless communication, there remain numerous circumstances under which the high frequency radio wave based communication is unreliable [37], [157]–[159]. One reason is that the radio waves are highly absorptive in conductive media and highly reflective at interfaces between media with different impedances [35]–[38]. Therefore, reliable wireless communication cannot be achieved when media are conductive or reflective while operating in underwater or underground environments, or when used in communication between air and underwater interfaces.

An alternative technique that may be preferable under these circumstances is ultralow frequency (ULF: 300 Hz - 3 kHz) magnetic induction (MI). This method communicates by using nonradiative time-varying magnetic fields in the near-field region, where distances from the transmitters are closer than the ULF wavelength of 100-1000 km [35]–[37], [160]. In contrast to the high-frequency radio waves, ULF MI can transmit through seawater, soil, and building materials with small absorption [36], [161]. Communication is possible because of its relatively large skin depths, which increases when frequency is reduced [36]. Moreover, most materials are nonmagnetic with relative permittivity close to one; therefore, reflection and refraction between material interfaces are negligible [35]–[37], [160]. As a result, ULF MI can be used in

wireless communication underwater, underground, and in the air without relays at interfaces [35]–[37], [160]. ULF MI and other wireless communication technologies, including acoustic and radio waves, are compared in detail in 5.2.1.

Nonetheless, existing ULF transmitters are not suitable for IoT devices because of their large size, low efficiency, or because they contain many moving parts [36], [162]–[166]. For receivers, small-size, low-noise, and low-power ULF receivers suitable for IoT devices are available [161], [167]. Moreover, commercially available low-noise magnetometers can be used as ULF receivers, such that only transmitter development is necessary [38], [161], [168]. Available ULF transmitters include: 1) antenna facilities spanning over large areas, 2) loop antennas, and 3) mechanical antennas. First, in the 1970s, the US navy worked on Project Sanguine to develop far-field ULF transmitters for 1 - 1,000 Hz to communicate with submarines [163]. The project proposed an antenna facility spanning over an area as large as 100 km × 100 km. This large size prohibits integrating this type of antenna in IoT devices. The size of the antenna must be comparable to the wavelength to achieve high efficiency [169]. For example, radiation efficiency e_r of a short dipole antenna is approximately linearly proportional to the length [169]. The radiation efficiency e_r is given by

$$e_r = \frac{R_r}{R_r+R_o} \approx \frac{R_r}{R_o} \approx \frac{120\pi^3 a}{\lambda}\sqrt{\frac{2\sigma}{\omega\mu}}\left(\frac{L}{\lambda}\right), \tag{5.1}$$

where R_r is the radiation resistance, R_o is the antenna ohmic resistance, a is the antenna wire radius, λ is the wavelength, ω is the angular frequency, σ is the antenna wire conductivity, μ is antenna wire permeability, and L is the antenna length. [169]. Second, loop antennas have been used as ULF transmitters for near-field MI communication [36], [162]. Nevertheless, these loop antennas are large (0.5 - 6 m) for IoT applications because of the high inductance necessary for achieving low resonance frequency in the ULF range [36], [162]. The resonance frequency of the loop antenna is given by

$$f = \frac{1}{2\pi\sqrt{L_l C_l}}, \tag{5.2}$$

where L_l is the loop antenna inductance, and C_l is the loop antenna capacitance. Moreover, loop antennas constantly dissipate energy due to internal resistance, even when generating a static field [161]. The magnetic dipole moment m of the loop antenna is given by

$$m = NIA, \tag{5.3}$$

where N is the number of turns, I is the current, and A is the area of the loop antenna. Power dissipation P in the loop antenna is given by

$$P = I^2 R, \tag{5.4}$$

where R is the resistance of the loop antenna. A 3,000 cm^3 neodymium permanent magnet generates a static magnetic field without dissipating any energy, while a loop antenna of the same size requires 100 kW to generate the same magnetic field [161].

The third method is to use small-size and low-power mechanical ULF transmitters [161]. In this method, permanent dipoles such as electrets and magnets are mechanically actuated in the ULF range to generate a time-varying electric or magnetic field. The advantage of using mechanical ULF transmitters over the other ULF transmitters discussed earlier is that the permanent electric and magnetic dipoles do not dissipate energy while generating a static field [161]. As a result, the mechanical ULF antennas are more energy-efficient than the aforementioned antennas. Moreover, achieving resonance frequencies in the ULF range for mechanical systems is possible in small dimensions. Many articles have proposed theoretically calculated designs for using a mechanically rotating magnetic or electric dipole as a ULF transmitter [161], [170]–[173]. The process of using a high-speed motor to spin a permanent magnet as a mechanical ULF transmitter is shown in [164], [165], [174]; however, these devices

may suffer from bearing wear in the long term. A prototype array of oscillating permanent magnets driven by solenoids on machined aluminum structures is shown as a ULF antenna [166]. This device does not suffer from bearing wear but may be too heavy and large for IoT applications. In the next higher frequency band (VLF), prototypes using the oscillation of piezoelectric materials are shown [175], [176]. Using the VLF band causes higher absorption in conductive media such as seawater. In one prototype, oscillations of a piezoelectric PZT sheet driven by a magnetostrictive Metglas sheet is used as a VLF transmitter at 30 kHz [175]. In another prototype, a piezoelectric lithium niobate crystal resonating in elongation mode is used as a VLF transmitter at 35.5 kHz [176]. Nevertheless, this prototype uses a Czochralski-growth lithium niobate crystal rod and operates with a voltage as high as 125 kV causing air breakdown corona discharge.

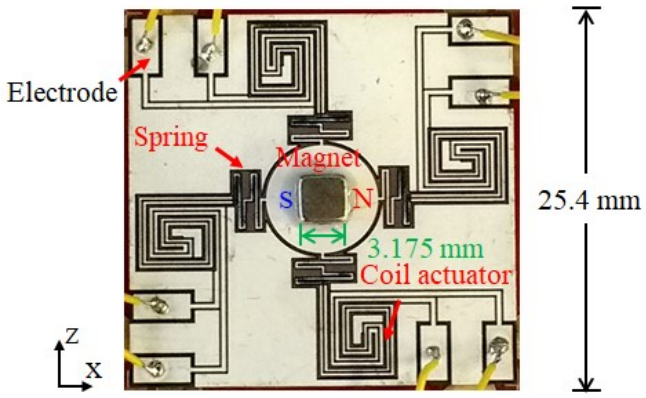

Figure 5.1: A top view photograph of the ULF transmitter shows a permanent magnet mounting on the piezoelectric dither stage. The platform is actuated by four coil actuators to generate a ULF signal.

In this chapter, small (2.4 cm^3) and low-power (1.8 µW) mechanical ULF transmitters (Figure 5.1) are presented. This ULF transmitter can communicate up to 20 m when using commercially available receivers. The ULF transmitter uses a piezoelectric lead zirconate titanate (PZT) dither stage to drive a permanent magnet in

an angular oscillation motion. In contrast to existing mechanical ULF transmitters, this research focuses on reducing the size, improving the energy figure of merit, forgoing the need for motors or bearings, forgoing the need for impedance matching, and minimizing voltage requirement. Piezoelectric transduction allows for designing small and low-power actuators without motors or bearings. The dither stage has a high impedance of 34.6 kΩ; therefore, impedance matching circuits and special driver circuits are not required. In contrast, actuating permanent magnets with a magnetic field from solenoids requires impedance matching or special driver circuits to avoid significant power loss. At low frequency in the ULF range, the capacitance required for impedance matching tends to be impractically large. The ULF transmitter application examples include 1) linearly cascaded IoT devices for localization and communication in an underground mine (Figure 5.2a) and 2) distributed IoT devices capable of communicating with UAVs for studying fish behavior (Figure 5.2b).

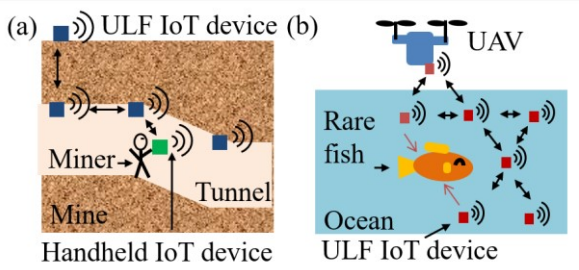

Figure 5.2: Examples of cascaded and distributed devices. (a) Linearly cascaded IoT devices with ULF communication for mine localization and communication. (b) Distributed IoT devices with ULF communication for monitoring fish behavior.

In the following sections of this chapter (5.2), the ULF transmitter is discussed in further detail. First, the ULF MI wireless communication technology is compared with other technologies in 5.2.1 to show that ULF MI is suitable for communication in underwater, underground, and air environments. Next, the ULF transmitter design and fabrication are presented in 5.2.2, followed by a modeling of the ULF transmitter in different aspects in 5.2.3-5.2.6. The generated time-varying magnetic field is modeled

in 5.2.3 – this is an important metric that can be used to quantify the distance and direction over which the ULF transmitter can communicate. The solid mechanic model is investigated by finite element analysis (FEA) in 5.2.4 to predict the maximum generated magnetic field. From the device model in 5.2.3 and 5.2.4, its communication range and power consumption are calculated in 5.2.5, and the data bandwidth is calculated in 5.2.6. The experimental results of the fabricated stage are presented in 5.3.

5.2 Materials and Methods

The ULF transmitter consists of a permanent magnet mounted on a laser-micromachining piezoelectric dither stage, as shown in Figure 5.3. When actuating the dither stage, the magnet oscillates with a small-angle amplitude at the mechanical resonance frequency, which is designed to be in the ULF range. The oscillating magnet generates a time-varying magnetic field, which can be detected by magnetometers or ULF receivers.

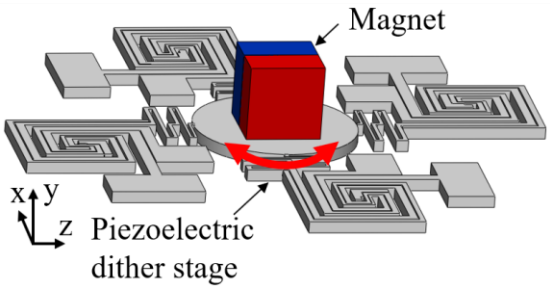

Figure 5.3: The mechanical ULF transmitter consists of a permanent magnet mounted on a piezoelectric dither stage.

The dither stage is designed for gyroscope calibration, as previously explained in Chapter 4. Because the ULF MI is suitable for communication in underwater, underground, and air environments, as discussed in 5.2.1, the dither stage is integrated with a permanent magnet to achieve a low-power and small ULF transmitter, as explained in 5.2.2. The dither stage actuates the permanent magnet, which can be modeled as an oscillating magnetic dipole generating a time-varying magnetic field for

ULF MI communication, as explained in 5.2.3. From the calculation in 5.2.3, the generated ULF magnetic field is proportional to the dither angle and decay inversely proportional to the cube of the distance. Hence, the maximum communication range can be increased by driving the dither stage at a large angle. The dither stage is investigated by finite element analysis (FEA) in 5.2.4 to predict the maximum dither angle before irreversible deformation. From the analysis in 5.2.3 and 5.2.4, the maximum communication range and power consumption are calculated in 5.2.5, and the data bandwidth is calculated in 5.2.6 to investigate whether the ULF transmitter is suitable for IoT applications.

5.2.1 Comparison of wireless communication technologies

Table 5.1: Comparison of wireless communication technologies for air, underwater, and underground environments [35]–[38].

Technologies / **Characteristic**	**EM**	**Acoustic**	**MI in MHz range**	**MI in ULF range**	**MI in ULF range with mechanical antenna (This work)**
Air	**Common technique**	Disturb humans and animals	**Suitable**	**Suitable**	**Suitable**
Underground	High path loss	High reflection	High path loss in conductive media	**Suitable**	**Suitable**
Underwater	High path loss	**Common technique**	High path loss in seawater	**Suitable**	**Suitable**
Air/Underground /Underwater interface	High reflection	High reflection	**Suitable**	**Suitable**	**Suitable**
Antenna size	**Small**	**Small**	**Small**	Large	**Small**

The ULF MI wireless communication technology is compared with other technologies to show that ULF MI is suitable for communication in underwater,

underground, and air environments, as shown in Table 5.1. Electromagnetic (EM) waves such as radio and microwave are one of the most common methods for wireless communication through air. However, EM waves can be reflected and absorbed by conductive media such as seawater. As a result, underwater and underground EM communication suffers from high path loss and unreliable channel conditions [35]–[38]. Using acoustic waves for wireless communication underwater is common, but acoustic communication suffers from high reflection underground because of different media [35], [37]. Acoustic waves can suffer from refraction in deep water, reflections in shallow water, and has a large propagation delay [36].

Magnetic induction (MI) can be used as a wireless communication method to send information through a time-varying magnetic field. Unlike communication using EM waves and acoustic waves, MI is more suitable for wireless communication underground and underwater because of low refraction and low reflection. The reason for this is that most underwater and underground media such as concrete, soil, and water are non-magnetic materials and have relative permeabilities close to one [35]–[37], [160]. Many research groups have proposed to use MI in the high-frequency range (125 kHz - 10 MHz) for underground communication and localization [35], [37], [177]. However, MI communication can suffer from high path loss due to induced eddy currents in conductive media such as seawater, metal structure, and wet soil [36].

Operating MI at low frequencies can reduce path loss because attenuation due to eddy currents increases with the frequency [36]. Nevertheless, reducing the frequency too much decreases the communication bandwidth beyond practical limits. MI communication in the range 300 Hz - 3 kHz is one of the most suitable frequency ranges for underwater and underground IoT due to its low absorption and acceptable bandwidth [36], [37], [161]. Even in conductive seawater, the path loss is estimated to be 25 dB at 10 m, which is much lower than the path loss of 7,000 dB at 10 m for 400 MHz EM

communication [36]. This frequency range (300 Hz - 3 kHz) is designated as ultralow frequency (ULF) by the International Telecommunication Union (ITU) and is called extremely low frequency (ELF) or very low frequency (VLF) in some literature [161], [163], [167]. Operating MI in ULF does not only allow wireless communication through water and underground, but ULF MI may enable direct communication between air and underwater and underground interface because of low reflectivity and absorption [36], [161]. The current approach relies on using relays at the interface to communicate by EM waves in the air and acoustic waves underwater [178], [179]. With ULF MI wireless communication, UAVs or handheld devices can directly communicate with underwater and underground IoT devices. Moreover, most existing wireless communication systems operate in VHF, HF, and medium wave bands; therefore, interference from existing systems is negligible [36]. Hence, MI in ULF is a promising candidate for wireless communication with underground and underwater IoT devices.

5.2.2 Design and fabrication

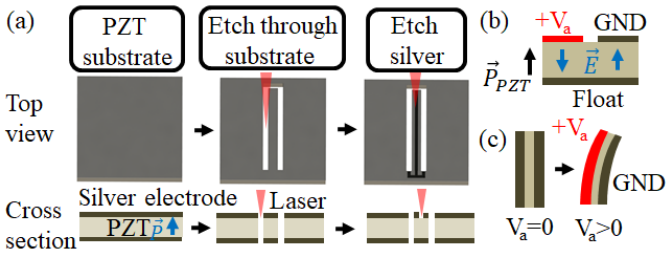

Figure 5.4: (a) A laser-micromachining process on bulk PZT plates. (b) The cross-sectional view of a PZT lateral bimorph actuator shows the output electrode and ground electrode on top and a floating electrode on the bottom. (c) The top view of a PZT lateral bimorph shows that the bimorph bends in-plane after applying voltage.

The ULF transmitter consists of a permanent magnet actuated by a piezoelectric dither stage that is fabricated by a laser-micromachining process on a bulk lead zirconate titanate (PZT) plate (Figure 5.4a) [60]. The substrate is 25.4 mm × 25.4 mm × 0.5 mm APC 841 bulk PZT plate with silver on the top and bottom. The process selectively

scans a UV laser (LPKF Protolaser U) to remove material from the substrate. Electrodes are formed by removing the silver layer, and mechanical structures are formed by laser etching through the substrate. The cross-sectional view and top view of the lateral PZT bimorph is shown in Figure 5.4b and Figure 5.4c, respectively. When applying a voltage V_a on the input electrode, an electric field is formed in opposite directions under the two top electrodes, as shown in Figure 5.4b [60]. The piezoelectric coefficient d_{31} causes in-plane expansion and contraction, which leads to the cantilever bending, as shown in Figure 5.4c. As a result, the bimorph can be used as an in-plane actuator by applying voltage V_a.

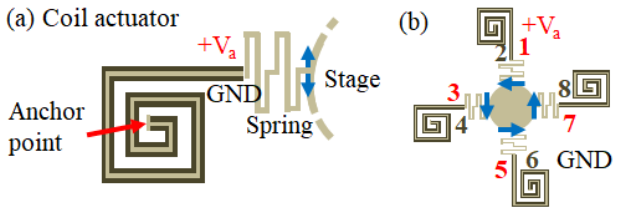

Figure 5.5: (a) A coil actuator consists of cascading lateral bimorph and is connected to the circular platform via a spring. (b) An angular dither stage consists of 4 coil actuators.

A series of in-plane bimorph actuators are cascaded into a coil actuator (Figure 5.5a) to amplify displacement while keeping the size compact. The coil actuator is connected to a circular platform via a spring to increase displacement and reduce spurious modes. Four coil actuators are connected to a circular platform such that the stage is angularly dithered (Figure 5.5b) when AC voltage $V_a = V_0 \sin(\omega t)$ is applied [141]. The platform is etched by laser to create a slot for aligning a magnet. A 3.175 mm × 3.175 mm × 3.175 mm N38SH neodymium magnet is attached to the stage with cyanoacrylate adhesive. The dither stage is driven at the mechanical resonance frequency to reduce the required voltage to as low as 0.5 V. Alternatively, in applications where power consumption is not critical such as gyroscope calibration, this

dither stage can be driven at high voltage (100-200V) at frequencies much lower than the resonance frequency, as explained in Chapter 4 [61], [62], [88]. Moreover, the in-plane bimorph can be used as zero-power sensors such as accelerometers, magnetometers, and microphones, as explained in Chapter 2 [52], [53], [59]. This laser-micromachining process potentially allows the integration of zero-power sensors and ULF transmitter in one PZT substrate.

5.2.3 Device ULF MI modeling

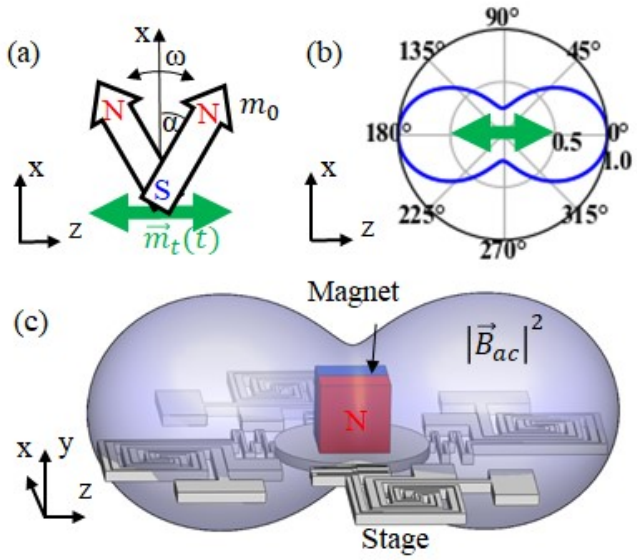

Figure 5.6: (a) A permanent magnet pointing in the x-direction is oscillating at a small angle in the xz plane. (b) Time-varying part of the magnetic dipole moment and magnetic field amplitude (c) Relative magnitude of magnetic induction energy as a function of direction.

The time-varying magnetic field generated by the ULF transmitter is analyzed to calculate the maximum communication distance. Most ULF MI systems operate over a short range (r < 300 m) while the wavelength λ is much longer (100-1000 km) [36], [37], [166]. The system can be modeled as a non-propagating near-field magnetic induction (MI)[36], [37], [166][36], [37], [166][36], [37], [166][36], [37], [166][36], [37], [166]. The permanent magnet size (L) is also much smaller than the wavelength.

Hence, the magnet can be considered as a dipole with a total magnetic dipole moment of m_0. If the magnet dipole moment points in the $\hat{x}$ direction and oscillates with a small angle at a frequency $\omega/2\pi$ in the x-z plane as shown in Figure 5.6a, the angle as a function of time is

$$\alpha(t) = \alpha_0 \cos(\omega t), \tag{5.5}$$

where α_0 is the dither angle amplitude.

The magnetic dipole moment as a function of time t is

$$\vec{m}(t) = m_0(\cos[\alpha(t)]\,\hat{x} + \sin[\alpha(t)]\,\hat{z}), \tag{5.6}$$

where m_0 is the magnetic dipole moment. If the oscillation angle amplitude is small ($\alpha_0 \ll 1$), the time-varying magnetic dipole moment can be approximated as

$$\vec{m}_t(t) \approx m_0\alpha_0 \cos(\omega t)\,\hat{z}, \tag{5.7}$$

which is an oscillating magnetic dipole with magnitude $m_{t0} = m_0\alpha_0$ pointing in the $\hat{z}$ direction, as shown in Figure 5.6a. Using approximations $L \ll r$, $L \ll \lambda$, and without considering loss from eddy currents, the vector potential $\vec{A}$ for an oscillating dipole can be written in the spherical coordinate (r, θ, ϕ) as

$$\vec{A}(r,\theta,t) = \frac{\mu_0\mu_r m_0\alpha_0}{4\pi}\frac{sin(\theta)}{r}\left[\frac{1}{r}\cos(\omega t') - \frac{\omega}{c}\sin(\omega t')\right]\hat{\phi}, \tag{5.8}$$

where μ_r is the relative permeability of the medium, and $t' = t - r/c$ is the retarded time [142]. ULF receivers tend to use magnetic field sensing because of its lower noise floor [161]. The magnetic field can be obtained from $\vec{B} = \nabla \times \vec{A}$ as

$$\vec{B}(r,\theta,t) = \frac{\mu_0 m_0\alpha_0}{4\pi}\left\{\frac{2\,cos(\theta)}{r^2}\left[\frac{1}{r}cos(\omega t') - \frac{\omega}{c}sin(\omega t')\right]\hat{r}\right.$$
$$\left. - \frac{sin(\theta)}{r}\left[\left(\frac{\omega^2}{c^2} - \frac{1}{r^2}\right)cos(\omega t') + \frac{\omega}{rc}sin(\omega t')\right]\hat{\theta}\right\}. \tag{5.9}$$

Within the typical communication range (r), which is much less than the wavelength (λ ≈ 100-1000 km), the magnetic field can be approximated as

$$\vec{B}(r,\theta,t) = \frac{\mu_0}{4\pi}\frac{m_0\,\alpha_0}{r^3}cos(\omega t') \times \left[2\,cos(\theta)\,\hat{r} + sin(\theta)\,\hat{\theta}\right]. \tag{5.10}$$

The magnetic field amplitude is dependent on the angle θ, as shown in Figure 5.6b, where the maximum amplitude is in the z-direction of the magnet pointing toward the x-axis. The amplitude of the magnetic field in the maximum direction ($\theta = 0, 180°$) is

$$\vec{B}_{max} = \frac{\mu_0}{4\pi}\frac{2m_0\,\alpha_0}{r^3}\hat{r}. \tag{5.11}$$

After estimating the maximum dither angle α_0 in 5.2.4, the magnetic field $\vec{B}_{max}$ is plotted, and the maximum communication distance is calculated in 5.2.5.

5.2.4 Device mechanical simulation

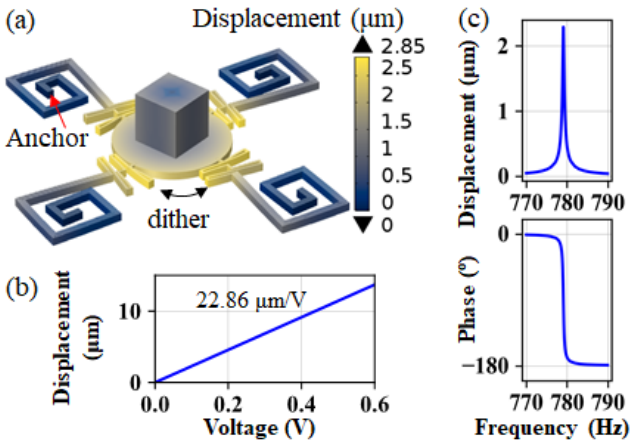

Figure 5.7: The ULF transmitter is simulated to extract displacement. (a) The mechanical resonance mode shape of the angular dither mode. The color shows total displacement. (b) Circular platform edge displacement at resonance as a function of voltage amplitude. (c) Frequency dependence of the circular platform edge displacement.

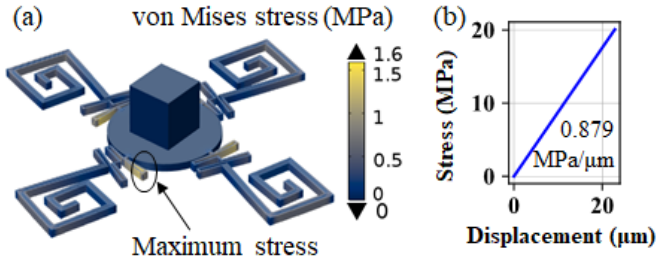

Figure 5.8: The ULF transmitter is simulated for stress to investigate maximum displacement without damaging the stage. (a) Simulated von Mises stress distribution shows maximum stress in the springs (b) Maximum von Mises stress versus platform edge displacement.

The ULF transmitter is investigated by a finite element analysis (FEA) to model mechanical resonance frequency and stress distribution. The stress is used to calculate the maximum dither angle before the dither stage is deformed irreversibly. Some parameters of the piezoelectric stage, such as piezoelectric force and spring constant, were analytically modeled [141]. Due to complex geometry, the mechanical model of the dither stage with a magnet is studied by COMSOL finite element simulation software. Damping is modeled as a lumped isotropic loss with a volume damping coefficient $1.75 \times 10^4\ \mathrm{N \cdot m^{-4} \cdot s}$. From an eigenfrequency study, the resonance frequency of the angular dither mode is 779 Hz with a mode shape shown in Figure 5.7a. At resonance, the circular platform edge displacement is 22.86 μm/V, as shown in Figure 5.7b. The circular platform radius is 3.7 mm, so the angular dither amplitude is α_0= 6.2 mrad/V. The frequency dependence of edge displacement is shown in Figure 5.7c. Next, the maximum stress is investigated to ensure that the dither stage does not operate close to yield strength to prevent damage. The von Mises stress distribution is shown in Figure 5.8a. The maximum von Mises stress is located at the corner of the spring. The stress as a function of circular platform edge displacement is shown in Figure 5.8b. Bulk PZT yield strength varies on PZT type, stress direction, and testing method [180], [181]. From various conditions, the lowest reported yield strength is 33

MPa [180]. This stress corresponds to a platform edge displacement of 37.5 μm, dither amplitude of 10.1 mrad, and an applied voltage of 1.64 V. In the experiments explained in 5.3, the applied voltage is below 0.5 V in order to operate the ULF transmitter below the yield point where permanent deformation occurs.

5.2.5 Communication range and power consumption

Communication range and power consumption are analyzed in order to evaluate the ULF transmitter with previous research. From the analysis in 5.2.3, the maximum communication range achieved by the ULF antenna can be calculated from the maximum magnetic field versus distance in (5.11). The ULF antenna power consumption is calculated from the dither stage impedance, measured later in 5.3. An operation point is chosen at the edge displacement of 5 μm, where the maximum stress is much lower than yield strength. The magnetic dipole moment can be estimated from N38SH specification, which shows residual flux density $B_r = 1.21$ T [182]. The magnetic dipole moment is

$$m_0 = B_r V/\mu_0, \tag{5.12}$$

where μ_0 is the permeability of free space and V is the magnet volume. From (5.12), the magnetic dipole moment of the permanent magnet in this prototype is 0.031 A·m^2. Other design parameters are shown in Table 5.2.

Table 5.2: Design parameters.

Description	Parameter	Value
Magnetic dipole moment	m_0	0.031 A·m^2
Stage dither angle amplitude	α_0	1.3 mrad
Mechanical resonance frequency	f_R	779 Hz

From (5.11), the magnetic field amplitude is plotted in Figure 5.9. Maximum communication distance can be calculated from the receiver noise floor. Commercially

available state-of-the-art ULF receivers have a noise floor of 1 fT/Hz$^{1/2}$ with a minimum detectable sensitivity as low as 1 fT at 1-Hz bandwidth [161], [167], [168]. For commercial receivers, this ULF transmitter has a maximum communication distance of 20 m with 1 Hz bandwidth.

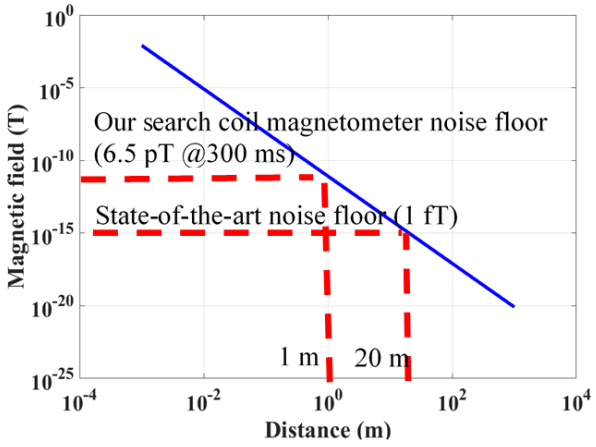

Figure 5.9: The plot shows magnetic field transmitted by the ULF transmitter prototype versus distance. Commercial receivers can receive the signal from up to 20 m.

To benchmark the system, energy and power dissipation needs to be quantified. In this ULF MI transmitter, energy stored in the mechanical oscillation is given by

$$P_{mechanical} = \frac{1}{2}\frac{k_\alpha \alpha_0^2}{Q}\omega = \frac{1}{2}\frac{I\alpha_0^2\omega^3}{Q}, \tag{5.13}$$

where k_α is the torsional spring constant, Q is the quality factor, and I is the moment of inertia of the ULF transmitter. The total power dissipated in the system can be calculated from active power given by

$$P_{electrical,active} = \frac{1}{2}\frac{V_{RMS}^2}{|Z_{Stage}|^2} Real(Z_{Stage}), \tag{5.14}$$

where Z_{Stage} is the electrical impedance of the dither stage, and V_{RMS} is the root-mean-square of the stage drive voltage. Nevertheless, impractically large inductance is needed

to cancel out the imaginary impedance of the ULF transmitter. As a result, the total energy dissipated in the system is

$$P_{electrical,complex} = \frac{1}{2}\frac{V_{RMS}^2}{Z_{stage}}. \tag{5.15}$$

MI communicates through non-radiative magnetic fields because energy coupling through an electric field is negligible [142]. The majority of energy in the magnetic field in (5.10) is not radiated to infinity. Hence, transfer energy cannot be modeled unless the receiver is modeled together [35], [36]. Different MI transmitters can be compared using the maximum magnetic field amplitude in (5.11), which depends only on equivalent oscillating dipole amplitude $m_{t0} = m_0\alpha_0$, as shown in (5.7). In this chapter, the energy figure of merit is defined as a ratio of equivalent oscillating dipole moment versus energy dissipated as

$$\text{Energy figure of merit} = \frac{m_{t0}}{P_{electrical,complex}} = m_0\alpha_0\frac{2Z_{stage}^2}{V_{RMS}^2}. \tag{5.16}$$

The energy figure of merit from different systems in literature are compared later in 5.4 (Table 5.4).

5.2.6 Modulation and bandwidth

The data bandwidth is calculated to quantify the maximum data rate achieved by the ULF transmitter. The transmitted ULF signal can be modulated by tuning resonance frequency, adding a tunable magnetic field attenuator, or modulating drive voltage [36], [164], [176], [183]. Tuning resonance frequency and adding a tunable magnetic field attenuator allow modulation bandwidths higher than the mechanical bandwidth, with the cost of system complexity and power consumption [164], [176]. Directly modulating drive voltage does not require additional mechanical hardware but leads to the bandwidth becoming limited by the mechanical response. For this ULF

transmitter, the mechanical bandwidth is 2.4 Hz, which is enough for many IoT applications, so the ULF transmitter is modulated by directly modulating drive voltage [157]. The drive voltage can be analog-modulated using AM and FM, or digital-modulated using OOK and FSK. Higher bit rates can be achieved by bandwidth-efficient modulation techniques such as minimum shift keying (MSK) and quadrature amplitude modulation (16-QAM) [36]. For OOK, if on-off durations are approximately equal, power consumption can be estimated to reduce by half of (5.14) and (5.15). Maximum bandwidth can be obtained from Shannon-Hartley theorem given by [184]

$$C = b \log_2(1 + SNR) \text{ bit/s.} \tag{5.17}$$

Digital bandwidth C is in the unit of bits/s, b is the analog bandwidth, and SNR is the average signal to noise power ratio. Even in the worst case with SNR of 1, this transmitter is theorized to be able to communicate at 2.4 bps. The bandwidth of this ULF transmitter is compared with others in 5.4.

5.3 Results

After the ULF transmitter was designed and fabricated, as discussed in the previous section, the prototype was characterized, and ULF transmission was demonstrated. The ULF transmitter was characterized in 5.3.1 to measure parameters including a dither angle α_0, input impedance Z, and a magnetic moment m_0. These parameters are used to calculate the maximum communication range and power consumption. The ULF transmissions at different distances with AM and OOK modulations were shown in 5.3.2 to demonstrate the ULF transmitter capability. The ULF magnetic field as a function of distance is measured and compared with predicted value to confirm the model previously calculated in 5.2.3. Power consumption is calculated in 5.3.3 to compare the ULF transmitter with others in 5.4.

5.3.1 Device characterization

The ULF transmitter is characterized by measuring a dither angle α_0, input impedance *Z*, and a magnetic moment m_0 to calculate the maximum communication range and power consumption. The dither angle α_0 is measured by the stroboscopic method (Polytec MSA400 microsystem analyzer), as shown in Figure 5.10. A microscope captures images at the circular platform edge (Figure 5.10a), and the platform edge displacement is measured by tracking image position. The ULF transmitter is driven by a sine wave with a fixed amplitude of 0.1 V, and the frequency is swept around the resonance frequency. The displacement amplitude and phase are plotted in Figure 5.10b, which shows a resonance frequency of 893 Hz, a quality factor of 380, and a bandwidth of 2.4 Hz. The measured resonance frequency matches the simulation results within 12%, which is potentially caused by process variations and magnet position.

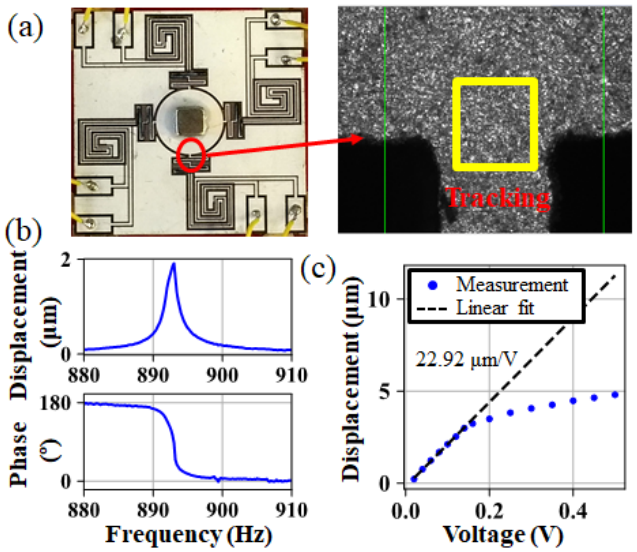

Figure 5.10: The dither stage is calibrated using the stroboscopic technique. (a) The microscope photograph is tracked to measure the displacement. (b) Displacement versus frequency is plotted to find the resonance frequency. (c) The platform edge displacement amplitude is plotted as a function of voltage amplitude.

While fixing the frequency at resonance, the displacement is measured at different voltages, as shown in Figure 5.10c. The displacement at low voltage is fitted to a linear model to measure the ratio of the displacement and the voltage. The measured ratio is 22.92 μm/V, which matches the simulation within 0.3%. When the ULF transmitter drive voltage is 0.1 Vp, the displacement is 2.12 μm, which corresponds to the dither angle α_0 of 0.57 mrad. When the drive voltage is higher than 0.14 V, the dither stage starts to operate in the nonlinear regime, which means the displacement is smaller than expected. When driving the dither stage at 0.5 Vp, the displacement is 4.81 μm, which corresponds to the dither angle α_0 of 1.3 mrad. The dither angle α_0 is used to calculate the predicted ULF magnetic field in 5.3.2.

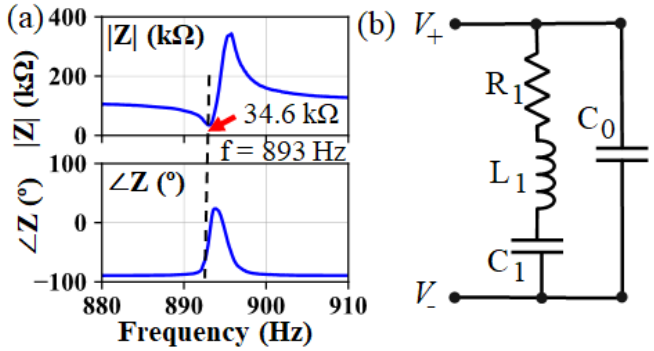

Figure 5.11: (a) The impedance of the ULF transmitter is measured by a HP4194 impedance analyzer. (b) A Butterworth-van Dyke equivalent circuit diagram.

The impedance of the ULF transmitter is measured by an HP4194A impedance analyzer to calculate ULF transmitter power consumption. The measured impedance magnitude and phase are shown in Figure 5.11a. The resonance frequency can be found at the location of the local minimum at 893 Hz. This frequency matches the resonance frequency measured by the stroboscopic technique. At resonance, the impedance magnitude is 34.6 kΩ and the phase of -31 degrees. The impedance is fitted to the Butterworth-van Dyke model (Figure 5.11b) to find an equivalent circuit as a piezoelectric transducer [18]. The fitted parameters are C_0 = 1.62 nF, C_1 = 8.36 pF, L_1

= 3.80 kH, and R_1 = 39 kΩ. The impedance is later used for calculating power consumption, as described in (5.14) and (5.15).

The magnetic dipole moment (m_0) of the magnet is experimentally quantified by measuring the magnetic field ($|\vec{B}|$) as a function of distance d, as shown in Figure 5.12a. The magnetic field was measured by a Texas Instruments DRV425 fluxgate magnetometer. The magnitude of the magnetic field from a dipole along the dipole direction is given by $B = \mu_0 m_0 / 2\pi d^3$. The magnetic moment is extracted by plotting $x = \mu_0 / 2\pi d^3$ and $y = B$, as shown in Figure 5.12b, and the slope is the measured magnetic moment $m_0 = 0.028\ \text{A} \cdot \text{m}^2$. The dither angle α_0, input impedance Z, and the magnetic moment m_0 measured in this section are used to calculate the maximum communication range and power consumption in 5.2.5 and 5.3.3, respectively.

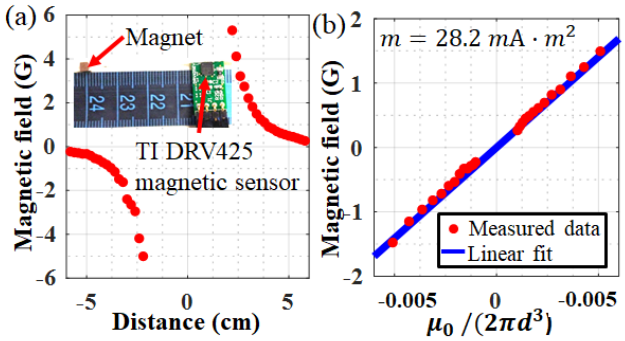

Figure 5.12: Magnetic dipole moment calibration. (a) Magnetic field as a function of distance. (b) The magnetic field is plotted versus $\mu_0/(2\pi d^3)$ to extract the magnetic dipole moment from the slope.

5.3.2 ULF MI communication

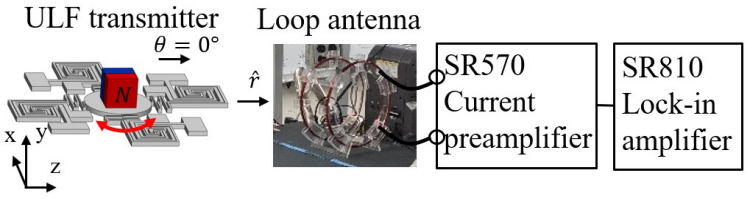

Figure 5.13: The ULF MI communication is demonstrated by using a loop antenna and amplifiers to receive a signal from the ULF transmitter.

ULF transmission at different distances with AM and OOK modulations is demonstrated by a measurement diagram shown in Figure 5.13. The ULF transmitter is driven at the mechanical resonance frequency of 893 Hz, as measured in 5.3.1. The drive voltage is kept below 0.5 V, which corresponds to a stress level far below the yield strength where irreversible deformation occurs, as discussed in 5.2.4. The loop antenna (100 turns of 27 AWG copper magnetic wire) is placed at the maximum transmission direction ($\theta = 0, 180°$), as described in (5.10). The loop antenna is placed in the $\hat{r}$ direction to maximize sensitivity, as described by (5.11). The magnetic field can be measured by voltage or current, but the current sensing has a lower noise floor at low frequency [168]. The output of the loop antenna is amplified by a Stanford Research Systems SR570 low noise current preamplifier and an SR810 lock-in amplifier. The total sensitivity of the receiver is 11.6 GV/T with the RMS noise floor of 6.5 pT, and the bandwidth of 0.5 Hz. The dither angle is measured by the Polytec MSA400 micro system analyzer, as explained in 5.3.1, at the same time as the ULF transmission measurement. The measured magnetic field amplitude as a function of distance is compared with the calculated magnetic field from (5.11) in Figure 5.14.

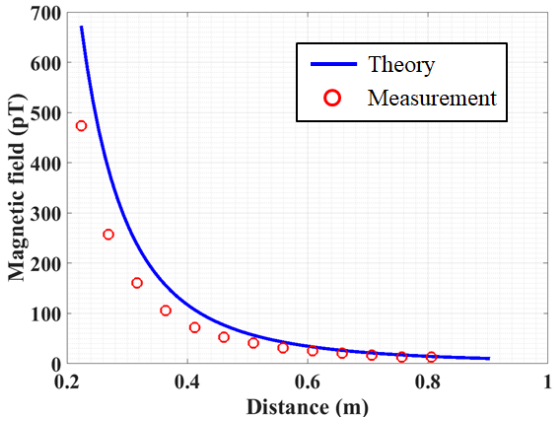

Figure 5.14: The magnetic field generated by the ULF transmitter with a frequency of 893 Hz and a drive voltage of 0.5 V is compared with the theoretical calculation.

ULF communication by AM and OOK is demonstrated by modulating the drive voltage. For AM, the drive voltage of 0.5 V_p is modulated with a modulation depth of 100%. The drive voltage and measured magnetic field at 0.5 m are shown in Figure 5.15. For digital modulation, an on-off keying (OOK) is shown in Figure 5.16. The bandwidth is limited by the receiver (0.5 Hz) rather than the transmitter (2.4 Hz). The bandwidth of the ULF transmitter is compared with other designs in 5.4.

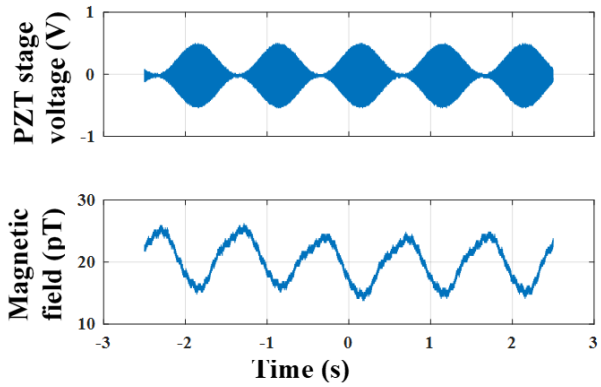

Figure 5.15: The AM modulated drive voltage of the ULF transmitter is compared with the measured magnetic field.

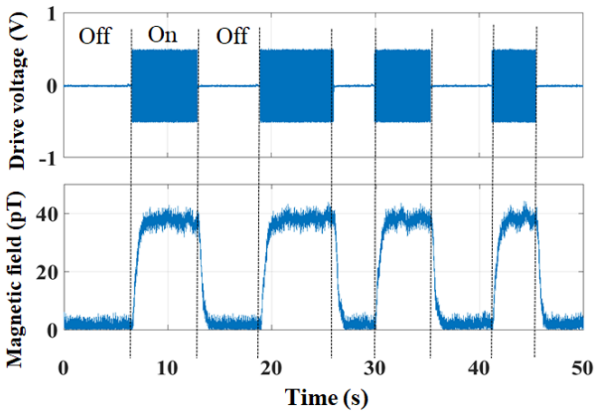

Figure 5.16: The OOK modulated drive voltage of the ULF transmitter is compared with the measured magnetic field.

5.3.3 Power consumption

Power consumption is calculated in order to compare the ULF transmitter with existing designs. Power consumption without modulation can be calculated from drive

voltage amplitude and measured impedance, as described in (5.14) and (5.15). In the linear operation with voltage 0.1 V, the active power is 124 nW, and complex power is 145 μW. For 0.5 V amplitude (nonlinear operation), active power is 3.1 μW, and complex power is 3.6 μW. Although impedance matching is not practical because of the large inductance required, power loss without impedance matching increases only by 14%. On the other hand, ULF loop antenna transmitter impedance is dominated by inductance, so impedance matching is critical [176]. For OOK modulation with a 50% duty cycle when the on and off durations are approximately 50%, power consumption is reduced by half. The power consumption and energy figure of merit of the ULF transmitter, previously defined in (5.16), are shown in Table 5.3. Power consumption is compared with other previous works in the next section.

Table 5.3: Power consumption for different settings.

Settings	Complex power consumption	Complex power consumption with OOK	Dipole equivalent	Efficiency figure of merit
Linear regime (0.1V)	145 nW	72 nW	16 μA·m^2	220 A·m^2/W
Nonlinear regime (0.5V)	3.6 μW	1.8 μW	36 μA·m^2	20 A·m^2/W

5.4 Discussions and conclusion

Specification comparisons of the ULF transmitter with those in existing literature are shown in Table 5.4 [36], [162], [164]. This transmitter consumes less power (up to 10^8 times) and is dimensionally smaller (up to 240 times in the longest linear dimension) than previously reported loop antenna or mechanical ULF transmitters. In linear operation, the efficiency figure of merit (220) is better than previously reported values. Nevertheless, the bandwidth (2.4 bps) and maximum communication distance (19 m) of this transmitter are less than other reported transmitters. The bandwidth of a few bps is enough for many IoT applications, such as

monitoring and reporting when pertinent events occur [42], [161]. In the case of distance, the transmitter can be linearly cascaded, distributed, or arrayed to communicate over larger areas depending on its applications [37], [185].

Table 5.4: Comparison with previous work.

Ref.	Work	Tech-nique	Freq-uency	Efficiency figure of merit Dipole/power Am2/W	Power	Size	Dipole equivalent	Calculated distance (1 fT)	Mod-ulation	Band-width
Domingo [36]	Proposed	Coil	500 Hz	N/A	N/A	6x3x3m	N/A	N/A	16-QAM	7 kbps
Dinn [162]	N/A	Coil	575Hz	75	0.4 W	2m	30 $A \cdot m^2$	1.8 km	N/A	2 bps
Sojdehei [162]	Demonstrated	Coil	630-2070Hz	N/A	N/A	56x36x 18cm	110-250 $A \cdot m^2$	2.8 km	FSK	100-300bps
Strachen [164]	Demonstrated	Spin magnet	150 Hz	0.22	17 W	11cm	3.8 $A \cdot m^2$	0.9 km	EMR	60 bps
Strachen [164]	Proposed	Spin magnet	575 Hz	13.3	2.25 W	22 cm	30 $A \cdot m^2$	1.8 km	EMR	60 bps
This work (0.1 V-OOK)	Demonstrated	Dither magnet	893 Hz	**220**	**72 nW**	**2.4 cm^3**	16 $\mu A \cdot m^2$	15 m	AM/OOK	2.4 Hz/ 2.4 bps
This work (0.5 V-OOK)	Demonstrated	Dither magnet	893 Hz	**20**	**1.8 µW**	**2.4 cm^3**	36 $\mu A \cdot m^2$	19 m	AM/OOK	2.4 Hz/ 2.4 bps

Since ULF transmitters are much smaller than the wavelength, several antennas can be arrayed, as shown in Figure 5.17. From the superposition principle, the magnetic field from each antenna adds up linearly. If permanent magnets point in the same direction, the magnetic field amplitude in (5.11) becomes,

$$\vec{B}_{max,array} = n\frac{\mu_0}{4\pi}\frac{2m_0\,\alpha_0}{r^3}\hat{r} \tag{5.18}$$

where n is the number of magnets in the array. As a result, the communication distance increases as $n^{1/3}$. An example of an array of a microfabricated magnet is shown in Figure 5.17a, where each cell is microfabricated with the structure shown in Figure 5.17b.

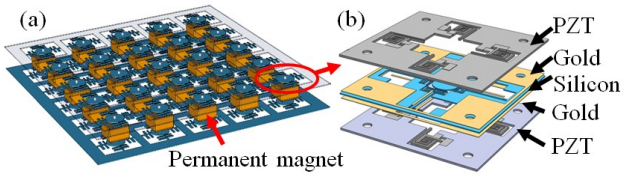

Figure 5.17: (a) An array of ULF antenna consisting of microfabricated PZT-Silicon stage driving permanent magnet. (b) Microfabricated PZT-Silicon stage.

In this chapter, a low-power, small, and lightweight mechanical ULF transmitter is demonstrated. This transmitter significantly improves size and power consumption compared to conventional coil transmitters. Compared to other recent research, this antenna does not contain motors, bearing, or high voltage. The transmitter operates at voltages as low as 0.5 V, which can be driven with standard CMOS IC. This transmitter allows novel applications such as underwater-underground internet-of-things, and direct communication between air, water, and ground. Handheld and UAV applications are possible because the weight is as light as 2.7 g.

CHAPTER 6

HIGH-OVERTONE BULK DIFFRACTION WAVE GYROSCOPE

6.1 Introduction

MEMS Coriolis vibratory gyroscopes are commercially available at low cost and suitable for applications such as smartphones and wearable gadgets. Gyroscopes are sensitive to shock and vibration because of released proof mass can respond to external accelerations by impacting contacts [186]. Gyroscopes without released structures can potentially achieve high bandwidth, high shock tolerance, and high dynamic range [186]. These gyroscopes are suitable for applications such as automotive inertial measurement unit which operate during high impact events such as during collisions, and inertial navigation for space exploration. The accurate values of high rate can enable the inertial navigation.

Gyroscopes without released structures were reported in various forms such as gyroscopes based on surface acoustic wave (SAW), and gyroscopes based on low-order vibration of unreleased structure [39], [186]–[191]. In the latter case, acceleration sensitivities can impact gyroscope accuracy owing to finite spring constants of the vibrating elements. SAW gyroscopes use solidly-attached mass arrays, attached at velocity antinodes, to produce secondary SAWs proportional to the Coriolis force on the masses. So far SAW gyroscopes have been demonstrated with low sensitivity, and high drift [39], [186]–[190]. Integrated graphene piezoresistive or photonic transduction on SAW gyroscope has been explored recently to increase sensitivity, at the cost high complexity of piezoresistive or optical technology integration [192]–[194]. For gyroscopes based on low-order vibration, a gyroscope made of a solid lead zirconate titanate (PZT) block with low sensitivity was shown [191].

In this chapter, relatively high-Q bulk resonances with leaky diffraction are used to increase the sensitivity. The leaked wave can be shear wave that is generated from

bulk mode by Coriolis force on the surface. Using the structure shown in Figure 6.1, the bulk mode resonances were exited such that the drive-sense transfer function demonstrated high-Q (~55,000) gyroscopic response and measure high scale factor for the gyroscope at a frequency substantially different from the SAW gyroscope frequency. Notably, SAW and bulk modes can be operated at independent frequencies, to potentially compensate gyroscope temperature sensitivities.

6.2 Material and Methods

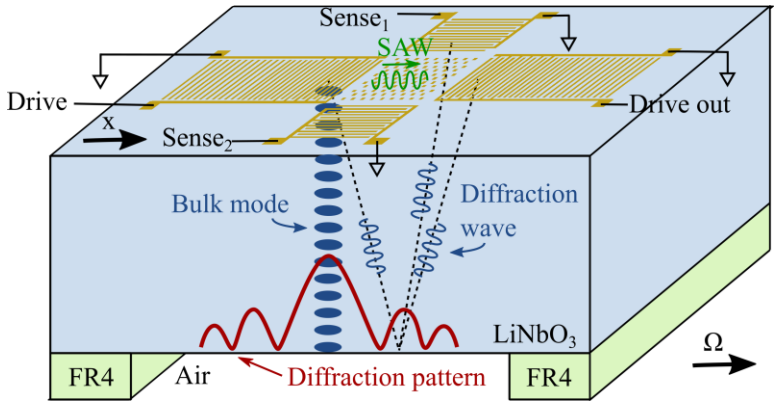

Figure 6.1: Bulk wave diffraction gyroscope operation using wave diffracted from bulk resonator to measure rotation.

The gyroscope operation is illustrated in Figure 6.1. High-order thickness resonance is generated from interdigital transducer (IDT). At the same time, SAW is generated by IDT on the surface. The IDTs are designed with SAW resonance frequency at 80 MHz. Traditionally, responses from IDT in SAW devices other than SAWs are considered as spurious responses. Four common types of the responses are deep bulk acoustic wave, surface skimming bulk wave, leaked bulk acoustic wave, and thickness resonance [195]. A thickness resonance is maintained at high-Q by a stress-free surface at the bottom (Figure 6.1). The bottom surface gives absorption-free reflections, while most of the SAW device bottom surface are sandblasted, coated by an acoustic absorber, or attached using adhesive bonding to suppress spurious modes. Thickness resonance

occurs at periodic frequency spacing $2t/v$, where t is the substrate thickness, and v is the wave speed. Pressure wave and shear wave with different polarization can establish at different frequency due to different wave speeds.

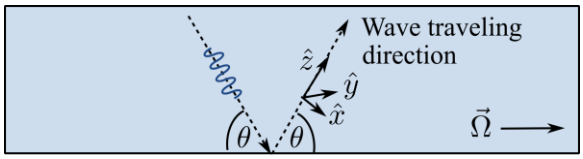

Figure 6.2: Shear wave travels in $\hat{z}$ direction with polarization in $\hat{x}$ and $\hat{y}$ direction.

For pressure and shear bulk elastic waves in the rotating earth, it has been shown that rotation effects the shear wave polarization [196]. If the wave is propagating in z direction (Figure 6.2) as $\vec{u}(z,t) = \vec{A}_s(z)e^{i(kz-\omega t)}$, and external rotation Ω is applied in the direction $\hat{\Omega}$ with angle θ to $\hat{z}$, the amplitude of shear wave will be affected by Coriolis force as,

$$f = \frac{1}{2\pi}\sqrt{\frac{k}{m}} = \frac{1}{4\pi}\sqrt{\frac{w^3}{AL^3}}\sqrt{\frac{E}{\rho}} \tag{6.1}$$

where k is the wave vector, ω is the wave angular frequency, and $\vec{A}_s(z)$ is the amplitude of the wave. Coriolis effect existence with different forms in the traveling wave has been shown [196], [197]. Shear wave can be generated from bulk mode by Coriolis force on the surface. Following from this insight, in the bulk-wave diffraction-based gyroscope, shear waves generated from higher order diffraction waves from the prime resonance arrive at receive IDTs with different amplitude providing high Q and effective transduction. After shear and pressure waves reach the sense IDTs, output voltage can be read and demodulated to extract rotation signal, with the orientation of the IDT transducers playing a role of wave-polarization sensitivity detectors.

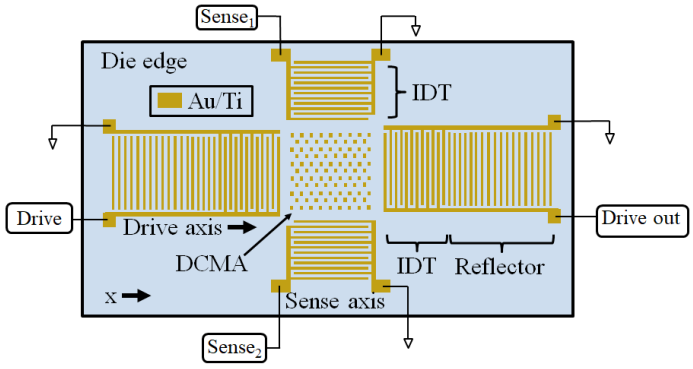

Figure 6.3: Top view of the bulk wave diffraction gyroscope shows electrode patterns.

The top view of the electrode drawing is shown in Fig. 3. The gyroscope consists of drive IDT, drive reflector, sense IDT, and Distributed Coriolis Mass Array (DCMA). Drive IDT generates bulk wave underneath and SAW wave on the surface. Sense IDT transduces SAW and bulk wave to output voltage contain rotation signal. Drive reflector create a resonator in the SAW drive axis. DCMA is series of metal blocks ($\lambda_x/4 \times \lambda_y/4$) in a checker board fashion places at the antinodes with maximum out-of-plane velocity such that the response from Coriolis generate a constructive interference at the sense IDT [187]. The gyroscope is fabricated by a 2-step lift off metal deposition process on 500-µm-thick Y-128° black lithium niobate substrate [187].

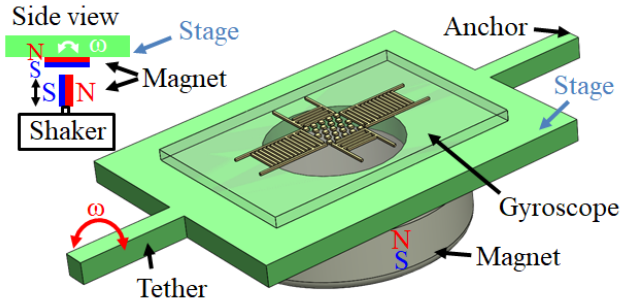

Figure 6.4: Gyroscope is integrated on magnetically driven FR4 stage. Inset shows side view of the FR4 stage is actuated by a magnetic coupling.

A custom FR4-PCB magnetic actuated rate-applying stage is implemented for rapid testing of the RF driven gyroscope as shown in Figure 6.4. After fabrication, wafer

is diced, and a gyroscope die is mounted on a FR4 PC board with a circular orifice at the center to create the stress-free boundary condition. The PC board was designed with groove cuts to form a mechanical stage that can bend to create a twist action on the gyroscope. A permanent magnet is attached under the stage. The stage is actuated by a magnetic coupling with another permanent magnet actuated by mechanical shaker (PASCO SF-9324). Magnet direction are shown in Figure 6.4 inset. Previous works show that using integrated dither stage can calibrate commercial gyroscopes with acceptable accuracy without the need of a rate table [61], [88], [127], [129]. A photograph of a gyroscope attached onto PC board is shown in Figure 6.5a. The stage motion is optically calibrated by measuring reflected laser scanning length as shown in Figure 6.5b inset. An example of the dither rate as a function of mechanical shaker drive voltage is shown in Figure 6.5b.

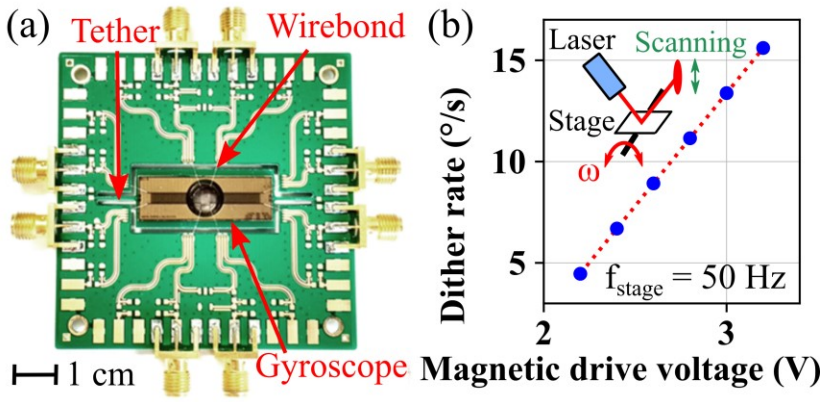

Figure 6.5: (a) Top view of the gyroscope on a PCB with integrated FR4 stage (b) Calibrated dither rate. Inset shows stage calibrating setup diagram.

6.3 Results

Gyroscope output is measured by driving and sensing using a high frequency lock-in amplifier (Zurich UHFLI) with connection diagram shown in Figure 6.6. The gyroscope is driven at the drive IDT with 7.5 dBm power from the lock-in amplifier. The outputs from sense IDT are pre-amplified by RF amplifier (Crystek CRBAMP-100-

6000) with gain +18 dB. The output from the amplifier is connected to Zurich UHFLI. An input rail of the UHFLI is set to around 50% larger than the input signal level to minimize quantization noise, while signal does not exceed the maximum range. The amplified input signal is demodulated respective to the drive RF frequency. The 1st demodulated output represents gyroscope signal with zero rate bias. In order to find drive RF frequency corresponds to maximum gyroscopic response, drive RF frequency is swept while mechanically dithering the gyroscope. The 1st demodulated output is demodulated respective to mechanical stimuli frequency. The 2nd demodulated output as a function of RF frequency represents relative gyroscopic response.

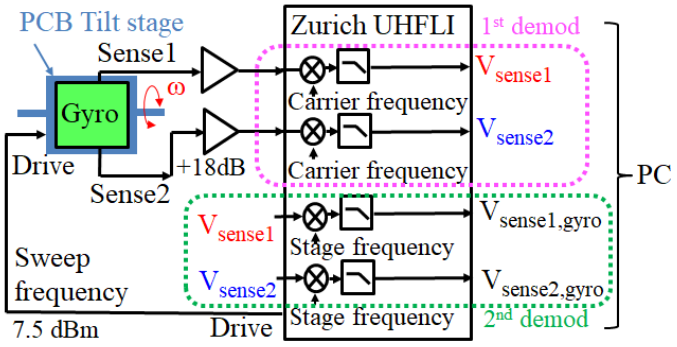

Figure 6.6: Double demodulation measurement block diagram shows gyroscope is driven and sensed by Zurich UHFLI.

Thickness resonance mode is studied by COMSOL finite element simulation software. The model uses eigenfrequency study on a semi-infinite rectangle of 500-μm-thick Y128° lithium-niobate with free boundary condition on top and bottom. Periodic boundary condition is used on 4 edges to simulate infinitely large structure. The frequency of the bulk mode spacing is 7.5 MHz, shear with polarization in x (drive axis) spacing is 4.1 MHz, shear with polarization perpendicular to *x*-direction (sense axis) frequency spacing is 4.2 MHz. Gyroscope sample without drive reflector and DCMA are fabricated and tested on dither stage. The 1st demodulation in Figure 6.7 shows two

sets of resonances corresponding to resonances from the shear waves and pressure waves owing to different velocities [198]. Measured bulk-mode resonance frequencies agree with the analytical analysis and numerical simulation of high-overtone bulk acoustic resonator (HBAR). The effective transducer aperture determines the bulk-wave generation and diffraction [199].

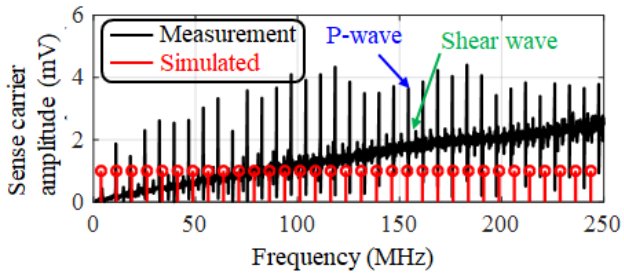

Figure 6.7: Sense port carrier amplitude shows modes with frequency compared with COMSOL simulation.

RF frequency corresponds to maximum scale factor is found by double demodulation measurement with frequency sweep from 1 - 450 MHz. RF frequency around 163.8 MHz showed maximum gyroscopic response. Because the gyroscope bandwidth is small, RF frequency is swept from 163.7-163.8 MHz as shown in Figure 6.8a. The maximum gyroscopic sensitivity corresponds to RF frequency of 163.766 MHz. Scale factor is calibrated by fixing mechanical shaker frequency to 50 Hz, and varying shaker voltage. The dither rate is measured by calculating from laser scanning length. The minimum dither rate was limited when laser spot size is comparable with scanning length. Scale factor without gain from preamplifier and lock-in amplifier was measured to be 191 μV/(deg/s) as shown in Figure 6.8b.

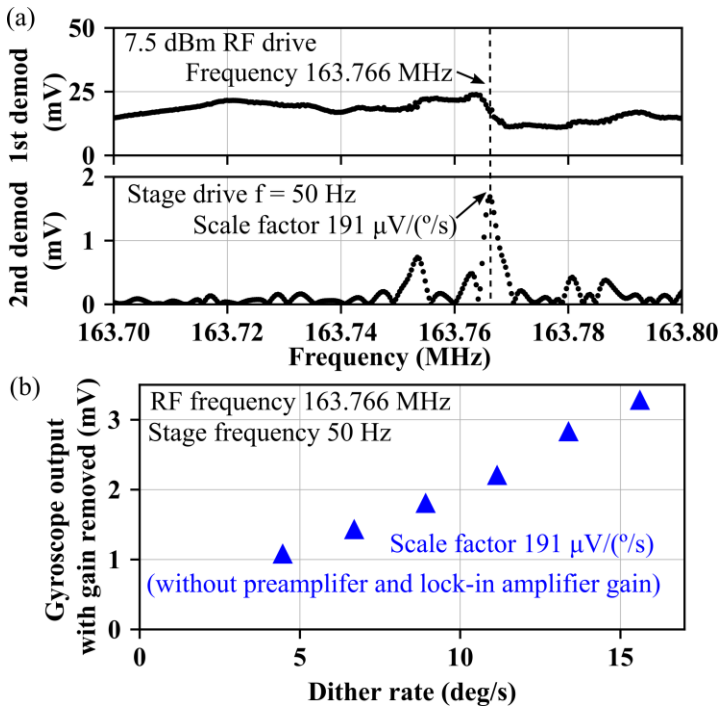

Figure 6.8: (a) Double demodulation measurement result shows RF frequency that corresponds to maximum scale factor (b) Scale factor measurement of the bulk gyroscope on magnetic dither stage setup. The plot shows gyroscope output with gain removed.

Zero rotation rate output (ZRO) is measured by setting mechanical shaker amplitude to 0V, while keep other setting identical to scale factor measurement. The demodulated output from Zurich UHFLI is recorded. Zero rate is calculated by the scale factor from Figure 6.8b. Allan deviation is calculated and plotted in Figure 6.9. The best-case angle random walk (ARW) and bias instability are extracted from the plot as 0.028 deg/hr$^{1/2}$ and 8 deg/hr, respectively. The peaking occurs due to sinusoidal interference and can be removed [200].

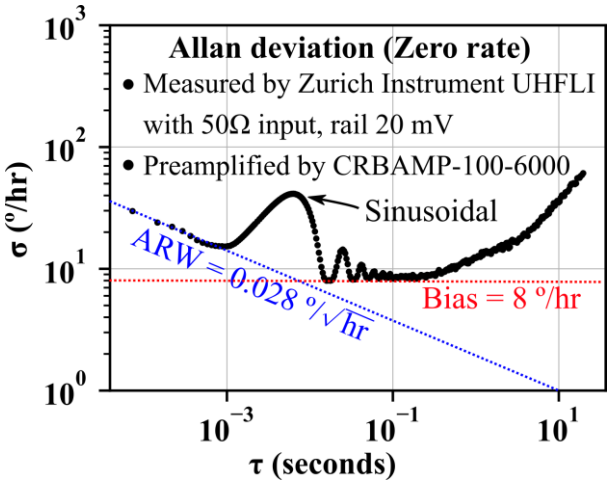

Figure 6.9: Allan deviation of zero rate output (ZRO). The peaking occurs due to interference and can be removed.

The measured gyroscope scale factor, without gain of the preamplifier and lock-in amplifier, is 191 μV/(deg/s), which is one of the largest scale factors reported for an all-solid-state gyroscope (Table 6.1).

Table 6.1: Comparison of previous solid-state gyroscope with this work.

SS - Gyro	Freq.	ARW	SF	Pillar
Ref [39]	80 MHz	Not reported	3.2 μV/Deg/S	Au (400 nm)
Ref [189]	115 MHz	5.5 $°/\sqrt{hr}$	0.96 μV/Deg/S	Au (282 nm)
This work	164 MHz	0.028 $°/\sqrt{hr}$	191 μV/Deg/S	Au (400 nm)

6.4 Conclusion

A new type of gyroscope using high-overtone bulk waves with diffraction is fabricated and tested. The gyroscope has high shock-tolerance due to the lack of released structures. The gyroscope bulk modes are characterized consisting of pressure and shear wave resonators. Scale factor of gyroscope sensitivity are calibrated with integrated PCB stage. Allan deviation plot are shown with extracted angle random walk and bias fluctuation. This gyroscope has the best scale factor, ARW, and bias fluctuation for

solid-state-acoustic gyroscope. Optimal operation of the gyroscope is under way to incorporate the effects of transducer placement and multi-mode operation.

CHAPTER 7

HIGH-OVERTONE BULK DIFFRACTION WAVE GYROSCOPE: THEORY

7.1 Introduction

MEMS micro Coriolis vibratory gyroscopes (μCVG) are widely integrated in consumer electronics because of their low cost and acceptable sensitivity and noise performance. However, one of the drawbacks of μCVGs is sensitivity to high levels of shock because its released proof mass can impact surrounding structures [39]. In contrast, gyroscopes that utilize high-frequency vibration of solidly mounted structures such as surface acoustic wave (SAW) gyroscopes and thickness shear gyroscopes have high shock tolerance [39], [188]–[190], [192], [193], [201]. Moreover, since the oscillation of the proof mass occurs at high frequency (>MHz), this type of gyroscope has high bandwidth. Furthermore, the lack of any released parts leads to higher yields and lower fabrication cost. The lack of gaps means that stress-induced gap variations play a minimal role in gyroscope bias. High-shock tolerant gyroscopes allow for various applications such as to increase safety levels in smart automobiles, to aid in space exploration, and to enhance military technology. Nevertheless, these existing gyroscopes with solidly mounted proof masses suffer from low scale factors, which refer to low rotation sensitivity [39], [188]–[190], [192], [193], [201].

A gyroscopic mechanism was discovered using a gyroscope designed to be a SAW gyroscope [201]–[203]. This gyroscope is driven by interdigital transducer (IDT) and metal electrodes in high-overtone bulk acoustic wave resonance modes. The gyroscopic sensitivity of the high-overtone resonance mode was discovered to accidentally coexist with surface acoustic wave (SAW) gyroscopes [201]. Investigating mechanical waves in rotating media can further elucidate the operation of the high-overtone bulk diffraction wave gyroscope.

Several authors studied the effect of rotation on the bulk acoustic waves for geoscience and gyroscope applications. Geoscience applications include the effects of rotation on seismic waves that are theoretically studied in different conditions, such as medium with thermoelastic coupling, and medium with void [197], [204]–[207]. The solutions from these studies are complex and not suitable for modeling the gyroscope. For example, in 1973, Schoenberg and Censor described the effect of rotation on a traveling bulk acoustic wave with a slowness curve, which is a second-order changing of wave speed [207]. As for applications for the gyroscope, several authors proposed the idea of thickness shear gyroscopes, which utilize the effect of rotation on standing shear wave in the thickness resonances [208]–[215]. However, the thickness shear gyroscopes models are designed for standing wave instead of the traveling wave.

In 2016, Snieder *et al*. theoretically derived and experimentally confirmed that the polarization of seismic shear wave rotates in the opposite direction of the Earth's rotation [196]. The derivation was simplified to the first-order effect of Ω/ω, where Ω is the rotation rate of the media, and ω is the shear wave angular frequency. The measured polarization of the shear wave generated by an earthquake was consistent with this theory. The polarization rotation of shear waves can potentially explain the complete model of the gyroscope.

In this chapter, a new principle of operation of a gyroscope that utilizes longitudinal pressure waves and shear waves to measure rotation rate is presented. The gyroscope is designed to sense gyroscopic effect from only the diffraction wave, as explained in 7.2. The first-order effect of rotation on shear wave is investigated in 7.3. From the results, the gyroscope is analyzed and modeled to calculate the scale factor expression in 7.4. An example of the gyroscope geometry and material is shown with calculated scale factor number in 7.5.

7.2 Bulk wave gyroscope design

In this section, a high-overtone bulk diffraction wave gyroscope design and analysis are presented. The gyroscope is fabricated on lithium niobate ($LiNbO_3$) substrates with metal electrode geometry shown in Figure 7.1a. The concept can be implemented in other materials such as AlN and PZT in both thin film and bulk forms. This design takes advantage of the drive standing wave to increase gyroscope sensitivity. The cross-section at the dashed line in Figure 7.1a is shown in Figure 7.1b to further illustrate gyroscope operation.

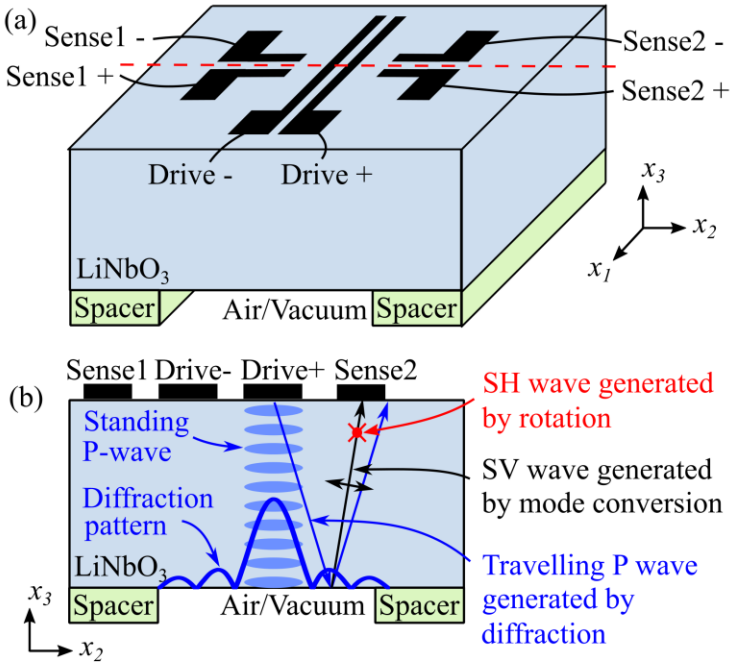

Figure 7.1: (a) A bulk diffraction wave gyroscope consists of metal electrodes on a lithium niobate substrate. (b) Cross-section illustrates the gyroscope operation.

From the gyroscope cross-section in Figure 7.1b, a high-order longitudinal standing wave (P wave) is generated by a pair of drive electrodes, Drive + and Drive -. The P wave thickness resonance is maintained by a stress-free surface at the bottom of the electrodes. The drive electrode length d is designed to be comparable to the P wave wavelength λ_p. The standing P wave generates a traveling P wave due to diffraction. The

traveling P wave generates a traveling shear vertical wave (SV wave) due to mode conversion from reflection at angle. This SV wave polarization rotates due to the Coriolis force from external rotation as described in (7.48). The rotated shear wave is polarized in x_1 direction and can be considered as a shear horizontal wave (SH wave). This SH wave can be measured with sense electrode pairs perpendicular to the drive electrodes. The gyroscope operation is explained in detail and the scale factor is calculated in 7.4.

7.3 The effect of rotation on bulk acoustic waves

The effect of rotation on bulk acoustic waves is investigated to design and model the gyroscope. The governing equations that comprise of stress equations of motion and piezoelectric constitutive equations are described in 7.3.1. From the governing equations, the first-order effect of rotation on the traveling shear wave are derived in 7.3.2. The first-order result that the polarization of shear wave rotates in the opposite direction of the external rotation is used for designing the gyroscope later in this chapter. Next, the thickness shear wave gyroscope is investigated in 7.3.3 to show existing gyroscope type using the effect of rotation on the shear wave resonator [208]–[215].

7.3.1 Governing equations

In this section, governing equations for deriving the effect of rotation on shear wave are listed in full form without assuming crystal symmetry and other approximations. The effect of rotation can be derived from the stress equations of motion in an inertial frame of reference as [216]

$$\boldsymbol{\nabla} \cdot \boldsymbol{T} + \boldsymbol{f} = \rho\, \ddot{\boldsymbol{u}}, \tag{7.1}$$

and in tensor notation as

$$T_{ji,j} + f_i = \rho\, \ddot{u}_i, \tag{7.2}$$

where $\boldsymbol{T}$ and $T_{ji} = T_{ij}$ is the stress tensor, $\boldsymbol{f}$ and f_i is the body force vector, ρ is the mass density, and $\boldsymbol{u}$ and u_i is the mechanical displacement vector. From Newtonian mechanics, a rotating frame of reference can be mathematically treated as an inertial frame with fictitious forces acting on all bodies [217]. In a rotating frame with a rotation vector $\boldsymbol{\Omega}$, Newton's second law $\boldsymbol{F} = m\boldsymbol{a}$ can be written as

$$\boldsymbol{F} - m\dot{\boldsymbol{\Omega}} \times \boldsymbol{r} - 2m\boldsymbol{\Omega} \times \dot{\boldsymbol{r}} - m\boldsymbol{\Omega} \times (\boldsymbol{\Omega} \times \mathbf{r}) = m\boldsymbol{a}, \tag{7.3}$$

where $\boldsymbol{F}$ is the force vector, $\boldsymbol{r}$ is the position vector, $\boldsymbol{a}$ is the acceleration vector, $-m\dot{\boldsymbol{\Omega}} \times \boldsymbol{r}$ is the Euler's angular acceleration force, $-2m\boldsymbol{\Omega} \times \dot{\boldsymbol{r}}$ is the Coriolis force, and $-m\boldsymbol{\Omega} \times (\boldsymbol{\Omega} \times \mathbf{r})$ is the centrifugal force. Similarly, the stress equations of motion (7.1) in a rotating frame of reference can be written with pseudo force as

$$\boldsymbol{\nabla} \cdot \boldsymbol{T} + \boldsymbol{f} - \rho\dot{\boldsymbol{\Omega}} \times \boldsymbol{r} - 2\rho\boldsymbol{\Omega} \times \dot{\boldsymbol{r}} - \rho\boldsymbol{\Omega} \times (\boldsymbol{\Omega} \times \mathbf{r}) = \rho\ddot{\boldsymbol{u}}, \tag{7.4}$$

and in the tensor notation as

$$T_{ji,j} + f_i - 2\rho e_{ijk}\dot{\Omega}_j u_k - 2\rho e_{ijk}\Omega_j \dot{u}_k - \rho(\Omega_i\Omega_j u_j - \Omega_j\Omega_j u_i) = \rho\ddot{u}_i, \tag{7.5}$$

where $i, j,$ and k are tensor index.

Material stress-strain relation is required for solving the stress equations of motion. For piezoelectric material, there are several commonly used forms of the constitutive equations [218]. In this work, the following piezoelectric constitutive equations will be used for convenience:

$$\text{(a) } [S] = [s^E][T] + [d]^t[E], \qquad (b)\ [D] = [d][T] + [\epsilon^T][E], \tag{7.6}$$

where $[S]$ is a strain tensor, $[T]$ is a stress tensor, $[E]$ is an electric field vector, $[D]$ is an electric displacement vector, $[s^E]$ is a compliance tensor measured under constant electric field, $[\epsilon^T]$ is a compliance tensor measured under constant stress, and $[d]^t$ is a

transposed piezoelectric coefficient tensor. To simplify, the brackets and superscripted *E* and *T* are omitted as

$$\text{(a) } \boldsymbol{S} = \boldsymbol{s}\,\boldsymbol{T} + \boldsymbol{d}^{t}\boldsymbol{E}, \qquad \text{(b) } \boldsymbol{D} = \boldsymbol{d}\,\boldsymbol{T} + \boldsymbol{\epsilon}\,\boldsymbol{E}, \tag{7.7}$$

and in the tensor notation as

$$\text{(a) } S_{ij} = s_{ijkl}\,T_{kl} + d_{kij}E_{k}, \qquad \text{(b) } D_{i} = d_{ijk}\,T_{jk} + \epsilon_{ij}\,E_{j}. \tag{7.8}$$

Equations (7.8) can be written in other form such as

$$\text{(a) } T_{ij} = c_{ijkl}\,S_{kl} - e_{kij}E_{k}, \qquad \text{(b) } D_{i} = e_{ijk}\,S_{jk} + \epsilon_{ij}\,E_{j}, \tag{7.9}$$

where c_{ijkl} is a stiffness tensor, and e_{kij} is a piezoelectric coefficient tensor.

Equations (7.5) and (7.8) can be rigorously solved without approximations, but the solutions are complicated [208]. In the following sections, two simplified cases are shown along with their first-order solutions. First, the first-order effect of rotation on a traveling shear wave in an isotropic media is shown in 7.3.2. Since traveling wave directions can be arbitrary, assuming isotropic media significantly simplifies the solution. Second, the first-order effect of rotation on thickness shear wave resonator is shown in 7.3.3. In this case, the shear wave is confined in a standing wave with known polarization directions. Considering only relevant equations for the standing wave greatly reduces complexity.

7.3.2 Traveling shear waves in rotating media

In this section, the first-order effect of rotation on traveling shear waves is derived from the constitutive equations in (7.5) and (7.8). The result from this section is used to analyze the gyroscope in the next section (7.4). A plane shear wave travels in x_3 direction with u_1 and u_2 displacement fields representing polarization in x_1 and x_2, as shown in Figure 7.2. This shear wave is in a rotating media with rotation vector $\boldsymbol{\Omega}$. This

derivation can explain shear wave traveling in arbitrary directions by rotating material property matrices.

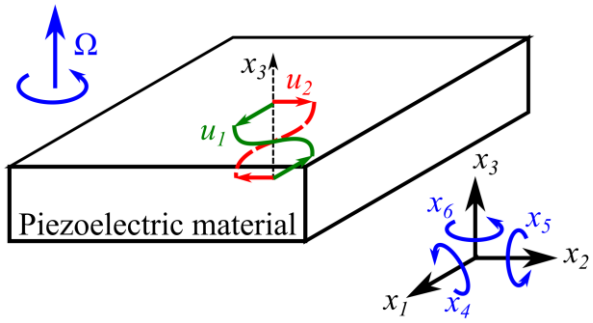

Figure 7.2: Traveling shear waves in rotating media.

The transverse displacement field can be described as a general form of a plane wave in the tensor notation form as

$$u_1 = A\exp(jkx_3)\exp(j\omega t), \tag{7.10}$$

$$u_2 = B\exp(jkx_3)\exp(j\omega t), \tag{7.11}$$

$$u_3 = 0, \tag{7.12}$$

where u_i is the displacement field in x_i direction, A and B are the complex wave amplitudes, k is the wave number, ω is the angular frequency, t is time, and j is imaginary unit. From the stress equations of motion in (7.5), considering only constant rotation ($\dot{\Omega} = 0$), and no external force ($f = 0$), the equations are reduced to

$$T_{ji,j} - 2\rho e_{ijk}\Omega_j\dot{u}_k - \rho(\Omega_i\Omega_j u_j - \Omega_j\Omega_j u_i) = \rho\,\ddot{u}_i. \tag{7.13}$$

In the gyroscope, the external rotation rate of the media is much slower than the wave frequency ($\Omega \ll \omega$). In the first-order approximation, the second-order centrifugal terms can be neglected. Furthermore, since the displacement in the traveling direction u_3 is negligible as in (7.12), equations for $i = 3$ can be ignored. After the approximation, the relevant equations are

$$T_{31,3} + 2\rho\Omega_3\dot{u}_2 = \rho\,\ddot{u_1}, \tag{7.14}$$

$$T_{32,3} - 2\rho\Omega_3\dot{u}_1 = \rho\,\ddot{u_2}. \tag{7.15}$$

The index *ij* can be written in the reduced form as [219]

$$T_{5,3} + 2\rho\Omega_3\dot{u}_2 = \rho\,\ddot{u_1}, \tag{7.16}$$

$$T_{4,3} - 2\rho\Omega_3\dot{u}_1 = \rho\,\ddot{u_2}. \tag{7.17}$$

From the piezoelectric constitutive equations in (7.9), the relevant equations are

$$T_5 = c_{\mathbf{55}}\,S_5 - e_{25}E_2, \tag{7.18}$$

$$T_4 = c_{44}\,S_4 - e_{14}E_1. \tag{7.19}$$

From the definition of compressed notation $S_p = 2S_{ij}$ when $i \neq j, p = 4, 5, 6$ and the definition of strain $S_{ij} = (u_{i,j} + u_{j,i}\,)/2$, the strain can be written in the displacement field as

$$T_5 = c_{55}u_{1,3} - e_{25}E_2, \tag{7.20}$$

$$T_4 = c_{44}u_{2,3} - e_{14}E_1. \tag{7.21}$$

Substitute T_5 and T_4 from (7.20), and (7.21) into (7.16), and (7.17), the equations become

$$c_{55}u_{1,33} + 2\rho\Omega_3\dot{u}_2 = \rho\,\ddot{u_1}, \tag{7.22}$$

$$c_{44}u_{2,33} - 2\rho\Omega_3\dot{u}_1 = \rho\,\ddot{u_2}. \tag{7.23}$$

This is a system of coupled linear differential equations, which can be solved by substituting general assumed solutions u_1 and u_2 from (7.10) and (7.11). The characteristic equations are

$$-c_{55}k^2A + 2\rho\Omega_3 Bj\omega\ = -\omega^2\rho\,A, \tag{7.24}$$

$$-c_{44}k^2B - 2\rho\Omega_3 Aj\omega\ = -\omega^2\rho\,B. \tag{7.25}$$

These equations can be rearranged as

$$\left(\frac{c_{55}}{\rho}\frac{k^2}{\omega^2}-1\right)A-2j\,\frac{\Omega_3}{\omega}\,B=0, \tag{7.26}$$

$$2j\,\frac{\Omega_3}{\omega}\,A+\left(\frac{c_{44}}{\rho}\frac{k^2}{\omega^2}-1\right)B=0, \tag{7.27}$$

which is in matrix form given by

$$\begin{bmatrix}\left(\frac{c_{55}}{\rho}\frac{k^2}{\omega^2}-1\right) & -2j\,\frac{\Omega_3}{\omega}\\ 2j\,\frac{\Omega_3}{\omega} & \left(\frac{c_{44}}{\rho}\frac{k^2}{\omega^2}-1\right)\end{bmatrix}\begin{bmatrix}A\\B\end{bmatrix}=0. \tag{7.28}$$

Since A and B are independent variables, the differential equations will be satisfied for every A and B only when the determinant is zero. This condition gives a dispersion equation in the form of

$$\left(\frac{c_{44}}{\rho}\frac{k^2}{\omega^2}-1\right)\left(\frac{c_{55}}{\rho}\frac{k^2}{\omega^2}-1\right)-\left(\frac{2\Omega_3}{\omega}\right)^2=0. \tag{7.29}$$

This equation can be solved by gathering the $k^2/(\rho\omega^2)$ terms, and arranged into a quadratic equation as

$$c_{44}c_{55}\left(\frac{k^2}{\rho\omega^2}\right)^2-(c_{44}+c_{55})\left(\frac{k^2}{\rho\omega^2}\right)+1-\left(\frac{2\Omega_3}{\omega}\right)^2=0. \tag{7.30}$$

The two solutions of the quadratic equation are

$$\frac{k^2}{\rho\omega^2}=\frac{(c_{44}+c_{55})\pm\sqrt{(c_{44}+c_{55})^2-4c_{44}c_{55}+4c_{44}c_{55}\left(\frac{2\Omega_3}{\omega}\right)^2}}{2c_{44}c_{55}}. \tag{7.31}$$

These two solutions represent two shear waves that travel at different speeds. The wavenumber k can be solved as

$$k=\pm\sqrt{\rho\omega^2\frac{(c_{44}+c_{55})\pm\sqrt{(c_{44}+c_{55})^2-4c_{44}c_{55}+4c_{44}c_{55}\left(\frac{2\Omega_3}{\omega}\right)^2}}{2c_{44}c_{55}}}. \tag{7.32}$$

The positive and negative values of k indicate the direction that the wave travels in the x_3 axis. The relation between u_1 and u_2 can be obtained by substituting B by αA into (7.28). The full solution of the wave is

$$u_1 = \sum_{m=1}^{4} A_m \exp(jk_m x_3) \exp(j\omega t), \tag{7.33}$$

$$u_2 = \sum_{m=1}^{4} A_m \alpha_m \exp(jk_m x_3) \exp(j\omega t), \tag{7.34}$$

$$\alpha_m = -j \frac{\omega}{2\Omega_3} \left(\frac{c_{55}}{\rho} \frac{k_m^2}{\omega^2} - 1 \right), \tag{7.35}$$

$$k_1 = +\sqrt{\rho\omega^2 \frac{(c_{44}+c_{55}) + \sqrt{(c_{44}+c_{55})^2 - 4c_{44}c_{55} + 4c_{44}c_{55}\left(\frac{2\Omega_3}{\omega}\right)^2}}{2c_{44}c_{55}}}, \tag{7.36}$$

$$k_2 = +\sqrt{\rho\omega^2 \frac{(c_{44}+c_{55}) - \sqrt{(c_{44}+c_{55})^2 - 4c_{44}c_{55} + 4c_{44}c_{55}\left(\frac{2\Omega_3}{\omega}\right)^2}}{2c_{44}c_{55}}}, \tag{7.37}$$

$$k_3 = -\sqrt{\rho\omega^2 \frac{(c_{44}+c_{55}) + \sqrt{(c_{44}+c_{55})^2 - 4c_{44}c_{55} + 4c_{44}c_{55}\left(\frac{2\Omega_3}{\omega}\right)^2}}{2c_{44}c_{55}}}, \tag{7.38}$$

$$k_4 = -\sqrt{\rho\omega^2 \frac{(c_{44}+c_{55}) - \sqrt{(c_{44}+c_{55})^2 - 4c_{44}c_{55} + 4c_{44}c_{55}\left(\frac{2\Omega_3}{\omega}\right)^2}}{2c_{44}c_{55}}}. \tag{7.39}$$

Many piezoelectric materials such as PZT ceramics and sputtered AlN thin films have in-plane symmetry: $c_{44} = c_{55}$. In this case, the wave number (k) can be simplified and approximated as,

$$\alpha_1 = -j; \qquad k_1 \approx \sqrt{\frac{\rho}{c_{55}}}\omega \left(1 + \frac{\Omega_3}{\omega}\right), \tag{7.40}$$

$$\alpha_2 = +j; \qquad k_2 \approx \sqrt{\frac{\rho}{c_{55}}}\omega \left(1 - \frac{\Omega_3}{\omega}\right), \tag{7.41}$$

$$\alpha_3 = -j; \qquad k_3 \approx -\sqrt{\frac{\rho}{c_{55}}}\omega \left(1 + \frac{\Omega_3}{\omega}\right), \tag{7.42}$$

$$\alpha_4 = +j; \qquad k_4 \approx -\sqrt{\frac{\rho}{c_{55}}}\omega\left(1 - \frac{\Omega_3}{\omega}\right). \tag{7.43}$$

To interpret the results, the general solution can be written as a linear combination of a plane wave in vector form as [196],

$$\boldsymbol{u}(x_3, t) = \frac{A}{2}(\boldsymbol{e_1} - i\boldsymbol{e_2}) \exp\left(\pm jk_0\left(1 + \frac{\Omega_3}{\omega}\right)x_3 + j\omega t\right) + \frac{A}{2}(\boldsymbol{e_1} + i\boldsymbol{e_2}) \exp\left(\pm jk_0\left(1 - \frac{\Omega_3}{\omega}\right)x_3 + j\omega t\right), \tag{7.44}$$

where $\boldsymbol{e_i}$ is a unit vector i direction, $k_0 = \sqrt{\rho/c_{55}}\omega$ is the wave number without rotation, and A is the wave amplitude. This equation can be written as a wave with circular polarization as

$$\boldsymbol{u}(x_3, t) = A\,\hat{\boldsymbol{q}}(x_3) \exp(\pm jk_0 x_3 + j\omega t), \tag{7.45}$$

where $\hat{\boldsymbol{q}}(x_3)$ is the circular polarization unit vector given by,

$$\hat{\boldsymbol{q}}(x_3) = \boldsymbol{e_1} \cos\left(\pm k_0 \frac{\Omega_3}{\omega} x_3\right) + \boldsymbol{e_2} \sin\left(\pm k_0 \frac{\Omega_3}{\omega} x_3\right). \tag{7.46}$$

The angle θ can be defined as a polarization angle measured from $\boldsymbol{e_1}$ in the $\boldsymbol{e_1}$-$\boldsymbol{e_2}$ plane, and the polarization angle θ is given by

$$\theta(x_3) = \pm k_0 \frac{\Omega_3}{\omega} x_3. \tag{7.47}$$

At rotation rate $\Omega_3 \ll \omega$, the wave speed is a $\mp\omega/k_0$, so the polarization as a function of time is given by

$$\theta(t) = -\Omega_3 t. \tag{7.48}$$

Equation (7.48) indicates that the polarization of the shear wave rotates with the rate $\dot{\theta} = -\Omega_3$, which depends only on the external rotation rate and the traveling time. The polarization angle is independent of the wave traveling direction and the wave frequency.

7.3.3 *Thickness shear resonators in rotating media*

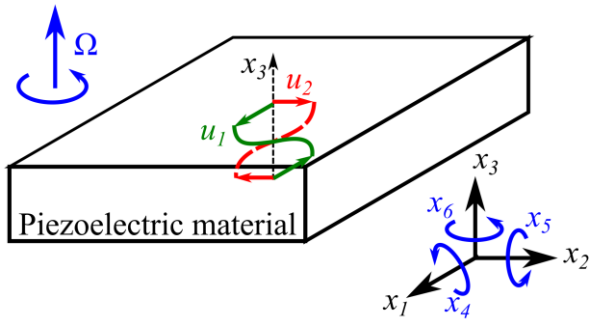

Figure 7.3: A thickness shear resonator in rotating media.

A thickness shear wave gyroscope is investigated to evaluate existing gyroscope designs using the effect of rotation on shear wave resonators [208]–[215]. A thickness shear resonator with thickness t in x_3 direction and infinite size in x_1 and x_2 directions is shown in Figure 7.3. The resonator is rotating with a rotation rate Ω_3 in x_3 direction. The shear wave resonator is driven with the displacement field u_1 in x_1 direction. The standing wave in the resonator can be modeled as a superposition of traveling waves, so the solutions have a general form similar to (7.10), (7.11), and (7.12) given by,

$$u_1 = A_n \exp(jk_n x_3) \exp(j\omega t), \tag{7.49}$$

$$u_2 = A_n \alpha_n \exp(jk_n x_3) \exp(j\omega t), \tag{7.50}$$

$$u_3 = 0, \tag{7.51}$$

where A_n and $A_n \alpha_n$ are the amplitude of the shear wave with the polarization in x_1 and x_2 directions, respectively, k_n is the wave number, and ω is the angular frequency. The governing equations are similar to those of the traveling wave in (7.22) and (7.23) given by,

$$c_{55} u_{1,33} + 2\rho\Omega_3 \dot{u}_2 = \rho\, \ddot{u}_1, \tag{7.52}$$

$$c_{44} u_{2,33} - 2\rho\Omega_3 \dot{u}_1 = \rho\, \ddot{u}_2, \tag{7.53}$$

where ρ is the material density, c_{55} and c_{44} are stiffness coefficients, and $A_n\alpha_n$ is the sensing wave amplitude. Since the shear wave resonator is driven in x_1 direction, the sensing displacement amplitude u_2 is small compared u_1. The resonator generally has a resonance frequency of more than 1 MHz, which is much higher than the rotation rate Ω_3. As a result, the expression $2\rho\Omega_3\dot{u}_2$ in (7.52) is a negligible second-order effect. The governing equation for the driving direction is approximately independent to Ω_3 and u_2 given by

$$c_{55}u_{1,33} = \rho\,\ddot{u_1}. \tag{7.54}$$

This is a second-order linear differential equation, which can be solved by substituting general answers of u_1 from (7.49). After substitution, the characteristic equation is given by

$$-c_{55}k_n^2A = -\omega^2\rho\,A_n. \tag{7.55}$$

This equation can be simplified to obtain the dispersion equation for a thickness shear wave resonator given by

$$k_n^2 = \omega^2\rho/c_{55}. \tag{7.56}$$

To find u_2, an elastic damping can be added to (7.53) as c_{44} becomes $c_{44}(1 + j/Q_s)$ such that [210]

$$c_{44}(1 + j/Q_s)u_{2,33} - 2\rho\Omega_3\dot{u}_1 = \rho\,\ddot{u}_2, \tag{7.57}$$

where Q_s is the quality factor of the sense mode. The differential equation can be solved by substituting general answers of u_1 and u_2 from (7.49) and (7.50), and the characteristic equation is given by

$$-c_{44}\left(1 + \frac{j}{Q_s}\right)k_n^2A_n\alpha_n - 2\rho\Omega_3A_nj\omega\ = -\omega^2\rho\,A_n\alpha_n. \tag{7.58}$$

This equation can be rearranged and solved for the transfer function to sense mode $\alpha_n = u_2/u_1$ given by

$$\alpha_n = \frac{-2\rho\Omega_3 j\omega}{(c_{44}k_n^2\left(1+\frac{j}{Q_s}\right)-\omega^2\rho)}. \tag{7.59}$$

The solution can be obtained by substituting k_n^2 from (7.56), and the sense mode standing wave from (7.49) and (7.50). The displacement field of the shear wave is given by

$$u_2 = -2j\frac{\Omega_3}{\omega}\frac{1}{\left(\frac{c_{44}}{c_{55}}+\frac{c_{44}\ j}{c_{55}Q_s}-1\right)}\ u_1. \tag{7.60}$$

Equation (7.60) describes the sensing shear wave u_2 generated by coupling from the driving shear wave u_1 due to the Coriolis force. The amplitude of the shear wave u_2 is linearly proportional to the external rotation rate Ω_3. This shear wave resonator can be used as a gyroscope by measuring u_2 from its electric potential or current outputs generated by piezoelectric transduction. For materials with in-plane symmetry $(c_{44} = c_{55})$, the driving and sensing resonance modes have the same frequency. Equation (7.60) can be simplified to

$$\text{Mode match } (c_{44} = c_{55}); \qquad u_2 = -2\frac{\Omega_3}{\omega}Q_s u_1. \tag{7.61}$$

Equation (7.61) indicates that decreasing the frequency potentially increases the gyroscope scale factor; however, the trade-offs are lower bandwidth and larger device size.

To match the modes, manufacturing variation is minimized, and followed by adding fine resonance frequency tuning mechanisms and control systems. Because mode matching gyroscopes are challenging to manufacture, most commercial gyroscopes intentionally have different resonance frequencies for driving and sensing modes known as mode split gyroscopes [108]. With the stiffness coefficient $c_{44} \gg c_{55}$,

this thickness-shear wave gyroscope behaves similarly to mode split gyroscope, which can be written as

$$\text{Mode split } (c_{44} \gg c_{55}); \qquad u_2 \approx -2j\frac{\Omega_3}{\omega}\frac{c_{55}}{c_{44}}u_1. \tag{7.62}$$

The thickness shear gyroscopes are compared to the high-overtone bulk diffraction wave gyroscopes in 7.5.

7.4 Gyroscope modeling

The bulk diffraction wave gyroscope can be modeled in separated parts to estimate the scale factor. In this section, variables for each part are defined, followed by detailed explanation in 7.4.1-7.4.6 and numerical results are given in 7.5. The Drive+ electrode is connected to a drive voltage with amplitude V_d and frequency f_d. The electric field between Drive+ and Drive- electrodes generates a traveling P wave with displacement given by

$$u_{dp} = \Gamma_{dp} V_d, \tag{7.63}$$

where Γ_{dp} is the longitudinal wave (P wave) generation coefficient, and u_{dp} is the displacement field of the generated traveling P wave. If f_d matches with one of the resonance frequencies of the high-overtone bulk acoustic resonator (HBAR), the displacement of the P wave at resonance increases to

$$u_{dpr} = Q_p \Gamma_{dp} V_d, \tag{7.64}$$

where u_{dpr} is the P wave amplitude at resonance, and Q_p is the quality factor of the HBAR at the frequency f_d. The Drive+ electrode size is designed to be comparable to the wavelength of the P wave, so a traveling P wave is generated by diffraction with amplitude given by

$$u_{pi} = \Gamma_{diff} u_{dpr}, \tag{7.65}$$

where Γ_{diff} is the diffraction wave coefficient. The P wave u_{pi} travels at angle θ_p and reflects at the free boundary. After reflection, the shear vertical (SV) wave is generated with displacement given by

$$u_{svr} = \Gamma_{sp} u_{pi}, \tag{7.66}$$

where Γ_{sp} is the reflection coefficient of the SV wave. The reflected SV wave u_{svr} polarization is rotated into SH wave due to the Coriolis force from an external rotation, as previously explained in 7.3.2. The SH wave amplitude can be written as

$$u_{sh} = \Gamma_{\Omega} \Omega u_{svr}, \tag{7.67}$$

where Γ_{Ω} is the rotation coefficient from the SV wave to the SH wave, and Ω is the external rotation rate. This SH wave is detected by the sense electrodes designed for measuring the SH wave by using a geometry that is insensitive to the SV wave. The sense electrodes transduce the SH wave and generate output voltage given by

$$V_{sense} = \Gamma_{sense} u_{sh}, \tag{7.68}$$

where Γ_{sense} is the sensing coefficient of the sense electrode. From (7.63) to (7.68), the sense output can be written as

$$V_{sense} = V_d \Gamma_{dp} Q_p \Gamma_{diff} \Gamma_{sp} \Gamma_{\Omega} \Omega \Gamma_{sense}. \tag{7.69}$$

From (7.69), the scale factor, which is the ratio of the rotation rate and output voltage, of the gyroscope can be written as

$$\text{Scale factor} = \Gamma_{BDWG} = V_d \Gamma_{dp} Q_p \Gamma_{diff} \Gamma_{sp} \Gamma_{\Omega} \Gamma_{sense}. \tag{7.70}$$

The scale factor and other variables of an example device will be quantified in 7.5.

In the following sections, a model of the gyroscope will be discussed in further detail, starting with the P wave generation from the drive electrodes in 7.4.1. The P

wave couples with the HBAR, as explained in 7.4.2. The P wave diffracts from the HBAR and generates a P wave traveling at angles, as explained in 7.4.3. The traveling P wave reflects at the free interface and generates the SV wave, as explained in 7.4.4. The SV wave polarization is rotated by the Coriolis force from external rotation and the SH wave is generated, as explained in 7.4.5. The SH wave is transduced into output voltage by the sense electrode, as explained in 7.4.6. This gyroscope output voltage is proportional to the rotation rate with the scale factor calculated in 7.5.

7.4.1 P wave generation by electrodes

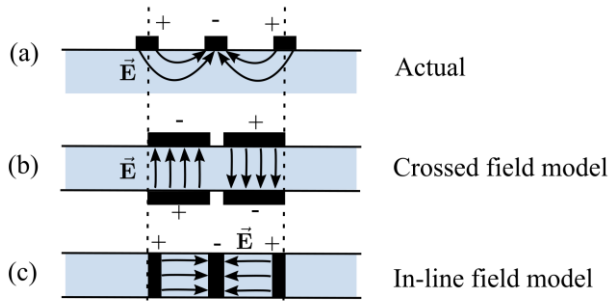

Figure 7.4: Cross-sectional view of the interdigital transducer (IDT) shows electric field patterns with Smith's IDT model (a) Actual field pattern (b) Crossed-field approximation (c) In-line field approximation [220].

The P wave generation by the drive electrodes is modeled to quantify the P wave generation coefficient, Γ_{dp}, previously defined in (7.63). The P wave generation coefficient, Γ_{dp} is used to calculate the gyroscope scale factor in (7.70). The drive electrode can be modeled by Smith's crossed field model, which approximates that the electric field $\vec{\boldsymbol{E}}$ under the drive electrode consists of only the vertical components, as shown in Figure 7.4 [220]. Smith *et al.* proposed that the actual electric field profile of the interdigital transducer (Figure 7.4a) can be approximated by 1) a crossed field model (Figure 7.4b), in which the electric field is only in the vertical direction, or 2) an in-line field model (Figure 7.4c), in which the electric field is only in the horizontal direction [220].

From the cross-field model, the gyroscope drive electrodes can be modeled as shown in Figure 7.5. The cross-section under the drive electrodes at the dashed line in Figure 7.5a is shown in Figure 7.5b. The actual electric field $\vec{\boldsymbol{E}}$ under the sense electrodes (Figure 7.5b) is approximated by the Smith's crossed-field model to consist of only electric field in x_3 (Figure 7.5c). This electric field generates the P wave u_{dp} which couples with the high-overtone bulk acoustic resonator, as explained in the next section (7.4.2). The electric field profile depends on the electrode geometry and piezoelectric material properties. Instead of obtaining the analytical solution, a finite element analysis (FEA) solution is shown later in 7.5 (Figure 7.14).

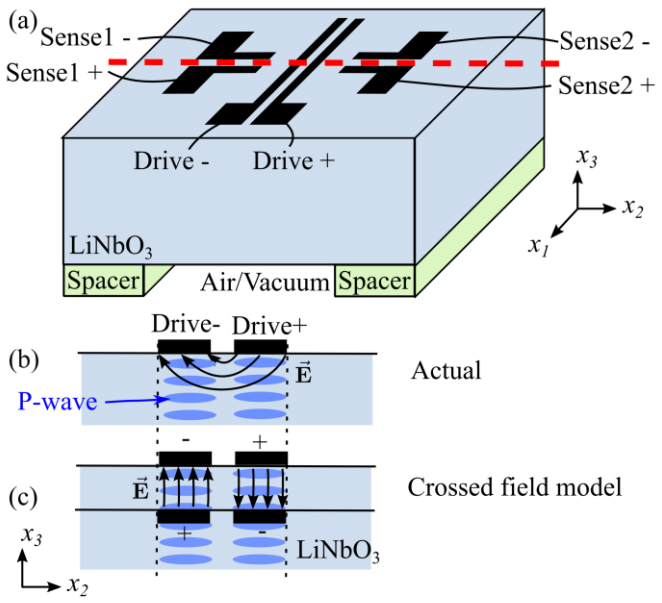

Figure 7.5: The gyroscope model for the P wave generation by the drive electrodes. (a) A 3D illustration shows the electrode pattern. The dashed line shows the cross-section location (b) The actual field pattern under the drive electrodes. (b) The crossed field approximation of the electric field pattern [220].

7.4.2 High-overtone bulk acoustic resonators

A high-overtone bulk acoustic resonator (HBAR) is analyzed to calculate resonance frequency of the resonator. This frequency is used to design gyroscope geometry, as explained in 7.5. From the previous section, the longitudinal wave (P wave)

is generated by the drive electrodes. The P wave is amplified by the resonator if the P wave frequency matches with the resonance frequency of the HBAR. The gyroscope has thickness h with stress-free interface on top and bottom, as shown in Figure 7.6. The resonances are found by the condition given by [221]:

$$h = n\frac{\lambda_p}{2}, \tag{7.71}$$

where λ_p is the wavelength of the P wave, and n is the order of the resonance. Hence, the resonance frequencies of the HBAR can be written as

$$f_p = n\frac{v_p}{2h}, \tag{7.72}$$

where v_p is the P wave phase velocity.

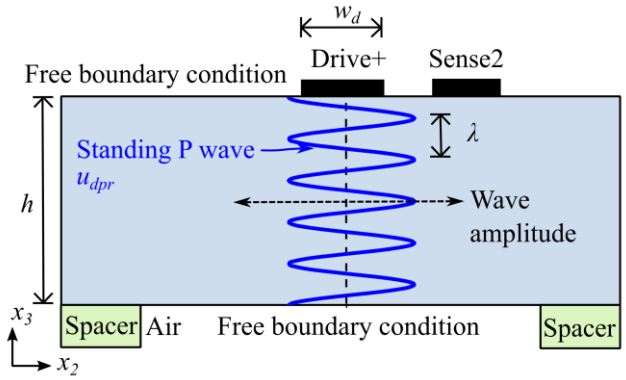

Figure 7.6: The P wave couples to the HBAR formed by the free boundary condition on the top and bottom of the substrate.

Although the quality factor Q is used to calculate the gyroscope scale factor in (7.70), the quality factor depends on several loss processes as given by [8],

$$\frac{1}{Q} = \frac{1}{Q_{air}} + \frac{1}{Q_{material}} + \frac{1}{Q_{other}} \ldots, \tag{7.73}$$

where is Q_{air} is the quality factor corresponding to air damping, $Q_{material}$ is the quality factor corresponding to material damping, and Q_{other} is the quality factor

corresponding to other types of damping. The quality factor value used in the scale factor calculation in 7.5 is obtained from as experiment in Chapter 6.

7.4.3 Diffraction wave

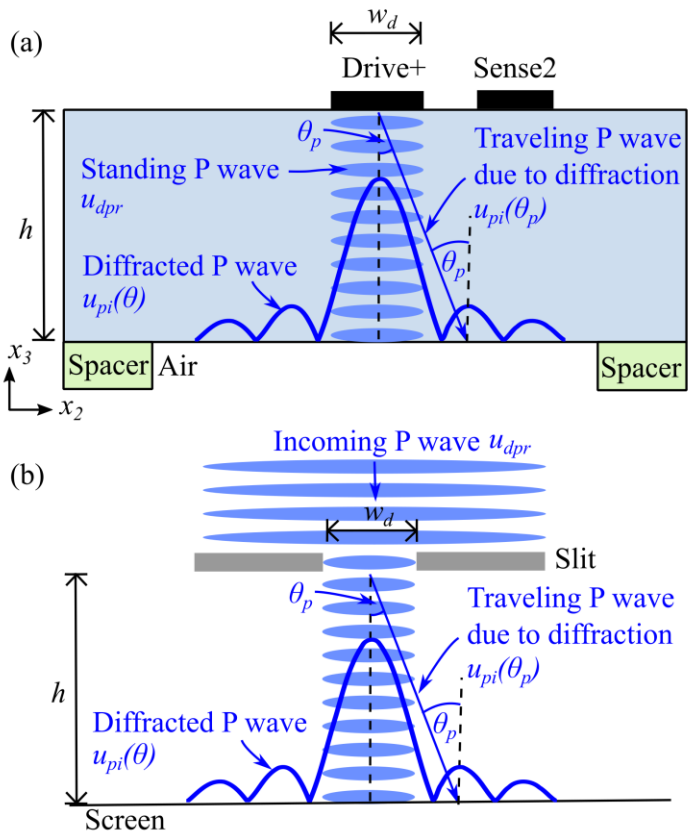

Figure 7.7: (a) The standing P wave diffracts from the Drive+ electrode and generates the traveling P wave (b) Diffraction pattern from a single slit.

Diffraction of the P wave from the Drive+ electrode is analyzed to calculate the diffraction coefficient Γ_{diff} previously defined in (7.65). The Γ_{diff} coefficient is used to calculate the gyroscope scale factor in (7.70). The cross-section of the device illustrating diffraction is shown in Figure 7.7a. The standing P wave with amplitude u_{dpr} is generated from electrode Drive+ and amplified by the HBAR as described in the previous section. The width w_d of the electrodes Drive+ and Drive- is designed to be comparable to the acoustic wavelength. The wave u_{dpr} diffracts and creates a

diffraction pattern $u_{pi}(\theta)$ on the free interface at the bottom side. The first constructive diffraction peak at θ_p generates traveling P wave $u_{pi}(\theta_p)$.

To reduce the complexity of this analysis, the diffraction angle θ is approximated as a small angle. In this region, $LiNbO_3$ is approximately an isotropic material with properties identical to the properties when $\theta = 0$. The length of the electrodes L_d are designed to be much longer than the wavelength. The diffraction process is analyzed as a diffraction from a single slit in one dimension with the width w_d and infinite length (Figure 7.7b). In the single slit analogy, the incoming wave has amplitude of u_{dpr}, and the diffraction wave on the screen has an amplitude of $u_{pi}(\theta)$. From the Fraunhofer approximation, the diffraction wave $u_{pi}(\theta)$ amplitude distribution is given by [218]

$$u_{pi}(\theta) = u_{dpr}\,\mathrm{sinc}\left(\frac{w_d \sin(\theta)}{\lambda_p}\right), \tag{7.74}$$

where the $\mathrm{sinc}(x)$ function is defined as

$$\mathrm{sinc}(x) = \begin{cases} \frac{\sin(\pi x)}{\pi x}; & x \neq 0 \\ 1; & x = 0 \end{cases}. \tag{7.75}$$

The sinc function is defined as $\mathrm{sinc}(x) = \sin(x)/x$ in general [218].

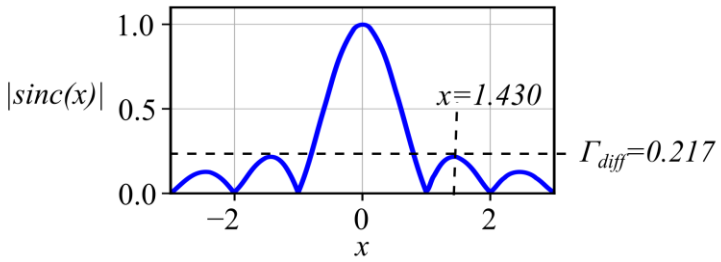

Figure 7.8: A plot of sinc function shows the first constructive diffraction peak.

From (7.65) in section 7.4, the diffraction coefficient Γ_{diff} is the ratio amplitude of the first constructive interference. To find the first constructive interference, the

function $|\mathrm{sinc}(x)|$ is plotted in Figure 7.8. The first constructive diffraction is located at one of the maxima, which can be found by the condition given by

$$\frac{d}{dx}\mathrm{sinc}(x) = 0, \tag{7.76}$$

which leads to the expression given by

$$\tan(\pi x) - \pi x = 0. \tag{7.77}$$

Solving numerically, the location of the first constructive interference can be written as

$$x = \frac{d\sin(\theta)}{\lambda_p} \approx 1.430. \tag{7.78}$$

The diffraction coefficient Γ_{diff} previously defined in (7.65) is given by

$$\Gamma_{diff} \approx \mathrm{sinc}(1.430) \approx 0.217. \tag{7.79}$$

The diffraction coefficient Γ_{diff} is used to calculate the gyroscope scale factor in (7.70). From (7.74), the drive electrode width is given by

$$w_d = \frac{1.430}{\sin(\theta_p)}\frac{v_p}{f_p}. \tag{7.80}$$

where θ_p is the diffracted angle, v_p is the P wave speed, and f_p is the P wave frequency. The drive electrode width is calculated in 7.5 after θ_p, v_p, and f_p are calculated.

7.4.4 Mode conversion due to reflection

Mode conversion from the P wave to the S wave due to reflection is analyzed to calculate the reflection coefficient Γ_{sp} previously defined in (7.66). The reflection coefficient Γ_{sp} is used to calculate the gyroscope scale factor in (7.70). The cross-section of the device illustrating mode conversion is shown in Figure 7.9. The traveling P wave with amplitude $u_{pi}(\theta_p)$ is generated by diffraction from the electrode. The wave $u_{pi}(\theta_p)$ travels at an angle θ_p and reflects the free interface on the bottom side. This

reflection results in a reflected P wave and a shear vertical (SV) wave with polarization in the x_2-x_3 plane. The angle of reflection of the SV wave can be calculated using the Snell law [221]:

$$\frac{v_p}{v_s} = \frac{\sin(\theta_p)}{\sin(\theta_s)}. \tag{7.81}$$

The reflected SV wave is used to measure an external rotation as described in 7.4.5.

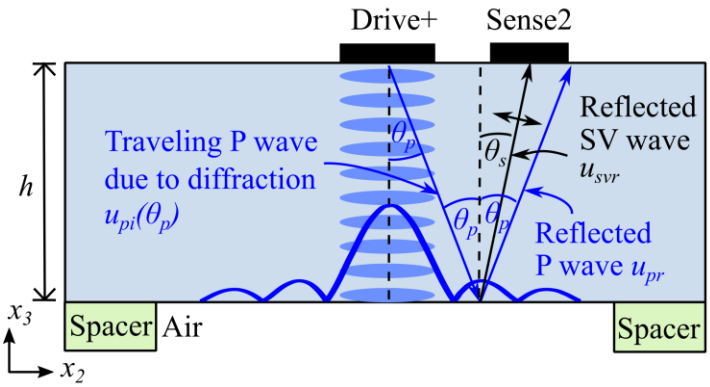

Figure 7.9: The P wave generated by the diffraction is converted to the S wave by the reflection.

Approximating that the angle of incidence θ_p is small, the material properties are identical when $\theta = 0$. The reflection coefficients are given by [221]

$$\Gamma_{pp} = \frac{\sin 2\theta_s \sin 2\theta_p - (v_p/v_s)^2 \cos^2 2\theta_s}{\sin 2\theta_s \sin 2\theta_p + (v_p/v_s)^2 \cos^2 2\theta_s}, \tag{7.82}$$

$$\Gamma_{sp} = \frac{2(v_p/v_s) \sin 2\theta_p \cos 2\theta_s}{\sin 2\theta_s \sin 2\theta_p + (v_p/v_s)^2 \cos^2 2\theta_s}, \tag{7.83}$$

where θ_p is the angle of incidence, θ_s is the angle of reflection of the SV wave, v_p is the P wave speed, v_s is the SV wave speed, Γ_{pp} is the reflection coefficient of the incident P wave to the reflected P wave, and Γ_{sp} is the reflection coefficient of the P wave to the S wave. The reflection coefficients Γ_{pp} and Γ_{sp} are calculated in 7.5.

7.4.5 Shear wave polarization rotation

Shear wave polarization rotation due to the Coriolis force is analyzed to calculate the gyroscope scale factor and the rotation coefficient Γ_Ω as defined in (7.67). The rotation coefficient Γ_Ω is used to calculate the gyroscope scale factor in (7.70). The cross-section of the device illustrating polarization rotation is shown in Figure 7.10. The reflected SV wave u_{svr} is generated from mode conversion, as described in the previous section. Without external rotation, the SV wave u_{svr} has a polarization only in the x_2 and x_3 planes. The polarization angle φ_s rotates in the opposite direction of the external rotation, as described in 7.3.2. This polarization rotation generates a shear horizontal wave u_{sh}.

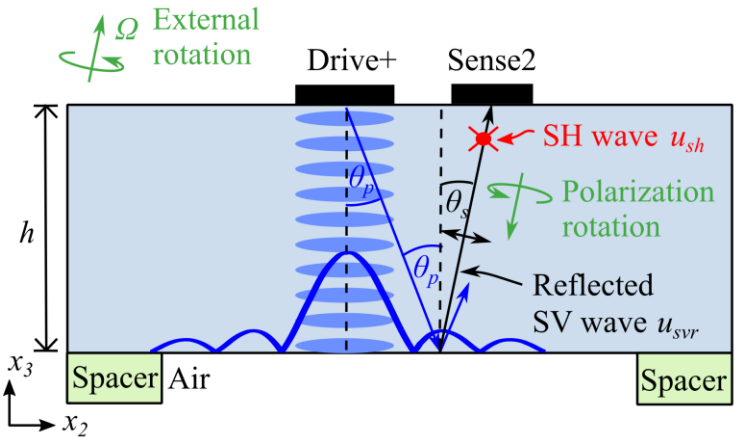

Figure 7.10: The shear vertical (SV) wave polarization rotates and generates the shear horizontal (SH) wave due to external rotation.

From (7.48), the phase φ_s of the reflected shear wave u_{svr} is rotated due to the Coriolis force as

$$\varphi_s(t) = -\Omega \cos(\alpha)\, t, \tag{7.84}$$

where α is the angle between the external rotation vector $\vec{\Omega}$ and the SH wave u_{sh}, and t is the time that the shear wave travels in the rotating medium. The gyroscope sensitivity is maximized when the rotation vector is aligned with the SH wave ($\alpha = 0°$). In this

gyroscope, t is the time that the reflected SV wave u_{svr} travels to the sense electrode. From Figure 7.10, t can be calculated as

$$t = \frac{h}{v_s \cos(\theta_s)}, \tag{7.85}$$

where t is the substrate thickness, θ_s is the angle of reflection of the shear wave, and v_s is the speed of the shear wave. The shear horizontal wave generated by polarization wave rotation is given by

$$u_{sh} = u_{svr} \sin\big(\varphi_s(t)\big). \tag{7.86}$$

If the phase $\varphi_s(t)$ is a small angle, the shear horizontal wave can be written as

$$u_{sh} \approx u_{svr}\varphi_s(t) = -u_{svr} \frac{h}{v_s \cos(\theta_s)} \Omega \cos(\alpha). \tag{7.87}$$

From (7.87), the maximized rotation coefficient Γ_Ω defined in (7.67) is given by

$$\Gamma_\Omega = -\frac{h}{v_s \cos(\theta_s)}, \tag{7.88}$$

where the rotation vector is aligned with the most sensitive direction ($\alpha = 0$). The rotation coefficient Γ_Ω will be quantified in 7.5 and used for calculating the scale factor in (7.70).

7.4.6 Sense electrode

The sense electrode is modeled to calculate the sensing coefficient Γ_{sense}, as previously explained in (7.68). The sensing coefficient Γ_{sense} is used to calculate the gyroscope scale factor in (7.70). From the previous section, the polarization of the shear vertical wave u_{svr} (polarized in the x_2-x_3 plane) is rotated by the Coriolis force into the shear horizontal wave u_{sh} (polarized in x_1 direction), as previously illustrated in Figure

7.10. This shear horizontal wave u_{sh} is transduced to voltage output by piezoelectric transduction at the sense electrodes.

To calculate the sensing coefficient Γ_{sense} of the sense electrode, the device is modeled in Figure 7.11 [220]. The cross-section at the dashed line in Figure 7.11a is shown in Figure 7.11b. Although the shear horizontal wave u_{sh} travels at angle θ_s in the x_2-x_3 plane, the shear wave u_{sh} travels straight in the x_1-x_3 plane to the sense electrodes. The electric field $\vec{\boldsymbol{E}}$ under sense electrode is approximated by Smith's inline field model, which models the electric field profile as straight lines in the x_1 direction [220].

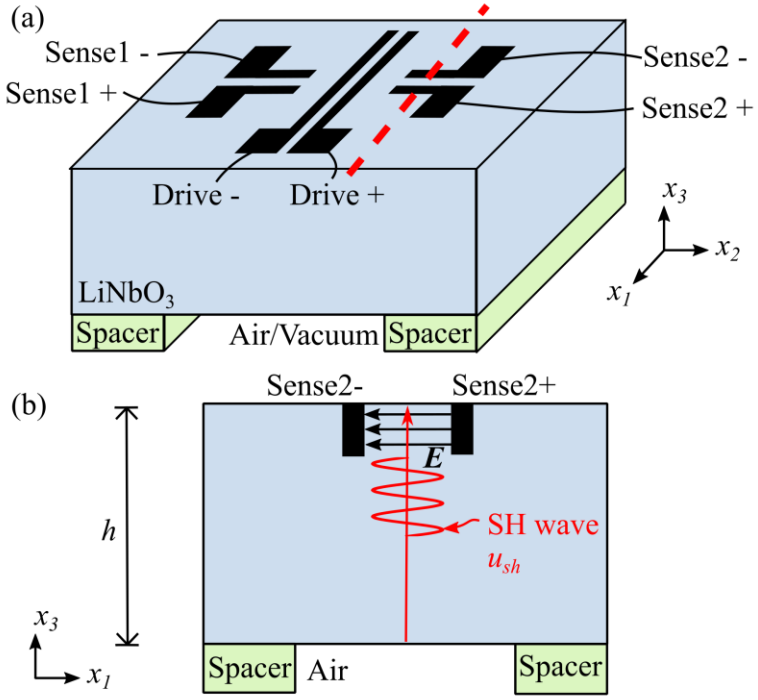

Figure 7.11: The sense electrode transducts the SH wave into output voltage. (a) A 3D illustration shows the electrode pattern with the dashed line indicating the cross-section location. (b) The cross-section shows the electric field pattern under the sense electrode is simplified by the in-line field model [220].

To calculate the sensing coefficient Γ_{sense}, the sense electrode can be modeled by the following piezoelectric constitutive equations:

$$(a)\ [S] = [s^E][T] + [d]^t[E], \qquad (b)\ [D] = [d][T] + [\epsilon^T][E] \qquad (7.89)$$

where $[S]$ is a strain tensor, $[T]$ is a stress tensor, $[E]$ is an electric field vector, $[D]$ is an electrical displacement vector, $[s^E]$ is a compliance tensor measured under constant electric field, $[\epsilon^T]$ is an electrical permittivity matrix measured under constant stress, and $[d]^T$ is a transposed piezoelectric coefficient tensor.

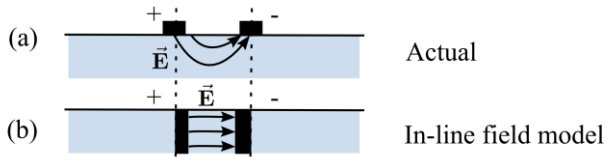

Figure 7.12: Cross-sectional view of the sense electrodes shows electric field patterns with Smith's IDT model (a) Actual field pattern (b) In-line field approximation [220].

Using the in-line field approximation (Figure 7.12), the electric field under the sense electrodes can be described by the relevant constitutive equations:

$$D_1 = d_{15}T_5 + \epsilon_1 E_1, \tag{7.90}$$

$$S_5 = s_{55}T_5 + d_{15}E_1. \tag{7.91}$$

From (7.91), the stress T_5 can be written as

$$T_5 = \frac{S_5 - d_{15}E_1}{s_{55}}. \tag{7.92}$$

Equations (7.90) and (7.91) can be solved by substituting T_5 into (7.90) given by

$$D_1 = \frac{d_{15}S_5}{s_{55}} + \epsilon_1 E_1 \left(1 - \frac{d_{15}^2}{\epsilon_1 s_{55}}\right). \tag{7.93}$$

From Figure 7.11, the sense electrode can be modeled as a parallel plate capacitor given by

$$\frac{Q}{A} = \frac{d_{15}S_5}{s_{55}} + \frac{\epsilon_1 V}{d}\left(1 - \frac{d_{15}^2}{\epsilon_1 s_{55}}\right), \tag{7.94}$$

where Q is the charge in the capacitor, A is the capacitor area, d is the capacitor gap, and V is the output voltage. The charge Q can be substituted by $Q = i/j\omega$ in the Fourier domain as

$$\frac{i}{j\omega} = \frac{Ad_{15}S_5}{s_{55}} + \frac{\epsilon_1 AV}{d}\left(1 - \frac{d_{15}^2}{\epsilon_1 s_{55}}\right). \tag{7.95}$$

If the sense electrode is connected to RC load with resistance R and capacitance C_L, the current can be substituted by voltage V given by

$$\frac{1}{j\omega}\left(-\frac{V}{R} - j\omega C_L V\right) = \frac{Ad_{15}S_5}{s_{55}} + \frac{\epsilon_1 AV}{d}\left(1 - \frac{d_{15}^2}{\epsilon_1 s_{55}}\right). \tag{7.96}$$

The output voltage V can be solved as

$$V = -\frac{\frac{Ad_{15}S_5}{s_{55}}}{\left(\frac{1}{j\omega R}\frac{1}{}+C_L+\frac{\epsilon_1 A}{d}\left(1-\frac{d_{15}^2}{\epsilon_1 s_{55}}\right)\right)}. \tag{7.97}$$

If the external capacitive and resistive load is negligible, the output voltage can be written as

$$V \approx -\frac{d_{15}}{s_{55}}\frac{d}{\epsilon_1}\frac{1}{\left(1-\frac{d_{15}^2}{\epsilon_1 s_{55}}\right)}S_5. \tag{7.98}$$

The strain S_5 can be written in the form of displacement as

$$V \approx -\frac{d_{15}}{s_{55}}\frac{d}{\epsilon_1}\frac{1}{\left(1-\frac{d_{15}^2}{\epsilon_1 s_{55}}\right)}u_{1,3}, \tag{7.99}$$

where $u_{1,3} = du_1/dx_3$, as previously explained. The generalized displacement u_1 can be written in terms of the shear horizontal wave generated by the Coriolis force u_{sh} given by

$$V \approx -\frac{d_{15}}{s_{55}}\frac{d}{\epsilon_1}\frac{1}{\left(1-\frac{d_{15}^2}{\epsilon_1 s_{55}}\right)}(jk_{sh1})u_{sh}, \tag{7.100}$$

where k_{sh1} is the wavevector of the shear horizontal wave in the x_1 direction. The wavevector k_{sh1} can be written in terms of the wavelength given by

$$V \approx -j\frac{d_{15}}{s_{55}}\frac{d}{\epsilon_1}\frac{1}{\left(1-\frac{d_{15}^2}{\epsilon_1 s_{55}}\right)}\frac{2\pi}{\lambda}\cos(\theta_s)u_{sh}. \tag{7.101}$$

From (7.101), the sensing coefficient Γ_{sense} defined in (7.68) can be written as

$$\Gamma_{sense} \approx -j\frac{d_{15}}{s_{55}}\frac{d}{\epsilon_1}\frac{1}{\left(1-\frac{d_{15}^2}{\epsilon_1 s_{55}}\right)}\frac{2\pi}{\lambda}\cos(\theta_s). \tag{7.102}$$

The sensing coefficient Γ_{sense} will be quantified in 7.5 and used to calculate the scale factor, as defined in (7.70).

7.5 Numerical results

Based on the model from the previous section (7.4), a bulk diffraction wave gyroscope geometry can be designed to optimize the gyroscope scale factor. From the detailed models in 7.4.1-7.4.6, the gyroscope scale factor in (7.70) can be calculated. The gyroscope is designed on 500-µm-thick Y-128 lithium niobate because of its high electromechanical coupling coefficient, high quality factor, and simple fabrication step. The substrate thickness of 500 µm is chosen because this thickness is commonly available.

In order to maximize gyroscope sensitivity, the angle of incidence θ_p is chosen to maximize the shear vertical wave generation due to mode conversion, as explained in 7.4.4. The shear wave reflection coefficient depends on the acoustic wave speed, as explained in (7.83). The acoustic wave speed can be calculated from the properties of lithium niobate obtained from [222]. The compliance tensor and piezoelectric coefficient tensor can be rotated by Bond transformation matrices [219]. The acoustic wave speed varies in different traveling directions due to anisotropy of lithium niobate.

To reduce the complexity, the angle of incidence is approximated as a small angle. The acoustic wave speed is approximately identical to the wave traveling in the x_1 direction, as shown in Table 7.1.

Table 7.1: Calculated acoustic wave speed in 128° Y lithium niobate.

Variables	**Travel direction**	**Polarization**	**Value**
P wave speed, v_p	x_3	x_3	7293 m/s
SV wave speed, v_s	x_3	x_2-x_3 *plane*	5052 m/s
SH wave speed, v_{sh}	x_3	x_1	4026 m/s

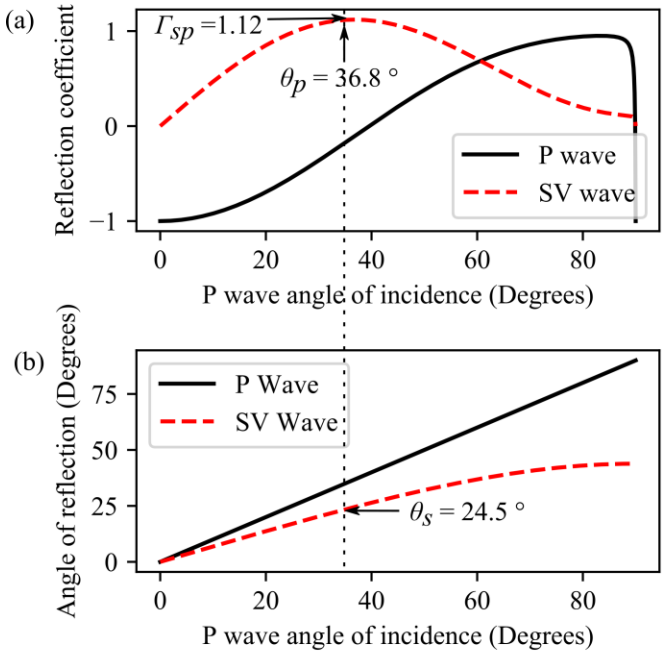

Figure 7.13: (a) Reflection coefficient of the P and S wave versus angle of incidence. (b) Angle of reflection versus angle of incidence.

From the acoustic wave speed in Table 7.1 and equations explained in 7.4.4, the reflection coefficient and angle of reflection are plotted in Figure 7.13. To maximize the gyroscope scale factor, the gyroscope operates to maximize the mode conversion to the shear wave at $\theta_p = 36.8\,°$, as shown in Figure 7.13a. This corresponds to the P to SV

wave reflection coefficient $\Gamma_{sp} = 1.12$ and the SV wave angle of reflection of $\theta_s = 24.5\,°$. The reflection coefficient Γ_{sp} is used to calculate the scale factor in (7.105).

From the geometry of the diffraction wave, explained in 7.4.3, the angle of incidence θ_p is equal to the diffraction angle of the traveling P wave, $u_{pi}(\theta_p)$. The diffraction angle is controlled by the drive electrode width w_d, and the operating frequency f, as explained in (7.80). From the P wave speed in Table 7.1 and θ_p in Figure 7.13a, the drive electrode width depends on the drive frequency given by

$$w_d = \frac{1.430}{\sin(\theta_p)} \frac{v_p}{f_p} = \frac{17{,}409\ \text{Hz·m}}{f_p} = \frac{17{,}409\ \text{MHz·μm}}{f_p}. \tag{7.103}$$

From (7.103), designing the gyroscope to be driven at high frequency results in a smaller drive electrode width, which leads to a smaller device size.

The operating frequency must match the resonance frequency of the HBAR, as explained in (7.72). From the P wave speed in Table 7.1, the HBAR resonance frequency for the substrate thickness of 500 μm is given by

$$f_p = n\frac{v_p}{2h} = n \times 7.29\ \text{MHz} \tag{7.104}$$

where n is the mode number. In order to be in the far-field region of the diffraction so that the traveling P wave is generated, the mode number should be high ($n \gg 1$), which means operating at high frequency.

Designing the gyroscope to be driven at high frequency results in a smaller device size, as explained in (7.103). However, operating at high frequency requires more complicated and expensive circuits. The gyroscope driving frequency and geometry are designed, as shown in Table 7.2. The design operated at the HBAR order of 16, which is high enough such that the diffraction is in the far-field. The HBAR order results in a gyroscope frequency of 116.68 MHz, which can be generated, read, and processed by

commercial CMOS integrated circuits. As stated in (7.103), the operating frequency results in a drive electrode width of 150 μm.

Table 7.2: Device geometry.

Variables	**Value**
Drive electrode width	150 μm
Drive electrode gap	150 μm
Gyroscope thickness, h	500 μm
Sense electrode width	150 μm
Sense electrode gap	150 μm
Driving frequency, f_d	116.68 MHz
HBAR order, n	16

From the gyroscope geometry given in Table 7.2, the P wave generation from the drive electrode (previously explained in 7.4.1) can be analyzed. The P wave generation coefficient Γ_{dp} is extracted for calculating the gyroscope scale factor in (7.105). The gyroscope is simulated by the Onscale finite element analysis software in 2D, as shown in Figure 7.14. The plain P wave is generated from drive+ and drive- electrodes in the opposite phase. The P wave generation coefficient, Γ_{dp} is extracted from the simulated results as $\Gamma_{dp} = 1.2$ pm/V.

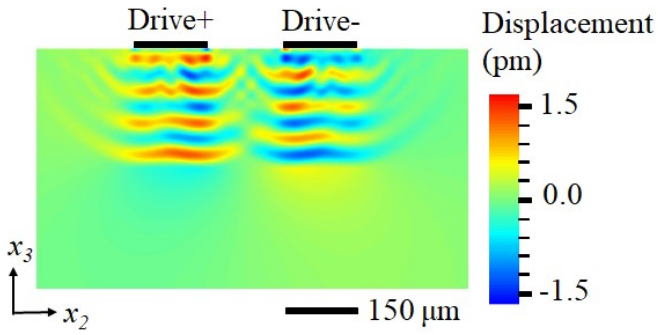

Figure 7.14 The P wave generated by the drive electrode is analyzed by Onscale FEA software.

The parameters used to calculate the gyroscope scale factor are concluded in Table 4.1. The drive voltage is chosen at 1 V_p and the P wave generation coefficient,

Γ_{dp} is extracted from the simulation in Figure 7.14. The quality factor Q_p is measured in Chapter 6. Other parameters are previously calculated in the equation in the table. From, Table 4.1, the gyroscope scale factor Γ_{BDWG} can be calculated:

$$\text{Scale factor} = V_d \Gamma_{dp} Q_p \Gamma_{diff} \Gamma_{sp} \Gamma_{\Omega} \Gamma_{sense} = 7.31\ \mu\text{V}/\left(\frac{\text{deg}}{\text{s}}\right). \quad (7.105)$$

The calculated gyroscope scale factor, without gain of an electronic amplifier, is $7.31\ \mu\text{V}/(\text{deg}/\text{s})$, which is one of the largest scale factors reported for a solidly mounted gyroscope (Table 6.1).

Table 7.3: Variables for calculating gyroscope scale factor.

Variables	**Definition**	**Expression**	**Value**
Drive voltage, V_d	-	chosen	1 V_p
P wave generation coefficient, Γ_{dp}	(7.63)	Figure 7.14	1.2 pm/V
Quality factor, Q_p	-	Chapter 6	55,000
Diffraction wave coefficient, Γ_{diff}	(7.65)	(7.79)	0.217
P to SV wave reflection coefficient, Γ_{sp}	(7.66)	(7.83)	1.121
Rotation coefficient, Γ_{Ω}	(7.67)	(7.88)	$1.898\text{x}10^{-9}$ $(\text{deg/s})^{-1}$
Sensing coefficient, Γ_{sense}	(7.68)	(7.102)	0.261 V/pm

Table 7.4: Comparison of other solidly mounted gyroscopes and this work.

Solidly mounted gyroscope	**Technology**	**Frequency**	**Scale factor**
Ref [39]	SAW	80 MHz	3.2 μV/(deg/s)
Ref [189]	SAW	115 MHz	0.96 μV/(deg/s)
Ref [209]	Thickness shear	647 kHz	0.75 μV/(deg/s)
Ref [212]	Thickness shear	1.1 MHz	12.5 nV/(deg/s)
This work (Theory, Chapter 7)	High-overtone bulk diffraction wave gyroscope	116 MHz	7.31 μV/(deg/s)
This work (Experiment, Chapter 6)	High-overtone bulk diffraction wave gyroscope	164 MHz	191 μV/(deg/s)

7.6 Discussions and conclusion

A new type of gyroscopic mechanism using high-overtone bulk diffraction wave is presented. The gyroscope measures rotation rate from polarization rotation of the shear wave generated by diffraction wave leaking from high-overtone bulk acoustic resonator. The gyroscope has high shock-tolerance due to the lack of released structures. This chapter focuses on a design using a lithium niobate substrate; however, the gyroscope principle can be designed for a thin film AlN, which is compatible with CMOS integration [223], [224].

The analysis of the gyroscope is based on several approximations, which comprise of 1) a Crossed field model of the drive electrode 2) a 1D model of the high-overtone bulk acoustic resonator 3) a far-field approximation for the diffraction 4) a small angle approximation for the mode conversion 5) an in-line field model for the sense electrode. These approximations potentially cause discrepancies between the scale factor estimated in this chapter and the experimental results in Chapter 6. The gyroscope models and analysis in each section should be further investigated and verified by experiments.

APPENDIX A

PRINTED CIRCUIT BOARD

A.1 IMU calibration stage control board (Chapter 4)

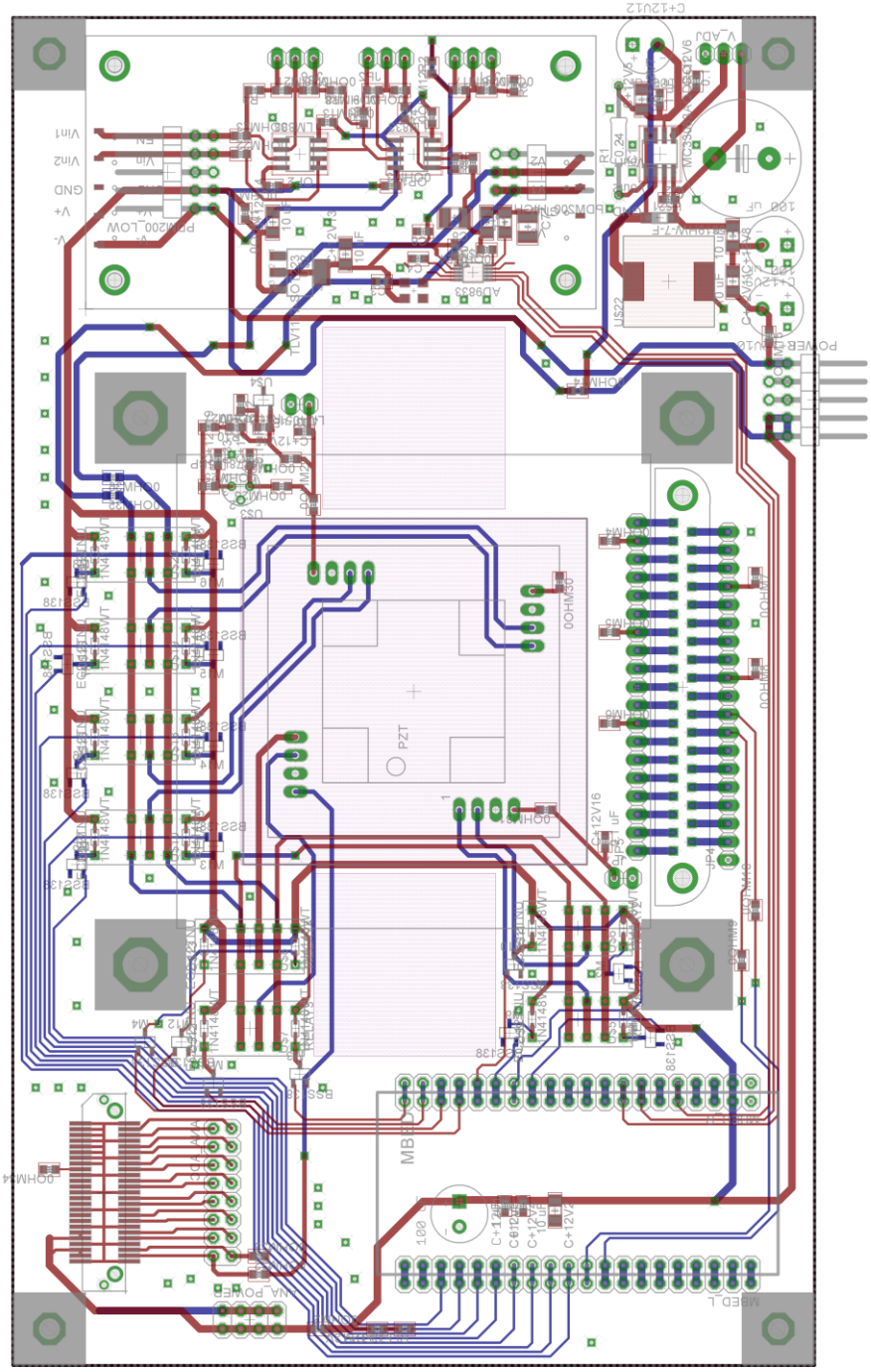

Figure A.1: Layout of the control board for IMU calibration.

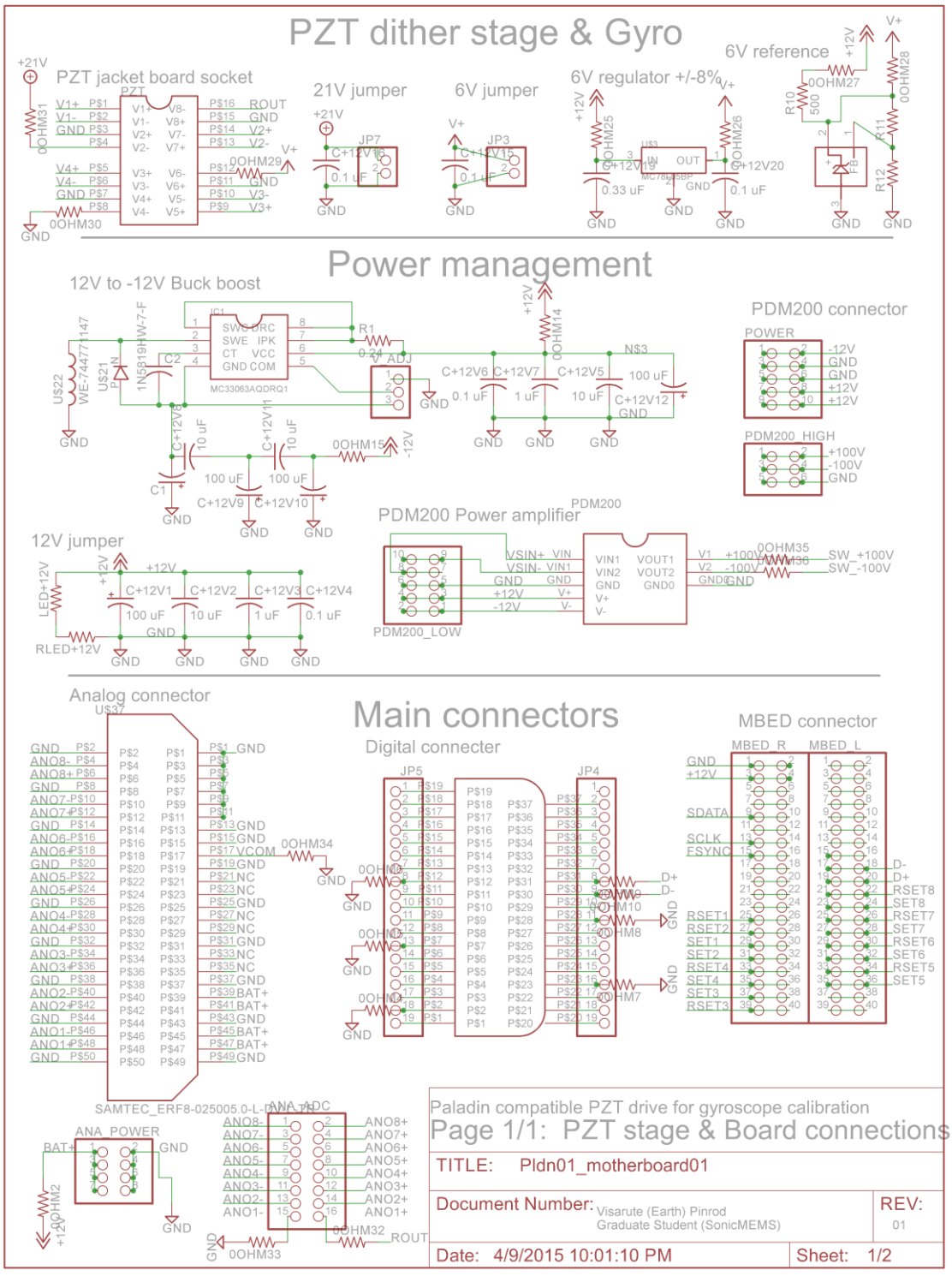

Figure A.2: Schematic of the control board for IMU calibration (Page 1/2).

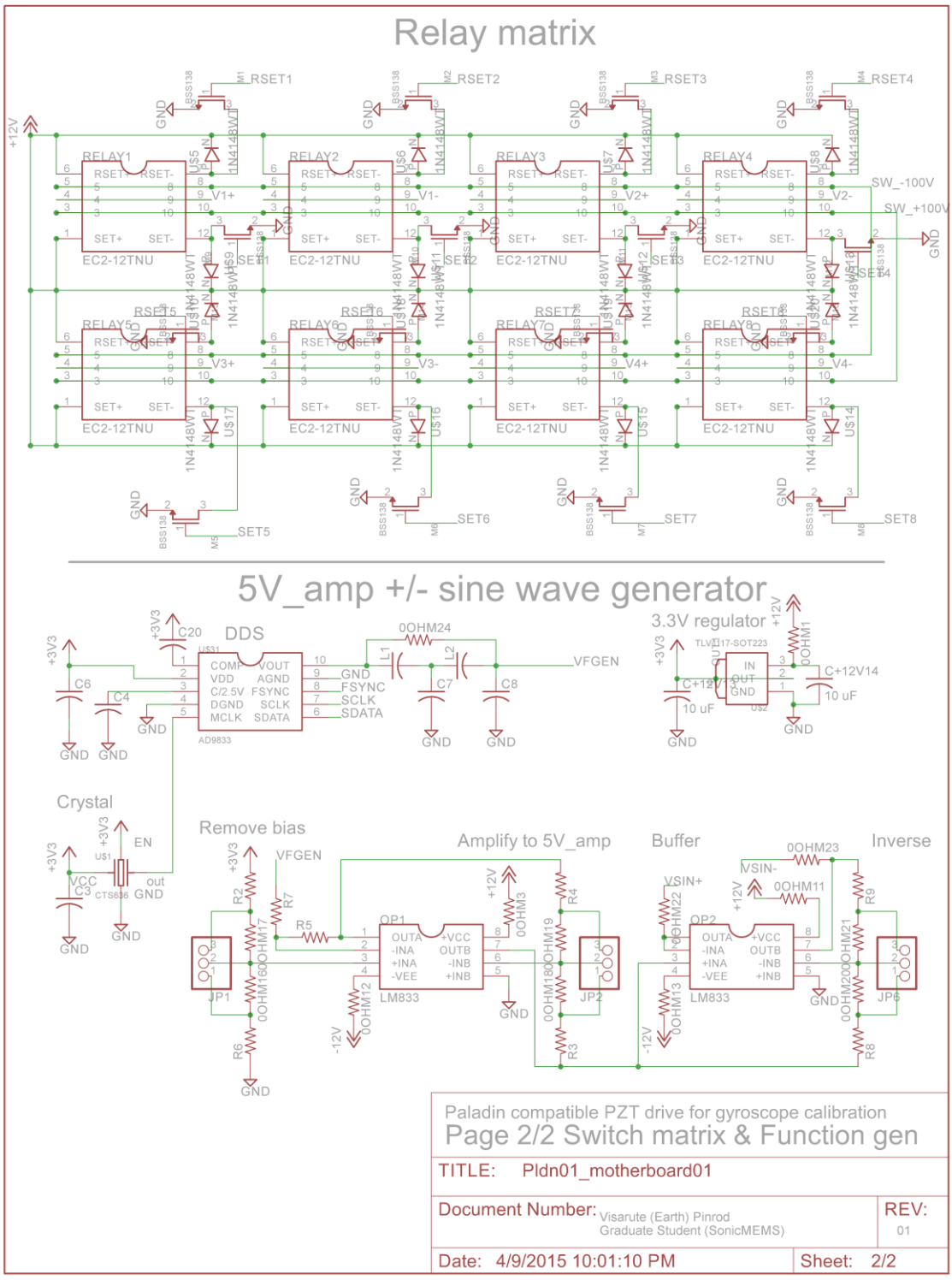

Figure A.3: Schematic of the control board for IMU calibration (Page 2/2).

Table A.1: The purpose and part numbers of the components used in the control board for IMU calibration.

Quantity	Part	Manufacturer	Part number
1	PZT stage board	In-house	-
1	Microcontroller	NXP	LPC1768
2	High voltage amplifier	PiezoDrive	PDM200
	Relays		
8	Relay	KEMET	EC2-12TNU
16	Relay diode	ON Semiconductor	1N4148WT
16	Relay transistor	ON Semiconductor	BSS138
	Connectors		
1	Digital connector	Cannon	MDM-37SBSP
1	Analog connector	Samtec	ERF8-025005.0-L-DV-L-TR
15	Pin headers	Various	Various
	Sine wave generator		
1	Sine wave generator IC	Analog device	AD9833
1	Crystal oscillator	CTS electronics	CTS636
2	OPAMP	Texas Instrument	LM833
	Power management		
1	Switching regulator	On semiconductor	MC33063AQDRQ1
1	Inductor	Wurth Elektronik	WE-744771147
1	Diode	Diodes Incorporated	1N5819HW-7-F
1	6V reference	Texas Instrument	LM4051
1	6V linear regulator	Micro Commercial Co	MC78L05BP
1	3.3V linear regulator	Texas Instrument	TLV1117-SOT223
	Miscellaneous		
28	Capacitors	Various	Various
50	Resistors	Various	Various

REFERENCES

[1] J. A. Stankovic, "Research directions for the internet of things," *IEEE Internet Things J.*, 2014.

[2] A. Zanella, N. Bui, A. Castellani, L. Vangelista, and M. Zorzi, "Internet of things for smart cities," *IEEE Internet Things J.*, 2014.

[3] O. B. Akan, O. Cetinkaya, C. Koca, and M. Ozger, "Internet of Hybrid Energy Harvesting Things," *IEEE Internet Things J.*, 2018.

[4] Gartner Inc, "Gartner Identifies Top 10 Strategic IoT Technologies and Trends," 2018. [Online]. Available: https://www.gartner.com/en/newsroom/press-releases/2018-11-07-gartner-identifies-top-10-strategic-iot-technologies-and-trends. [Accessed: 08-Jun-2019].

[5] S. Tadigadapa and K. Mateti, "Piezoelectric MEMS sensors: State-of-the-art and perspectives," *Meas. Sci. Technol.*, 2009.

[6] J. Tichý, J. Erhart, E. Kittinger, and J. Přívratská, *Fundamentals of piezoelectric sensorics: Mechanical, dielectric, and thermodynamical properties of piezoelectric materials*. 2010.

[7] H. Bhugra and G. Piazza, *Piezoelectric MEMS Resonators*. Switzerland, 2017.

[8] V. Kaajakari, *Practical MEMS: Design of microsystems, accelerometers, gyroscopes, RF MEMS, optical MEMS, and microfluidic systems*. Las Vegas, NV, USA: Small Gear Pub, 2009.

[9] J. Silva *et al.*, "MEMS-based Low SWaP Solutions for Multi/Hyperspectral Infrared Sensing and Imaging," in *2018 IEEE Research and Applications of Photonics In Defense Conference (RAPID)*, 2018, pp. 1–4.

[10] H. Jeong, J. Jeong, D. S. Lee, C. J. Stanton, and Y. D. Jho, "Generation and Frequency Control of THz Waves by Nanoscale Piezo-Engineering," 2013.

[11] APC International, "Physical and Piezoelectric Properties | APC International."

[Online]. Available: https://www.americanpiezo.com/apc-materials/physical-piezoelectric-properties.html. [Accessed: 15-Jul-2019].

[12] R. W. Johnstone and M. Parameswaran, *An Introduction to Surface-Micromachining*. Norwell, MA, USA, MA, USA: Kluwer Academic Publishers, 2004.

[13] S. Nadig, "Monolithic Bulk Piezoelectric Lateral Bimorph Transducers and Applications To Inertial Sensor Calibration Stages, Gyroscopes, Ultrasonic Motors and Energy Harvesters," Cornell University, 2017.

[14] S. F. B. Morse, "Improvement in the Mode of Communicating Information by Signals by the Application of Electro-magnetism," US1647A, 1840.

[15] Lybarger and S. F, "Magnetic Microphone," US2552800A, 1947.

[16] D. P. Arnold and N. Wang, "Permanent magnets for MEMS," *J. Microelectromechanical Syst.*, 2009.

[17] G. Gautschi, *Piezoelectric Sensorics*. 2002.

[18] A. A. Vives, *Piezoelectric transducers and applications*. 2008.

[19] J. Curie and P. Curie, "Développement par compression de l'électricité polaire dans les cristaux hémièdres à faces inclinées," *Bull. la Société minéralogique Fr.*, vol. 3, no. 4, pp. 90–93, 1880.

[20] H. Zhu *et al.*, "Observation of piezoelectricity in free-standing monolayer MoS 2," *Nat. Nanotechnol.*, 2015.

[21] K. A. N. Duerloo, M. T. Ong, and E. J. Reed, "Intrinsic piezoelectricity in two-dimensional materials," *J. Phys. Chem. Lett.*, 2012.

[22] C. Cui, F. Xue, W.-J. Hu, and L.-J. Li, "Two-dimensional materials with piezoelectric and ferroelectric functionalities," *npj 2D Mater. Appl.*, 2018.

[23] W. P. Mason, "Piezoelectricity, its history and applications," *J. Acoust. Soc. Am.*,

1981.

[24] W. P. Mason, “Theory of the Ferroelectric Effect and Clamped Dielectric Constant of Rochelle Salt,” *Phys. Rev.*, vol. 72, no. 9, pp. 854–865, Nov. 1947.

[25] G. H. Haertling, “Ferroelectric Ceramics: History and Technology,” *J. Am. Ceram. Soc.*, vol. 82, no. 4, pp. 797–818, Apr. 1999.

[26] S. Fujishima, “The history of ceramic filters,” *IEEE Trans. Ultrason. Ferroelectr. Freq. Control*, vol. 47, no. 1, pp. 1–7, Jan. 2000.

[27] S. Roberts, “Dielectric and Piezoelectric Properties of Barium Titanate,” *Phys. Rev.*, vol. 71, no. 12, pp. 890–895, Jun. 1947.

[28] R. B. Gray, “Transducer and method of making the same,” US2486560A, 20-Sep-1946.

[29] J. Bernard, “Piezoelectric transducers using lead titanate and lead zirconate,” US2708244A, 24-Mar-1954.

[30] A. A. BALLMAN, “Growth of Piezoelectric and Ferroelectric Materials by the CzochraIski Technique,” *J. Am. Ceram. Soc.*, vol. 48, no. 2, pp. 112–113, Feb. 1965.

[31] H. Kawai, “The Piezoelectricity of Poly (vinylidene Fluoride),” *Jpn. J. Appl. Phys.*, vol. 8, no. 7, pp. 975–976, Jul. 1969.

[32] A. Omairi, Z. H. Ismail, K. A. Danapalasingam, and M. Ibrahim, “Power Harvesting in Wireless Sensor Networks and Its Adaptation with Maximum Power Point Tracking: Current Technology and Future Directions,” *IEEE Internet Things J.*, 2017.

[33] S. Roundy, P. K. Wright, and J. M. Rabaey, *Energy Scavenging for Wireless Sensor Networks: with Special Focus on Vibrations*. 2004.

[34] P. D. Groves, *Principles of GNSS, Inertial, and Multisensor Integrated Navigation Systems*. Artech House, 2013.

[35] Z. Sun and I. F. Akyildiz, “Magnetic induction communications for wireless underground sensor networks,” *IEEE Trans. Antennas Propag.*, 2010.

[36] M. C. Domingo, “Magnetic induction for underwater wireless communication networks,” *IEEE Trans. Antennas Propag.*, 2012.

[37] S. C. Lin, A. A. Alshehri, P. Wang, and I. F. Akyildiz, “Magnetic Induction-Based Localization in Randomly Deployed Wireless Underground Sensor Networks,” *IEEE Internet Things J.*, 2017.

[38] A. K. Sharma *et al.*, “Magnetic Induction-Based Non-Conventional Media Communications: A Review,” *IEEE Sens. J.*, 2017.

[39] W. Wang, H. Oh, K. Lee, S. Yoon, and S. Yang, “Enhanced sensitivity of novel surface acoustic wave microelectromechanical system-interdigital transducer gyroscope,” *Jpn. J. Appl. Phys.*, 2009.

[40] L. Da Xu, W. He, and S. Li, “Internet of things in industries: A survey,” *IEEE Transactions on Industrial Informatics*. 2014.

[41] B. S. Cook *et al.*, “RFID-based sensors for zero-power autonomous wireless sensor networks,” *IEEE Sens. J.*, 2014.

[42] R. H. Olsson, R. B. Bogoslovov, and C. Gordon, “Event driven persistent sensing: Overcoming the energy and lifetime limitations in unattended wireless sensors,” in *Proceedings of IEEE Sensors*, 2017.

[43] R. W. Reger *et al.*, “Near-zero power accelerometer wakeup system,” in *2017 IEEE SENSORS*, 2017, pp. 1–3.

[44] S. K. Gupta, V. Pinrod, S. Nadig, B. Davaji, and A. Lal, “Vibration Powered RF-Transponder for Sensing Low Frequency Motion Events,” in *Journal of Physics: Conference Series*, 2016.

[45] V. Rajaram, Z. Qian, S. Kang, N. E. McGruer, and M. Rinaldi, “MEMS-based near-zero power infrared wireless sensor node,” in *2018 IEEE Micro Electro Mechanical Systems (MEMS)*, 2018, pp. 17–20.

[46] D. G. Stork and P. R. Gill, “Special-purpose optics to reduce power dissipation in computational sensing and imaging systems,” in *2017 IEEE SENSORS*, 2017, pp. 1–3.

[47] T. Wu *et al.*, “Design and fabrication of AlN RF MEMS switch for near-zero power RF wake-up receivers,” in *Proceedings of IEEE Sensors*, 2017.

[48] L. Colombo *et al.*, “Ultra-low-power and high sensitivity resonant micromechanical receiver,” in *Proceedings of IEEE Sensors*, 2017.

[49] P. Bassirian *et al.*, “A passive 461 MHz AlN-CMOS RF front-end for event-driven wakeup receivers,” in *Proceedings of IEEE Sensors*, 2017.

[50] A. K. Vutha, B. Davaji, C. H. Lee, and G. M. Walker, “A microfluidic device for thermal particle detection,” *Microfluid. Nanofluidics*, 2014.

[51] B. Davaji and C. H. Lee, “A paper-based calorimetric microfluidics platform for bio-chemical sensing,” *Biosens. Bioelectron.*, 2014.

[52] V. Pinrod *et al.*, “Zero-power sensors with near-zero-power wakeup switches for reliable sensor platforms,” in *Proceedings of the IEEE International Conference on Micro Electro Mechanical Systems (MEMS)*, 2017.

[53] V. Pinrod, A. Ruyack, R. Ying, B. Davaji, A. Molnar, and A. Lal, “PZT lateral bimorph based sensor cuboid for near zero power sensor nodes,” in *Proceedings of IEEE Sensors*, 2017.

[54] S. Jeong *et al.*, “Always-On 12-nW Acoustic Sensing and Object Recognition Microsystem for Unattended Ground Sensor Nodes,” *IEEE J. Solid-State Circuits*, 2018.

[55] Y. Kusano, J. Segovia-Fernandez, S. Sonmezoglu, R. Amirtharajah, and D. A. Horsley, “Frequency selective MEMS microphone based on a bioinspired spiral-shaped acoustic resonator,” in *TRANSDUCERS 2017 - 19th International Conference on Solid-State Sensors, Actuators and Microsystems*, 2017.

[56] L. Baumgartel, A. Vafanejad, S. J. Chen, and E. S. Kim, “Resonance-enhanced piezoelectric microphone array for broadband or prefiltered acoustic sensing,” *J.*

Microelectromechanical Syst., 2013.

[57] Y. Zhang *et al.*, "Development of a biologically inspired MEMS microphone," in *Proceedings of IEEE Sensors*, 2017.

[58] R. W. Reger, P. J. Clews, G. M. Bryan, C. A. Keane, M. D. Henry, and B. A. Griffin, "Aluminum nitride piezoelectric microphones as zero-power passive acoustic filters," in *TRANSDUCERS 2017 - 19th International Conference on Solid-State Sensors, Actuators and Microsystems*, 2017.

[59] V. Pinrod *et al.*, "Zero Power, Tunable Resonant Microphone with Nanowatt Classifier for Wake-Up Sensing," in *2018 IEEE SENSORS*, 2018, pp. 1–4.

[60] S. Nadig, S. Ardanuc, and A. Lal, "Planar laser-micro machined bulk PZT bimorph for in-plane actuation," in *2013 Joint IEEE International Symposium on Applications of Ferroelectric and Workshop on Piezoresponse Force Microscopy, ISAF/PFM 2013*, 2013.

[61] S. Nadig, V. Pinrod, S. Ardanuc, and A. Lal, "Multi-modal mechanical stimuli stage for in-situ calibration of MEMS gyroscopes," in *2nd IEEE International Symposium on Inertial Sensors and Systems, IEEE ISISS 2015 - Proceedings*, 2015.

[62] V. Pinrod, S. Nadig, B. Davaji, and A. Lal, "3-axis MEMS gyroscope calibration stage: Magnetic actuation enabled out-of-plane dither for piezoelectric in-plane calibration," in *4th IEEE International Symposium on Inertial Sensors and Systems, INERTIAL 2017 - Proceedings*, 2017.

[63] K. Amponsah, N. Yoshimizu, S. Ardanuc, and A. Lal, "Near-kT switching-energy lateral NEMS switch," in *2010 IEEE 5th International Conference on Nano/Micro Engineered and Molecular Systems, NEMS 2010*, 2010.

[64] X. Yue *et al.*, "Development of an Indoor Photovoltaic Energy Harvesting Module for Autonomous Sensors in Building Air Quality Applications," *IEEE Internet Things J.*, 2017.

[65] J. J. Bernstein *et al.*, "Resonant Acoustic MEMS Wake-Up Switch," *J. Microelectromechanical Syst.*, 2018.

[66] S. Tin *et al.*, "N-Zero Integrated Analog Classifier (NINA)," in *GOMACTech Conference*, 2017.

[67] A. Ruyack, B. Davaji, L. Pancoast, N. Shalabi, A. Molnar, and A. Lal, "NEMS elecctrostatic resonant near-zero power resistive contact RF wake-up switch with Pt FIB contact," in *IEEE MEMS*, 2019.

[68] P. H. P. Wang *et al.*, "A Near-Zero-Power Wake-Up Receiver Achieving -69-dBm Sensitivity," *IEEE J. Solid-State Circuits*, 2018.

[69] J. Moody *et al.*, "An 8.3 nW -72 dBm Event Driven IoE Wake up Receiver RF Front End," in *EuMIC 2017*, 2017.

[70] S. Bdiri, F. Derbel, and O. Kanoun, "An 868 MHz 7.5ĝW wake-up receiver with-60 dBm sensitivity," *J. Sensors Sens. Syst.*, 2016.

[71] W. A. Vitale, M. Fernandez-Bolanos, A. Bazigos, C. Dehollain, and A. M. Ionescu, "RF MEMS power sensors for ultra-low power wake-up circuit applications," in *2013 Proceedings of the European Solid-State Device Research Conference (ESSDERC)*, 2013, pp. 288–291.

[72] B. Jiang, K. P. Fishkin, S. Roy, and M. Philipose, "Unobtrusive long-range detection of passive RFID tag motion," *IEEE Trans. Instrum. Meas.*, 2006.

[73] C. He, M. E. Kiziroglou, D. C. Yates, and E. M. Yeatman, "A MEMS self-powered sensor and RF transmission platform for WSN nodes," *IEEE Sens. J.*, 2011.

[74] H. Jiang, M. E. Kiziroglou, D. C. Yates, and E. M. Yeatman, "A motion-powered piezoelectric pulse generator for wireless sensing via FM transmission," *IEEE Internet Things J.*, 2015.

[75] L. M. Miller, E. Halvorsen, T. Dong, and P. K. Wright, "Modeling and experimental verification of low-frequency MEMS energy harvesting from ambient vibrations," *J. Micromechanics Microengineering*, 2011.

[76] Q. He and T. Jiang, "Complementary multi-mode low-frequency vibration energy harvesting with chiral piezoelectric structure," *Appl. Phys. Lett.*, 2017.

[77] I. H. Kim, H. J. Jung, B. M. Lee, and S. J. Jang, “Broadband energy-harvesting using a two degree-of-freedom vibrating body,” *Appl. Phys. Lett.*, 2011.

[78] M. S. M. Soliman, E. M. Abdel-Rahman, E. F. El-Saadany, and R. R. Mansour, “A design procedure for wideband micropower generators,” *J. Microelectromechanical Syst.*, 2009.

[79] H. Liu, C. Lee, T. Kobayashi, C. J. Tay, and C. Quan, “Investigation of a MEMS piezoelectric energy harvester system with a frequency-widened-bandwidth mechanism introduced by mechanical stoppers,” *Smart Mater. Struct.*, 2012.

[80] P. Constantinou and S. Roy, “A 3D printed electromagnetic nonlinear vibration energy harvester,” *Smart Mater. Struct.*, vol. 25, no. 9, p. 095053, Sep. 2016.

[81] P. Pillatsch, L. M. Miller, E. Halvorsen, P. K. Wright, E. M. Yeatman, and A. S. Holmes, “Self-tuning behavior of a clamped-clamped beam with sliding proof mass for broadband energy harvesting,” in *Journal of Physics: Conference Series*, 2013.

[82] X. Wu and D. W. Lee, “A high-efficient broadband energy harvester based on non-contact coupling technique for ambient vibrations,” in *2015 28th IEEE International Conference on Micro Electro Mechanical Systems (MEMS)*, 2015, pp. 1110–1113.

[83] E. Baker, T. Reissman, F. Zhou, C. Wang, K. Lynch, and C. Sun, “Microstereolithography of Three-Dimensional Polymeric Springs for Vibration Energy Harvesting,” *Smart Mater. Res.*, 2012.

[84] M. Dawoud, I. Taha, and S. J. Ebeid, “Mechanical behaviour of ABS: An experimental study using FDM and injection moulding techniques,” *J. Manuf. Process.*, vol. 21, pp. 39–45, Jan. 2016.

[85] S. Nadig, S. Ardanuc, and A. Lal, “Monolithic 2-axis in-plane PZT lateral bimorph energy harvester with differential output,” in *Proceedings of the IEEE International Conference on Micro Electro Mechanical Systems (MEMS)*, 2015.

[86] C. Ou, V. Pinrod, B. Davaji, and A. Lal, “Omnidirectional Low Frequency Energy Harvester for Wearable Applications,” in *2018 PowerMEMS*, 2018.

[87] S. Nadig, S. Aggrawal, and A. Lal, “PZT lateral bimorph array stator based ultrasonic micromotor,” in *IEEE International Ultrasonics Symposium, IUS*, 2017.

[88] V. Pinrod, S. Nadig, S. Ardanuc, and A. Lal, “Piezoelectric micro dither stage calibration of 6-axis IMU,” in *Proceedings of the IEEE International Conference on Micro Electro Mechanical Systems (MEMS)*, 2016.

[89] A. Lozano-Nieto, *RFID design fundamentals and applications*. Boca Raton, FL: CRC Press, 2011.

[90] A. Narimani, M. F. Golnaraghi, and G. N. Jazar, “Frequency response of a piecewise linear vibration isolator,” *JVC/Journal Vib. Control*, 2004.

[91] K. H. Matlack, A. Bauhofer, S. Krödel, A. Palermo, and C. Daraio, “Composite 3D-printed metastructures for low-frequency and broadband vibration absorption.,” *Proc. Natl. Acad. Sci. U. S. A.*, vol. 113, no. 30, pp. 8386–90, Jul. 2016.

[92] Honda Motor Company, “Owner’s Manual Generator EZ3500-EZ5000,” 2002.

[93] P. Trautman, J. Ma, R. M. Murray, and A. Krause, “Robot navigation in dense human crowds: Statistical models and experimental studies of human–robot cooperation,” *Int. J. Rob. Res.*, vol. 34, no. 3, pp. 335–356, Mar. 2015.

[94] Y.-P. Huang, L. Sithole, and T.-T. Lee, “Structure From Motion Technique for Scene Detection Using Autonomous Drone Navigation,” *IEEE Trans. Syst. Man, Cybern. Syst.*, pp. 1–12, 2017.

[95] Q. Luo, Y. Cao, J. Liu, and A. Benslimane, “Localization and Navigation in Autonomous Driving: Threats and Countermeasures,” *IEEE Wirel. Commun.*, vol. 26, no. 4, pp. 38–45, Aug. 2019.

[96] J.-C. Juang and Y.-H. Chen, “Accounting for data intermittency in a software gnss receiver,” *IEEE Trans. Consum. Electron.*, vol. 55, no. 2, pp. 327–333, May 2009.

[97] B. Van den Bergh and S. Pollin, “Keeping UAVs Under Control During GPS

Jamming," *IEEE Syst. J.*, vol. 13, no. 2, pp. 2010–2021, Jun. 2019.

[98] J. Bird and D. Arden, "Indoor navigation with foot-mounted strapdown inertial navigation and magnetic sensors [Emerging Opportunities for Localization and Tracking]," *IEEE Wirel. Commun.*, vol. 18, no. 2, pp. 28–35, Apr. 2011.

[99] O. Hegrenas, E. Berglund, and O. Hallingstad, "Model-aided inertial navigation for underwater vehicles," in *2008 IEEE International Conference on Robotics and Automation*, 2008, pp. 1069–1076.

[100] S. Scheding, G. Dissanayake, E. M. Nebot, and H. Durrant-Whyte, "An experiment in autonomous navigation of an underground mining vehicle," *IEEE Trans. Robot. Autom.*, vol. 15, no. 1, pp. 85–95, 1999.

[101] J. L. Crassidis, "Sigma-point Kalman filtering for integrated GPS and inertial navigation," *IEEE Trans. Aerosp. Electron. Syst.*, vol. 42, no. 2, pp. 750–756, Apr. 2006.

[102] W. Quan, J. Li, X. Gong, and J. Fang, *INS/CNS/GNSS integrated navigation technology*. 2015.

[103] Analog Devices, "ADIS16497 Datasheet Tactical Grade, Six Degrees of Freedom Inertial Sensor." [Online]. Available: https://www.analog.com/media/en/technical-documentation/data-sheets/ADIS16497.pdf. [Accessed: 28-Aug-2019].

[104] Honeywell, "HG4930 INERTIAL MEASUREMENT UNIT (IMU) Performance and Environmental Information," 2017. [Online]. Available: https://media.digikey.com/pdf/Data Sheets/Honeywell PDFs/HG4930_PerfandEnvrioManual_Jul2017.pdf. [Accessed: 28-Aug-2019].

[105] Honeywell, "HG9900 Inertial Measurement Unit," 2018. [Online]. Available: https://aerospace.honeywell.com/en/~/media/aerospace/files/brochures/n61-1638-000-000-hg9900inertialmeasurementunit-bro.pdf. [Accessed: 28-Aug-2019].

[106] DigiKey Electronics, "DigiKey Electronics - Electronic Components Distributor." [Online]. Available: https://www.digikey.com/. [Accessed: 28-Aug-2019].

[107] VectorNav Technologies, “Inertial Measurement Units and Inertial Navigation.” [Online]. Available: https://www.vectornav.com/support/library/imu-and-ins. [Accessed: 28-Aug-2019].

[108] C. Acar and A. Shkel, *MEMS vibratory gyroscopes: structural approaches to improve robustness*. 2008.

[109] Hao Luo, G. Fedder, and L. R. Carley, “Integrated multiple-device IMU system with continuous-time sensing circuitry,” in *2003 IEEE International Solid-State Circuits Conference*, 2003, pp. 204–205.

[110] F. Ayazi, “Multi-DOF inertial MEMS: From gaming to dead reckoning,” in *2011 16th International Solid-State Sensors, Actuators and Microsystems Conference, TRANSDUCERS’11*, 2011.

[111] B. Cardani, “Optical image stabilization for digital cameras,” *IEEE Control Systems*. 2006.

[112] STMicroelectronics NV, “LSM6DSOX Datasheet,” 2019.

[113] Bosch Sensortec GmbH, “BMI160 Datasheet,” 2018.

[114] TDK Invensense Corporation, “ICM-42605 Datasheet,” San Jose, CA, USA, 2019.

[115] A. Olivares, G. Olivares, J. M. Górriz, and J. Ramírez, “High-efficiency low-cost accelerometer-aided gyroscope calibration,” in *Proceedings of the International Symposium on Test and Measurement*, 2009.

[116] A. A. Trusov, I. P. Prikhodko, D. M. Rozelle, A. D. Meyer, and A. M. Shkel, “1 PPM precision self-calibration of scale factor in MEMS Coriolis vibratory gyroscopes,” in *2013 Transducers and Eurosensors XXVII: The 17th International Conference on Solid-State Sensors, Actuators and Microsystems, TRANSDUCERS and EUROSENSORS 2013*, 2013.

[117] T. Olbrich, A. Richardson, W. Vermeiren, and B. Straube, “Integrating testability into microsystems,” *Microsyst. Technol.*, 1997.

[118] A. Norouzpour-Shirazi and F. Ayazi, “A Dual-Mode Actuation and Sensing Scheme for In-Run Calibration of Bias and Scale Factor Errors in Axisymmetric Resonant Gyroscopes,” *IEEE Sens. J.*, 2018.

[119] A. Norouzpour-Shirazi, “ADVANCED INTERFACE SYSTEMS FOR READOUT, CONTROL, AND SELF-CALIBRATION OF MEMS RESONANT GYROSCOPES,” Georgia Institute of Technology, 2016.

[120] G. K. Balachandran, V. P. Petkov, T. Mayer, and T. Balslink, “A 3-axis gyroscope for electronic stability control with continuous self-test,” *IEEE J. Solid-State Circuits*, 2016.

[121] W. T. Fong, S. K. Ong, and A. Y. C. Nee, “Methods for in-field user calibration of an inertial measurement unit without external equipment,” *Meas. Sci. Technol.*, 2008.

[122] S. You and U. Neumann, “Fusion of vision and gyro tracking for robust augmented reality registration,” 2002.

[123] J. Georgy, A. Noureldin, M. J. Korenberg, and M. M. Bayoumi, “Modeling the stochastic drift of a MEMS-based gyroscope in gyro/odometer/GPS integrated navigation,” *IEEE Trans. Intell. Transp. Syst.*, 2010.

[124] T. C. Dong-Si and A. I. Mourikis, “Estimator initialization in vision-aided inertial navigation with unknown camera-IMU calibration,” in *IEEE International Conference on Intelligent Robots and Systems*, 2012.

[125] S. Sukkarieh, E. M. Nebot, and H. F. Durrant-Whyte, “A high integrity IMU/GPS navigation loop for autonomous land vehicle applications,” *IEEE Trans. Robot. Autom.*, 1999.

[126] M. Tanigawa, H. Luinge, L. Schipper, and P. Slycke, “Drift-free dynamic height sensor using MEMS IMU aided by MEMS pressure sensor,” in *5th Workshop on Positioning, Navigation and Communication 2008, WPNC’08*, 2008.

[127] E. E. Aktakka, J. K. Woo, and K. Najafi, “On-chip characterization of scale-factor of a MEMS gyroscope via a micro calibration platform,” in *4th IEEE International Symposium on Inertial Sensors and Systems, INERTIAL 2017 - Proceedings*, 2017.

[128] Y. Chen, E. E. Aktakka, J. K. Woo, K. Najafi, and K. R. Oldham, "On-chip capacitive sensing and tilting motion estimation of a micro-stage for in situ MEMS gyroscope calibration," *Mechatronics*, 2018.

[129] E. E. Aktakka and K. Najafi, "A six-axis micro platform for in situ calibration of MEMS inertial sensors," in *Proceedings of the IEEE International Conference on Micro Electro Mechanical Systems (MEMS)*, 2016.

[130] E. E. Aktakka, J. K. Woo, D. Egert, R. J. M. Gordenker, and K. Najafi, "A microactuation and sensing platform with active lockdown for in situ calibration of scale factor drifts in dual-axis gyroscopes," *IEEE/ASME Trans. Mechatronics*, 2015.

[131] Y. Chen *et al.*, "An integrated opto-mechatronic system for self-calibration of accelerometer in large dynamic range," *Sensors Actuators A Phys.*, p. 111612, Sep. 2019.

[132] K. Papafotis and P. P. Sotiriadis, "MAG.I.C.AL.–A Unified Methodology for Magnetic and Inertial Sensors Calibration and Alignment," *IEEE Sens. J.*, vol. 19, no. 18, pp. 8241–8251, Sep. 2019.

[133] F. Qin *et al.*, "Integrated piezoelectric micromechanical vibration platform for six degree of freedom motion," *J. Micromechanics Microengineering*, 2019.

[134] F. Qin *et al.*, "High acceleration and angular velocity micro vibrating platform with IMU integration," *Sensors Actuators, A Phys.*, 2019.

[135] Y. Zhang *et al.*, "A 6-Degree-of-Freedom Piezoelectric Vibration Microstage with Reduced Cross-Axis Coupling," in *IEEE International Ultrasonics Symposium, IUS*, 2018.

[136] H. Zhang, Y. Wu, W. Wu, M. Wu, and X. Hu, "Improved multi-position calibration for inertial measurement units," *Meas. Sci. Technol.*, 2010.

[137] S. Nadig, V. Pinrod, S. Ardanuc, and A. Lal, "In-run scale factor and drift calibration of MEMS gyroscopes with rejection of acceleration sensitivities," in *IEEE 3rd International Symposium on Inertial Sensors and Systems, ISS 2016 - Proceedings*, 2016.

[138] W. I. Liu and Y. Li, “Error modeling and extrinsic–intrinsic calibration for LiDAR-IMU system based on cone-cylinder features,” *Rob. Auton. Syst.*, 2019.

[139] Y. Chen, “High-accuracy Motion Estimation for MEMS Devices with Capacitive Sensors,” University of Michigan, 2018.

[140] R. Hayes, E. Mumm, and K. Gotthelf, “Electrical Noise Performance of Gold-on-Gold Slip Rings,” *Proc. 43 rd Aerosp. Mech. Symp.*, 2016.

[141] S. Nadig, S. Ardanuc, and A. Lal, “Monolithic piezoelectric in-plane motion stage with low cross-axis-coupling,” in *Proceedings of the IEEE International Conference on Micro Electro Mechanical Systems (MEMS)*, 2014.

[142] D. J. Griffiths, *Introduction to Electrodynamics*. Upper Saddle River, NJ, USA: Prentice-Hall, Inc., 1999.

[143] K&J Magnetics Inc., “K&J Magnetics - Specifications.” [Online]. Available: https://www.kjmagnetics.com/specs.asp. [Accessed: 23-Sep-2019].

[144] Master Magnetics Inc., “Understanding Magnet Grades.” [Online]. Available: https://www.magnetsource.com/blog/understanding-magnet-grades/. [Accessed: 23-Sep-2019].

[145] Chengdu Heaven and Great Technology, “How to Understand the Grade of Sintered NdFeB Magnet? – China NdFeB Magnet, SmCo Magnet Supplier | HGT Co.,Ltd.” [Online]. Available: http://www.advancedmagnets.com/how-to-understand-the-rare-earth-permanent-magnets-grades-part-1-sintered-neodymium-iron-boron-magnets/. [Accessed: 23-Sep-2019].

[146] P. Campbell, *Permanent magnet materials and their application*. Cambridge : Cambridge University Press, 1994.

[147] D. J. Griffiths, *Instructure’s solutions manual Introduction to Electrodynamics*. 2004.

[148] X. Niu, Y. Li, H. Zhang, Q. Wang, and Y. Ban, “Fast Thermal Calibration of Low-Grade Inertial Sensors and Inertial Measurement Units,” *Sensors*, vol. 13, no. 9, pp. 12192–12217, Sep. 2013.

[149] J. B. Johnson, “Thermal Agitation of Electricity in Conductors,” *Phys. Rev.*, vol. 32, no. 1, pp. 97–109, Jul. 1928.

[150] H. Nyquist, “Thermal Agitation of Electric Charge in Conductors,” *Phys. Rev.*, vol. 32, no. 1, pp. 110–113, Jul. 1928.

[151] T. B. Gabrielson, “Mechanical-Thermal Noise in Micromachined Acoustic and Vibration Sensors,” *IEEE Trans. Electron Devices*, 1993.

[152] H. B. Callen and R. F. Greene, “On a theorem of irreversible thermodynamics,” *Phys. Rev.*, 1952.

[153] P. R. Saulson, “Thermal noise in mechanical experiments,” *Phys. Rev. D*, 1990.

[154] G. I. González and P. R. Saulson, “Brownian motion of a torsion pendulum with internal friction,” *Phys. Lett. A*, 1995.

[155] S. Al-Sarawi, M. Anbar, K. Alieyan, and M. Alzubaidi, “Internet of Things (IoT) communication protocols: Review,” in *ICIT 2017 - 8th International Conference on Information Technology, Proceedings*, 2017, pp. 685–690.

[156] S. K. Sharma and X. Wang, “Live Data Analytics with Collaborative Edge and Cloud Processing in Wireless IoT Networks,” *IEEE Access*, 2017.

[157] M. C. Domingo, “An overview of the internet of underwater things,” *Journal of Network and Computer Applications*. 2012.

[158] M. C. Vuran, A. Salam, R. Wong, and S. Irmak, “Internet of underground things in precision agriculture: Architecture and technology aspects,” *Ad Hoc Networks*, 2018.

[159] C.-C. Kao *et al.*, “A Comprehensive Study on the Internet of Underwater Things: Applications, Challenges, and Channel Models,” *Sensors*, vol. 17, no. 7, p. 1477, Jun. 2017.

[160] T. E. Abrudan, O. Kypris, N. Trigoni, and A. Markham, “Impact of Rocks and Minerals on Underground Magneto-Inductive Communication and Localization,”

IEEE Access, 2016.

[161] T. Olsson, "A MEchanical Based Antenna (AMEBA)," 2016. [Online]. Available: https://www.fbo.gov/index?s=opportunity&mode=form&id=a7ad32588088d94cf6d66af19851b22e&tab=core&_cview=0. [Accessed: 04-Mar-2019].

[162] J. J. Sojdehei, P. N. Wrathall, and D. F. Dinn, "Magneto-inductive (MI) communications," *Ocean. Conf. Rec.*, 2001.

[163] J. Wait, "Propagation of ELF electromagnetic waves and project sanguine/seafarer," *IEEE J. Ocean. Eng.*, vol. 2, no. 2, pp. 161–172, Apr. 1977.

[164] N. Strachen, J. Booske, and N. Behdad, "A mechanically based magneto-inductive transmitter with electrically modulated reluctance," *PLoS One*, vol. 13, no. 6, p. e0199934, Jun. 2018.

[165] J. A. Bickford, R. S. McNabb, P. A. Ward, D. K. Freeman, and M. S. Weinberg, "Low frequency mechanical antennas electrically short transmitters from mechanically-actuated dielectrics," in *2017 IEEE Antennas and Propagation Society International Symposium, Proceedings*, 2017.

[166] I. Grinberg, J. Kim, and G. Bahl, "Eigenmode Optimization and Topologically Protected States in MagnetoMechanical ULF Transmitter Arrays," in *Solid State Sensors Actuators and Microsystems Workshop*, 2018.

[167] M. B. Cohen, U. S. Inan, and E. W. Paschal, "Sensitive Broadband ELF/VLF Radio Reception With the AWESOME Instrument," *IEEE Trans. Geosci. Remote Sens.*, vol. 48, no. 1, pp. 3–17, Jan. 2010.

[168] A. Grosz, M. J. Haji-Sheikh, and S. C. Mukhopadhyay, *High Sensitivity Magnetometers*. Switzerland: Springer Nature, 2017.

[169] W. L. Stutzman and G. A. Thiele, *Antenna Theory and Design*. Hoboken, NJ, USA: John Wiley and Son, Inc., 2012.

[170] A. Madanayake *et al.*, "Energy-efficient ULF/VLF transmitters based on mechanically-rotating dipoles," in *2017 Moratuwa Engineering Research*

Conference (MERCon), 2017, pp. 230–235.

[171] M. Manteghi, "A navigation and positining system for unmanned underwater vehicles based on a mechanical antenna," in *2017 IEEE Antennas and Propagation Society International Symposium, Proceedings*, 2017.

[172] M. N. S. Prasad, Y. Huang, and Y. E. Wang, "Going beyond Chu harrington limit: ULF radiation with a spinning magnet array," in *2017 32nd General Assembly and Scientific Symposium of the International Union of Radio Science, URSI GASS 2017*, 2017.

[173] S. Selvin, M. N. Srinivas Prasad, Y. Huang, and E. Wang, "Spinning magnet antenna for VLF transmitting," in *2017 IEEE Antennas and Propagation Society International Symposium, Proceedings*, 2017.

[174] M. T. Bin Tarek *et al.*, "Power-Efficient Data Modulation for All-Mechanical ULF/VLF Transmitters," in *2018 IEEE 61st International Midwest Symposium on Circuits and Systems (MWSCAS)*, 2018, pp. 759–762.

[175] J. Xu *et al.*, "A low frequency mechanical transmitter based on magnetoelectric heterostructures operated at their resonance frequency," *Sensors (Switzerland)*, 2019.

[176] M. A. Kemp *et al.*, "A high Q piezoelectric resonator as a portable VLF transmitter," *Nat. Commun.*, vol. 10, no. 1, p. 1715, Dec. 2019.

[177] N. Ahmed, A. Radchenko, D. Pommerenke, and Y. R. Zheng, "Design and Evaluation of Low-Cost and Energy-Efficient Magneto-Inductive Sensor Nodes for Wireless Sensor Networks," *IEEE Syst. J.*, pp. 1–10, 2018.

[178] F. Tonolini and F. Adib, "Networking across boundaries: enabling wireless communication through the water-air interface," *Sigcomm*, 2018.

[179] X. Che, I. Wells, G. Dickers, P. Kear, and X. Gong, "Re-evaluation of RF electromagnetic communication in underwater sensor networks," *IEEE Commun. Mag.*, 2010.

[180] T. Fett, D. Munz, and G. Thun, "Tensile and bending strength of piezoelectric

ceramics," *J. Mater. Sci. Lett.*, no. 18, pp. 1899–1902, 1999.

[181] M. W. Hooker, "Properties of PZT-Based Piezoelectric Ceramics Between -150 and 250 C," 01-Sep-1998. [Online]. Available: https://ntrs.nasa.gov/search.jsp?R=19980236888. [Accessed: 01-Apr-2019].

[182] K&J Magnetics Inc., "Neodymium Magnet Physical Properties." [Online]. Available: https://www.kjmagnetics.com/specs.asp. [Accessed: 01-Apr-2019].

[183] Guosheng Yang, Jun Wang, Guangrong Yue, and Shaoqian Li, "Myriad MSK signal detection for VLF/LF communication," in *MILCOM 2016 - 2016 IEEE Military Communications Conference*, 2016, pp. 648–653.

[184] K. S. Shanmugam, *Digital and Analog Communication Systems*. Delhi, India: John Wiley and Son, Inc., 1985.

[185] S. C. Lin, I. F. Akyildiz, P. Wang, and Z. Sun, "Distributed Cross-Layer Protocol Design for Magnetic Induction Communication in Wireless Underground Sensor Networks," *IEEE Trans. Wirel. Commun.*, 2015.

[186] H. Oh, K. J. Lee, K. Lee, and S. S. Yang, "Gyroscopes based on surface acoustic waves," *Micro Nano Syst. Lett.*, 2015.

[187] H. Oh, W. Wang, S. Yang, and K. Lee, "Development of SAW based gyroscope with high shock and thermal stability," in *Sensors and Actuators, A: Physical*, 2011.

[188] B. Davaji, V. Pinrod, S. Kulkarni, and A. Lal, "Towards a surface and bulk excited SAW gyroscope," in *IEEE International Ultrasonics Symposium, IUS*, 2017.

[189] A. Mahmoud, M. Mahmoud, T. Mukherjee, and G. Piazza, "Investigating the impact of resonant cavity design on surface acoustic wave gyroscope," in *5th IEEE International Symposium on Inertial Sensors and Systems, INERTIAL 2018 - Proceedings*, 2018.

[190] A. Mahmoud, T. Mukherjee, and G. Piazza, "Novel Acoustic Gratings with High Reflection Constant for Surface Acoustic Wave Gyroscopes," in *IEEE*

International Ultrasonics Symposium, IUS, 2018.

[191] X. Wu, W. Chen, and A. Reza, "Optimal design of piezoelectric micromachined modal gyroscope (PMMG) with modes matched: modal analysis," *Microsyst. Technol.*, 2014.

[192] B. Davaji, A. Ruyack, and A. Lal, "Characterization of graphene electrodes as piezoresistive SAW transducers," in *IEEE International Ultrasonics Symposium, IUS*, 2017.

[193] B. Davaji, S. Kulkarni, V. Pinrod, A. Ruyack, and A. Lal, "Piezoresistive Graphene SAW Transducer," in *IEEE International Ultrasonics Symposium, IUS*, 2018.

[194] A. Mahmoud *et al.*, "Acousto-optic gyroscope," in *Proceedings of the IEEE International Conference on Micro Electro Mechanical Systems (MEMS)*, 2018.

[195] K. Hashimoto, *Surface Acoustic Wave Devices in Telecommunications*. 2013.

[196] R. Snieder, C. Sens-Schönfelder, E. Ruigrok, and K. Shiomi, "Seismic shear waves as Foucault pendulum," *Geophys. Res. Lett.*, 2016.

[197] J.-L. Auriault, "Body wave propagation in rotating elastic media," *Mech. Res. Commun.*, vol. 31, no. 1, pp. 21–27, Jan. 2004.

[198] M. Pijolat *et al.*, "Mode conversion in high overtone bulk acoustic wave resonators," in *2009 IEEE International Frequency Control Symposium Joint with the 22nd European Frequency and Time Forum*, 2009.

[199] M. Abdelmejeed, J. C. Kuo, and A. Lal, "AlN GHz ultrasonic pulse diffraction based transmit-receive oscillator with 1 PPM stability," in *TRANSDUCERS 2017 - 19th International Conference on Solid-State Sensors, Actuators and Microsystems*, 2017.

[200] Board IEEE Standards, *IEEE Standard Specification Format Guide and Test Procedure for Single –Axis Interferometric Fiber Optic Gyros*. 1997.

[201] V. Pinrod, B. Davaji, and A. Lal, “Coexisting Surface and Bulk Gyroscopic Effects,” in *IEEE International Ultrasonics Symposium, IUS*, 2018, pp. 1–4.

[202] V. Pinrod, B. Davaji, and A. Lal, “High-overtone bulk diffraction wave gyroscope,” in *IEEE MEMS 2019*, 2019.

[203] V. Pinrod, B. Davaji, and A. Lal, “Investigation of Scale Factor versus Frequency for a Bulk Wave Diffraction Gyroscope,” in *INERTIAL 2019 - 6th IEEE International Symposium on Inertial Sensors and Systems, Proceedings*, 2019.

[204] I. E. Dzyaloshinskii, “Sound waves in a rotating solid,” *Phys. Lett. A*, vol. 202, no. 5–6, pp. 403–404, Jul. 1995.

[205] J. N. Sharma and D. Grover, “Body wave propagation in rotating thermoelastic media,” *Mech. Res. Commun.*, 2009.

[206] J. N. Sharma, D. Grover, and D. Kaur, “Mathematical modelling and analysis of bulk waves in rotating generalized thermoelastic media with voids,” *Appl. Math. Model.*, 2011.

[207] M. Schoenberg and D. Censor, “Elastic Waves in Rotating Media,” *Q. Appl. Math.*, 1973.

[208] H. Fang, “Vibrations of a Rotating Piezoelectric Body and Applications in Gyroscopes,” University of Nebraska, 2000.

[209] H. Abe, T. Yoshida, and H. Watanabe, “Energy trapping of thickness-shear vibrations excited by parallel electric field and its application to piezoelectric vibratory gyroscopes,” *Proc. IEEE Ultrason. Symp.*, 1998.

[210] Z. Wang, M. Zhao, and J. Yang, “A piezoelectric gyroscope with self-equilibrated coriolis force based on overtone thickness-shear modes of a lithium niobate plate with an inversion layer,” *IEEE Sens. J.*, 2015.

[211] H. Chen, J. Wang, J. Du, and J. Yang, “Higher-order overtone thickness-shear vibrations of multilayered thin-film acoustic wave resonators and angular rate sensing,” *Int. J. Acoust. Vib.*, 2019.

[212] K. Nakamura and M. Ohsaki, “Trapped-energy vibratory gyroscopes using rotated Y-cut LiNbO3,” *Proc. Annu. IEEE Int. Freq. Control Symp.*, 1999.

[213] K. Nakamura and T. Abe, “Vibratory gyroscopes using trapped-energy vibrators of rotated Y-cut LiTaO3,” in *Proceedings of the IEEE Ultrasonics Symposium*, 2001.

[214] G. M. Reese, E. L. Marek, and D. W. Lobitz, “Three-dimensional finite element calculations of an experimental quartz rotation sensor,” in *Ultrasonics Symposium Proceedings*, 1989, vol. 1, pp. 419–422.

[215] J. S. Yang, “Analysis of ceramic thickness shear piezoelectric gyroscopes,” in *Proceedings of the IEEE Ultrasonics Symposium*, 1996, vol. 2, pp. 909–912.

[216] H. F. Tiersten, *Linear Piezoelectric Plate Vibrations: Elements of the Linear Theory of Piezoelectricity and the Vibrations Piezoelectric Plates*. New York, NY: Springer Science+Business Media, 1969.

[217] M. J. Benacquista and J. D. Romano, *Classical Mechanics*. Springer International Publishing AG, 2018.

[218] R. S. C. Cobbold, *Foundations of biomedical ultrasound*. New York : Oxford University Press, 2007.

[219] B. A. (Bertram A. Auld, *Acoustic Fields and Waves in Solids Volume I*. Malabar, Fla. : A Wiley-Interscience Publication, 1990.

[220] W. R. Smith, H. M. Gerard, T. M. Reeder, H. J. Shaw, and J. H. Collins, “Analysis of Interdigital Surface Wave Transducers by use of an Equivalent Circuit Model,” *IEEE Trans. Microw. Theory Tech.*, 1969.

[221] B. A. (Bertram A. Auld, *Acoustic Fields and Waves in Solids Volume II*. Malabar, Fla. : A Wiley-Interscience Publication, 1990.

[222] R. S. Weis and T. K. Gaylord, “Lithium niobate: Summary of physical properties and crystal structure,” *Appl. Phys. A Solids Surfaces*, 1985.

[223] J. Hoople, J. Kuo, S. Ardanuc, and A. Lal, “Chip-scale sonic communication using AlN transducers,” in *IEEE International Ultrasonics Symposium, IUS*, 2013, pp. 1934–1937.

[224] J. Hoople, J. Kuo, S. Ardanuç, and A. Lal, “Chip-scale reconfigurable phased-array sonic communication,” in *IEEE International Ultrasonics Symposium, IUS*, 2014, pp. 479–482.